

Department of Physics and Astronomy  
Heidelberg University

MASTER'S THESIS

in Physics

submitted by

**Patrick Michael Schygulla**

born in Villingen-Schwenningen

April 2018



# **Investigations of the Impact of Nuclear Quadrupole Moments on the Low-Frequency Elastic and Dielectric Susceptibilities of a Polymer Glass at Low Temperatures**

This Master's thesis has been carried out by Patrick Schygulla  
at the  
Kirchhoff-Institut für Physik  
under the supervision of  
**Professor Dr. Christian Enss.**



## Investigations of the Impact of Nuclear Quadrupole Moments on the Low-Frequency Elastic and Dielectric Susceptibilities of a Polymer Glass at Low Temperatures

Recent studies of glasses containing nuclear quadrupole moments have revealed deviations in the dielectric function from the predictions of the standard tunnelling model. Within this thesis the low-frequency elastic and dielectric properties of the polymer glass FR-122P were studied at temperatures ranging from 7 mK to 600 mK. A double paddle oscillator was used for elastic and a capacitance bridge for dielectric susceptibility measurements covering a frequency range between 60 Hz and 16 kHz. The large amount of nuclear quadrupole moments present in the investigated sample and the well known hyperfine level splitting enabled a thorough analysis of the role of nuclear quadrupole moments in this system. With the help of numerical calculations it could be shown that above around 200 mK the results agree with the standard tunnelling model while towards lowest temperatures interactions between nuclear quadrupole moments and atomic tunnelling systems need to be considered. Comparing the simulations with the measured data implies that the interactions result in an additional relaxation process rather than in changes of the tunnelling system distribution function. A novel experimental module was developed with the goal to directly study the influence of nuclear quadrupole moments. It allowed for selectively driving the nuclear quadrupole transition while simultaneously measuring the elastic susceptibility.

## Untersuchung des Einflusses von Kernquadrupolmomenten auf die niederfrequenten elastischen und dielektrischen Suszeptibilitäten eines Polymerglases bei tiefen Temperaturen

Messungen an Gläsern mit Kernquadrupolmomenten zeigten unlängst Abweichungen der dielektrischen Funktion von Vorhersagen des Standardtunnelmodells auf. In dieser Arbeit wurden niederfrequente elastische und dielektrische Eigenschaften des Polymerglases FR-122P bei Temperaturen zwischen 7 mK und 600 mK untersucht. Die elastische Suszeptibilität wurde mit einem Doppelflügeloszillator und die dielektrische Suszeptibilität mit einer Kapazitätsmessbrücke in einem Frequenzintervall von 60 Hz bis 16 kHz gemessen. Dank der großen Anzahl an Kernquadrupolmomenten in der untersuchten Probe und der bekannten Hyperfeinaufspaltung konnte die Rolle, die Kernquadrupolmomente in diesem System spielen, sorgfältig untersucht werden. Mithilfe numerischer Simulationen wurde gezeigt, dass oberhalb von etwa 200 mK die Messergebnisse mit dem Standardtunnelmodell übereinstimmen, wohingegen zu tieferen Temperaturen Wechselwirkungen zwischen Kernquadrupolmomenten und atomaren Tunnelsystemen berücksichtigt werden müssen. Ein Vergleich zwischen den Simulationen und Messdaten legt nahe, dass die Wechselwirkungen eine zusätzliche Relaxation statt einer Veränderung der Verteilungsfunktion der Tunnelsysteme zur Folge haben. Es wurde ein neuartiger experimenteller Aufbau entwickelt mit dem Ziel, den Einfluss der Kernquadrupolmomente direkt zu bestimmen. Mit diesem Aufbau kann der Kernquadrupolübergang selektiv angeregt werden, während gleichzeitig die elastische Suszeptibilität gemessen wird.



# Contents

List of Figures . . . . .	iii
List of Tables . . . . .	v
List of Abbreviations . . . . .	vi
List of Mathematical Symbols . . . . .	viii
<b>1 Introduction and Motivation</b>	<b>1</b>
<b>2 Theoretical Background</b>	<b>5</b>
2.1 Low-Temperature Dynamics in Glasses . . . . .	5
2.1.1 Glass Formation and Thermal Properties . . . . .	5
2.1.2 Structure of Amorphous Materials . . . . .	7
2.1.3 Energy States in a Double Well Potential . . . . .	9
2.1.4 The Standard Tunnelling Model . . . . .	11
2.1.5 Frequency Response of Amorphous Samples . . . . .	13
2.2 Nuclear Quadrupole Moments . . . . .	23
2.2.1 Nuclear Quadrupole Resonance . . . . .	23
2.2.2 Resonant Susceptibility . . . . .	26
2.2.3 Relaxation Mechanisms . . . . .	28
<b>3 Experimental Methods</b>	<b>33</b>
3.1 Working at Low Temperatures . . . . .	33
3.1.1 Cooling Methods . . . . .	33
3.1.2 Thermometry . . . . .	35
3.2 Polymer Glass FR-122P . . . . .	36
3.2.1 Chemical Structure . . . . .	36
3.2.2 Sample Production . . . . .	36
3.2.3 Material Choice . . . . .	37
3.3 Acoustic Measurements . . . . .	38
3.3.1 Double Paddle Oscillator . . . . .	38
3.3.2 Measurement Strategy . . . . .	43
3.3.3 Probing the Nuclear Bath . . . . .	49
3.4 Dielectric Measurements . . . . .	52

<b>4</b>	<b>Results and Analysis</b>	<b>55</b>
4.1	Preparatory Measurements . . . . .	55
4.1.1	High Temperatures . . . . .	55
4.1.2	Background . . . . .	57
4.1.3	Voltage Scaling . . . . .	58
4.1.4	Thermalisation . . . . .	60
4.2	Complex Acoustic and Dielectric Susceptibilities . . . . .	62
4.2.1	Temperature Overview . . . . .	62
4.2.2	Acoustic Measurements . . . . .	62
4.2.3	Dielectric Measurements . . . . .	64
4.3	Numerical Calculations . . . . .	66
4.3.1	Standard Tunnelling Model . . . . .	67
4.3.2	Resonant Susceptibility . . . . .	68
4.3.3	Additional Relaxation Rate . . . . .	69
4.4	Impact of RF Bias . . . . .	70
<b>5</b>	<b>Discussion</b>	<b>75</b>
5.1	Validity of Data . . . . .	75
5.2	Conclusion . . . . .	77
5.2.1	Interpretation of Results . . . . .	77
5.2.2	Comparison to Related Work . . . . .	79
5.3	Outlook . . . . .	81
<b>6</b>	<b>Summary</b>	<b>83</b>
	<b>References</b>	<b>85</b>
	<b>Appendices</b>	<b>92</b>
A	Mathematical Derivations . . . . .	92
B	Complementary Figures . . . . .	93
	<b>Danksagung</b>	<b>99</b>

## List of Figures

1.1	Anomalous frequency dependence of NQM containing samples. . . . .	2
2.1	Specific heat and thermal conductivity of vitreous and crystalline silica. . . . .	6
2.2	Pair correlation functions of liquid, amorphous and solid material. . . . .	7
2.3	Scanning tunnelling microscope picture of amorphous silica bilayer. . . . .	8
2.4	Schematic structure of amorphous silica with TLS. . . . .	8
2.5	Generic double well potential. . . . .	9
2.6	Energy eigenstates of a TLS. . . . .	10
2.7	Distribution function of TLS. . . . .	12
2.8	Bloch sphere representation of a TLS. . . . .	14
2.9	Absorption and stimulated emission of a phonon. . . . .	15
2.10	Frequency dependence of the resonant contribution to the elastic constant. . . . .	16
2.11	Changes of the TLS energy splitting due to an external field. . . . .	17
2.12	Frequency course of a Debye relaxator. . . . .	18
2.13	Synopsis of the temperature dependence of different relaxation rates. . . . .	20
2.14	Speed of sound and internal friction according to the STM. . . . .	21
2.15	Frequency dependence of the elastic susceptibility according to the STM. . . . .	22
2.16	Model of an oblate nucleus in an inhomogeneous electric field. . . . .	24
2.17	Energy level diagram of a NQM carrying a TLS in a magnetic field. . . . .	25
2.18	Misalignment of the NQM quantisation axis with the EFG due to tunnelling. . . . .	26
2.19	Pseudogap in the TLS distribution function. . . . .	28
2.20	Changes of the speed of sound assuming resonant NQM-TLS interaction. . . . .	28
2.21	Nuclear quadrupole driven relaxation rate. . . . .	30
2.22	Speed of sound and internal friction assuming NQM driven relaxation. . . . .	31
2.23	Role of the quadrupole splitting in the NQM driven relaxation model. . . . .	32
2.24	Frequency dependence of the NQM driven relaxation model. . . . .	32
3.1	Schematic set-up of the nitrogen bath cryostat. . . . .	34
3.2	Schematic set-up of the $^3\text{He}/^4\text{He}$ dilution cryostat. . . . .	35
3.3	Chemical structure of FR-122P. . . . .	37
3.4	Eigenmodes of a vibrating reed compared to a DPO. . . . .	39

3.5	Proportions of the fabricated DPO. . . . .	40
3.6	Edge quality of the DPO after milling. . . . .	40
3.7	DPO eigenmodes. . . . .	43
3.8	Experimental set-up used for acoustic measurements. . . . .	44
3.9	Amplitude and phase course of a DPO resonance. . . . .	48
3.10	Sketch of novel nuclear quadrupole transition drive module. . . . .	50
3.11	Simulated power dissipation in DPO under RF bias. . . . .	51
3.12	Transmission spectrum of the bias loop. . . . .	51
3.13	Circuit diagram and set-up for dielectric measurements. . . . .	53
4.1	High-temperature speed of sound and internal friction. . . . .	56
4.2	Impact of the 1 K pot on the noise level. . . . .	57
4.3	Noise spectrum of the acoustic experimental set-up. . . . .	58
4.4	Excitation voltage dependence of resonance frequency and internal friction. . . . .	59
4.5	Excitation voltage dependence of the acoustic signal amplitude. . . . .	60
4.6	Bias voltage dependence of the acoustic signal amplitude. . . . .	61
4.7	Thermalisation measurements. . . . .	61
4.8	Change in speed of sound and internal friction from 10 mK to 300 K. . . . .	62
4.9	Low-temperature change in speed of sound and internal friction. . . . .	64
4.10	Onset of relaxation part in internal friction. . . . .	65
4.11	Low-temperature changes of the speed of light and loss tangent. . . . .	66
4.12	Comparison between STM predictions and experimental data. . . . .	67
4.13	Comparison between resonant susceptibility model and data. . . . .	68
4.14	Comparison between NQM driven relaxation model and data. . . . .	69
4.15	Frequency sweep of the RF bias field at constant input power. . . . .	70
4.16	Power sweep of the RF bias field at constant frequency. . . . .	72
4.17	Complex plane representation of DPO response to bias field. . . . .	73
5.1	Synopsis of the acoustic and dielectric measurements. . . . .	78
5.2	Changes of the speed of light at kHz and MHz probing frequencies. . . . .	80
5.3	Real part of the dielectric permittivity of Br-DGEBA and HY-1. . . . .	81
B.1	Longitudinal NQR relaxation times of vitreous and crystalline $\text{As}_2\text{S}_3$ . . . . .	93
B.2	Shape of pseudogap for varying model parameters. . . . .	93
B.3	Speed of sound for varying pseudogap model parameters. . . . .	94
B.4	Susceptibility for varying NQM relaxation cut-off. . . . .	94

B.5	Susceptibility for varying NQM relaxation prefactor. . . . .	95
B.6	Picture of fabricated DPO. . . . .	95
B.7	Relative signal strengths of different eigenmodes. . . . .	96
B.8	Peak shape synopsis for different excitation voltages. . . . .	96
B.9	Background noise histogram. . . . .	96
B.10	Bias voltage dependence of resonance frequency and internal friction. . . . .	97
B.11	STM fit of speed of sound and internal friction for each frequency. . . . .	97
B.12	Pseudogap model fit with varying spin misalignment. . . . .	98
B.13	Qualitative comparison of internal friction with NQM driven relaxation model. . . . .	98

## List of Tables

2.1	Temperature dependencies of speed of sound and internal friction. . . . .	22
3.1	Boiling temperatures of cryogenic substances. . . . .	33
3.2	Simulated and measured resonance frequencies of DPO. . . . .	44

## List of Abbreviations

**AC** alternating current, generally an alternating field of finite frequency

**ADC** analogue-to-digital converter

**AlBaSi** multicomponent glass consisting of BaO-Al<sub>2</sub>O<sub>3</sub>-SiO<sub>2</sub>, contains NQM

**BK-7** multicomponent borosilicate glass, no large NQM

**BrDGEBa** brominated bisphenol A diglycidyl ether, molecular glass, contains NQM

**DAQ** data acquisition system

**DPO** double paddle oscillator

**EFG** electric field gradient

**FR** flame retardant

**FR-122P** trade name of a polymeric material with 11 atomic percent of bromine, contains NQM

**FWHM** full width at half maximum

**GPIB** general purpose interface bus

**Herasil** trade name of a quartz glass, negligible amount of NQM

**HF** high frequency

**HY-1** trade name of multicomponent glass with 0.5 atomic percent of holmium, contains NQM

**LPF** low-pass filter

**NKZFS-11** trade name of multicomponent glass with 1.5 atomic percent of tantalum, contains NQM

**NAR** nuclear acoustic resonance

**NCL** nearly constant loss

**NMR** nuclear magnetic resonance

**NQM** nuclear (electric) quadrupole moment

**OFHC** oxygen-free high-conductivity material

**PVAc** poly(vinyl acetate), many highly polar bonds, negligible amount of NQM

**RF** radio frequency

**SMA** subminiature version A coaxial cable  
**SNR** signal-to-noise ratio  
**SQUID** superconducting quantum interference device  
**STM** Standard Tunnelling Model  
**TLS** two-level system  
**TMP** turbomolecular pump  
**UHV** ultra high vacuum  
**US** ultrasound  
**WKB** Wentzel-Kramers-Brillouin approximation

## List of Mathematical Symbols

---

$a$	lattice constant (in crystals) or average distance between atoms (in glasses)	
$c_V$	specific heat at constant volume	$c_V = \partial U / \partial T _V$
$c$	speed of light in a material	$c = c_0 / \sqrt{\epsilon_0 \epsilon}$
$C$	macroscopic coupling constant of STM	$C = p_0 \gamma^2 / (\rho v^2)$
$\mathcal{C}$	dynamical elastic constant	
$d_{\text{conf}}$	generic configuration space coordinate	
$d$	distance between double wells in real space	
$\Delta$	asymmetry energy of a double well	
$\Delta_0$	tunnelling splitting	$\hbar \Omega e^{-\lambda}$
$\eta_a$	asymmetry parameter of electric field gradient	$\eta_a = (V_{xx} - V_{yy}) / V_{zz}$
$\eta$	nuclear spin overlap integral in a TLS	$\eta = \langle \Psi_{s,l}   \Psi_{s,r} \rangle$
$e(t)$	strain field	
$e$	elementary charge	$e = 1.6 \times 10^{-19} \text{ C}$
$\epsilon$	complex dielectric susceptibility	$\epsilon = \epsilon' + i\epsilon''$
$E$	energy splitting of states in a tunnelling system	$E = \sqrt{\Delta^2 + \Delta_0^2}$
$f_0$	resonance frequency of an oscillator	
$\mathbf{F}$	electrical field	
$\gamma$	coupling strength between phonons and TLS	
$\gamma_n$	gyromagnetic ratio of a nucleus	
$\hbar$	reduced Planck constant	$\hbar = h / (2\pi) = 1.05 \times 10^{-34} \text{ J s}$
$\mathcal{H}$	Hamiltonian operator (in basis of eigenstates)	$\mathcal{H}\Psi = E\Psi$
$k_B$	Boltzmann constant	$k_B = 1.38 \times 10^{-23} \text{ J K}^{-1}$
$\kappa$	thermal conductivity	$\kappa = 1/3 v c_V \ell$
$\ell$	(phonon) mean free path	$\ell = 1/(\sigma n)$
$\lambda$	tunnelling parameter of a TLS	
$m$	mass of tunnelling particle	
$\mu_n$	magnetic moment of an atomic nucleus	$\mu = \gamma_n I$
$\nu_q$	nuclear quadrupole resonance frequency	$\nu_q \propto \mathcal{Q}$
$N_{\pm}$	TLS occupation of the upper/lower state	$N = N_+ + N_-$
$p$	distribution of two-level systems	$p \, d\lambda d\Delta \stackrel{\text{STM}}{=} p_0 \, d\lambda d\Delta$
$\mathbf{p}$	dipole moment of a TLS	$\mathbf{p} = \langle \Psi   \rho(\mathbf{r}) \mathbf{r}   \Psi \rangle$
$\Psi$	quantum mechanical wave function	
$Q^{-1}$	internal friction, inverse quality factor	$Q^{-1} = \rho v^2 \Im(\delta C)$
$\mathcal{Q}$	nuclear electric quadrupole moment	$\mathcal{Q} = \langle \Psi   \rho(\mathbf{r}) (3 \cos(\theta_i) - 1) \mathbf{r}_{\perp}^2   \Psi \rangle$
$\rho$	charge or mass density	
$\sigma_i$	$i$ th component of Pauli matrix vector	
$\tau_{1/2}$	longitudinal/transverse TLS relaxation time	
$T$	temperature	
$U$	internal energy	
$\delta v/v$	relative change in the speed of sound	$\delta v/v = \Re(\delta C) / (2\rho v^2)$
$V_b$	potential barrier height of a double well	
$\Omega$	resonance frequency of a harmonic potential	
$Z$	partition function in canonical ensemble	$Z = \sum_i \exp(-E_i / (k_B T))$

---

# 1. Introduction and Motivation

Glasses have since long attracted special interest among humans thanks to some of their interesting and useful properties, for instance their transparency which enabled their usage as window panes along with traces of metallic admixtures providing colour. This fact is also what gave glass its name which is derived from the Germanic word *glasa* meaning „shimmering“ or „shining“. The existence of glass precedes human history, though, for early glass samples on Earth originate from volcanic eruptions. Upon sufficiently fast cooling below the glass transition temperature hot lava forms an amorphous solid, or in other words a glass, called obsidian. Another possibility for natural glass production are volcanic lightnings caused by friction between ash particles which melt in the course of a flash. Under certain cooling conditions they can form glass spheres that allow scientists to study eruption parameters at a safe distance [Ber17].

While the variety of glasses is as wide as their application spectrum, ranging from storing liquids over glass fibres to optical devices, the common and defining trait is their amorphous structure in contrast to crystals. The latter are characterised by a well defined crystal lattice that determines order and symmetry of the crystal by setting the position of every atom of the solid once a single atomic position is fixed. The former do not exhibit such a long range order. Rather, in glasses both the distances and bonding angles between neighbouring atoms are not discrete but show a broad distribution resulting in structural disorder.

Measurements of the specific heat and thermal conductivity [Las75, Zel71, Cah88] revealed a remarkably similar behaviour of different glasses at low enough temperatures, which deviated from what was measured in crystals. This coined the notion of the *universality of glasses*, a term which already suggests that at low temperatures the physics of glasses is exclusively governed by dynamic entities that are common to all amorphous structures but absent in crystals. We shall see as we go along that these entities can well be pictured as groups of atoms moving in and tunnelling through an irregular potential energy landscape. This phenomenologically motivated *Standard Tunnelling Model* (STM), was first put forward by Anderson, Halperin, Varma [And72] and independently by Phillips [Phi72] in 1972. It was to have a successful carrier in describing not only the low-temperature thermal properties but also the acoustic and dielectric susceptibilities of a large variety of glasses quite accurately given the simplistic set of underlying assumptions. Over the years, though, deviations of different kinds between experiments and predictions from the STM became apparent which triggered the development of extensions to the STM that take into account the structural and chemical properties of different amorphous materials and as a consequence started softening the universality claim. Examples include but are not limited to experiments that point to changing and restricting the distribution function of the tunnelling systems [Dou80], introducing interactions among them [Arn75] or taking the presence of nuclear electric quadrupole moments (NQM) into account [Wür02, Bur06a, Luc14].

In the framework of the STM dielectric glasses are indifferent to the application of small magnetic fields. However, it was found both from measurements of the dielectric function [Str00] and polarisation echo experiments [Lud02] that already minor static magnetic fields had a substantial effect on the multicomponent glass AlBaSi. Interesting enough, measurements of the elastic susceptibility of the borosilicate glass BK-7 did not show any sign of a magnetic field dependence [Lay01] raising the question whether this effect was due to a combi-

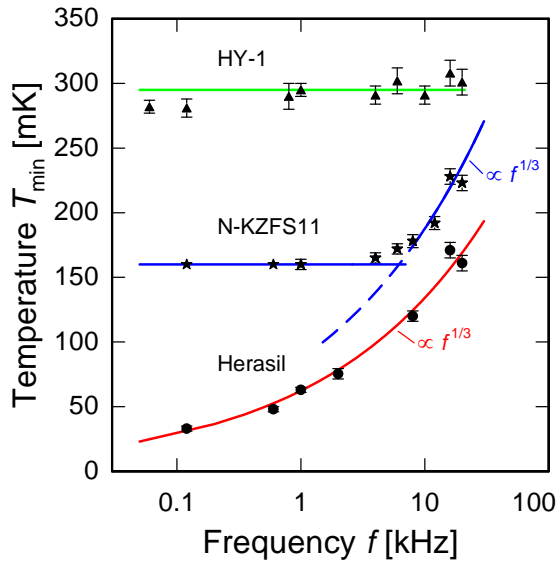


**Figure 1.1:** The temperature  $T_{\min}$  of the minimum in the real part of the dielectric function is shown as a function of probing frequency  $f$  for both NQM containing samples (HY-1, NKZFS-11) and a NQM-free sample (Herasil) [Luc14].

nation of magnetic and electric fields. With polarisation echo experiments on glycerol, which had been deuterated so that it contained NQM, Bartkowiak et al. succeeded to attribute the magnetic field sensitivity to the participation of NQM carrying atoms in the tunnelling motion and thus to learn something about the microscopic nature of some of the tunnelling systems [Bar13]. Suggested models for the effect on susceptibilities either see the cause of the deviations from the STM in a resonant interaction between the NQM and the tunnelling system [Bur06b] or in an additional relaxation pathway for the tunnelling systems [Luc16]. Recent studies demonstrated that the position of the minimum in the real part of the dielectric function in NQM containing samples does not follow the  $f^{1/3}$ -law predicted by the STM but becomes frequency independent at sufficiently low probing frequencies as shown in Fig. 1.1. This observation was made in acoustic measurements as well [Hem14] demonstrating that this kind of experiments is equally suited to look for peculiarities potentially caused by NQM. The findings were reproduced in numerical simulations assuming nuclear spin dominated relaxation in the kHz range.

A second chain of scientific research which motivates the subject of this thesis are nuclear quadrupole resonance experiments carried out on a number of vitreous and crystalline samples [Rub75, Kan80]. The measurement results of glasses exhibited anomalies in the spin-lattice relaxation time  $T_1$ , i.e. the time it takes for a nucleus in an energetically higher lying quadrupole state to release its energy and make a transition to the ground state. Compared to crystals the relaxation rates in glasses are about two orders of magnitude larger [Rub74] as shown in Fig. B.1. The existence of “low-frequency disordered modes” as the tunnelling systems were called [Sie93] and the standard tunnelling model provided the tools to explain the findings. The argument was that in glasses the occurrence of tunnelling systems and their influence on the local electrical environment in the vicinity of quadrupole moments provides a very efficient relaxation path.

This is the context in which this thesis is set. By mechanically probing a NQM containing sample at low frequencies it tries to deepen the understanding of the role that nuclear quadrupole moments play in amorphous materials. In particular the question is tackled whether their impact is predominantly based on an additional relaxation mechanism between NQM and tunnelling systems or whether it follows from a (pseudo)gap in the distribution function. To this end a specific material, FR-122P, was chosen. This polymer glass combines

---

two advantages: On the one hand it contains bromine atoms which carry a large nuclear quadrupole moment. On the other hand these bromine atoms are all covalently bond to carbon atoms and thus experience very similar chemical and thus electrical environments. Hence, the quadrupole level splitting is well defined, discrete and known. What is even more is that the Zeeman splitting of the hyperfine levels is negligibly small for ambient magnetic fields compared to the (pure) quadrupole splitting energy. This fact distinguishes the material at hand from previously studied samples with NQM, such as multicomponent glasses, which have a complicated chemical structure and additional strong magnetic dipole moments, and makes it a suitable candidate for the investigation of potential NQM effects.

This thesis is structured as follows: in Chapter 2 the STM is first introduced, explained and its most important results for the present study are derived in due briefness. With this firm ground set the definition of nuclear electric quadrupole moments is given, the physics of nuclear quadrupole resonance phenomena is discussed and theoretical considerations are made about interactions of nuclear quadrupole moments with other microscopic degrees of freedom such as tunnelling systems and with external fields. Once the theoretical foundation is laid the experimental strategy that was pursued is presented in Chapter 3. The analysed sample, a dielectric polymer glass, is characterised both chemically and physically and its suitability for the purpose at hand is justified in detail. The core experiments were carried out at temperatures ranging from 10 mK to 600 mK so the experimental challenges of obtaining and working within such a low-temperature environment are briefly described. The major part of the experimental work comprised low-frequency acoustic measurements, i.e. measurements of the relative change of the speed of sound and the internal friction at frequencies below 10 kHz. These were carried out using a double paddle oscillator (DPO) manufactured from the material of interest. Its production process, eigenmodes and integration into the experimental set-up is elucidated. In the course of this work a novel experimental module was designed and fabricated allowing to probe the sample with an additional radio frequency (RF) input line with the goal to selectively deposit energy into the nuclear bath and look for changes in the sample's susceptibility. This module is characterised electromagnetically and both its features and potential disadvantages are discussed. In addition to acoustic properties the dielectric susceptibility of FR-122P was measured as well at low temperatures for the sake of consistency. In the subsequent Chapter 4 the results from thermalisation, power dependence, and from the complex acoustic and dielectric susceptibility measurements are presented before these are compared to expectations from theory, provided by numerical calculations of the STM equipped with several extensions. Finally, the observations from the RF bias experiments are shown and analysed. Broadening the horizon in Chapter 5, the results are tried to be framed in a bigger picture. Findings from related experiments at low and intermediate frequencies of the same and similar materials are discussed and a conclusion is drawn. The summary in Chapter 6 concludes the thesis.



## 2. Theoretical Background

Since the time that the first measurements of solid state properties such as the specific heat and thermal conductivity revealed differences between crystalline and amorphous samples the discussion was ignited about whether there was a fundamental cause explaining all of the observed phenomena and if yes what it was. The suggestions ranged from impurities and defects over low lying electronic states and motional states of ions to one-dimensional vibrations and trapped atoms or groups of atoms [Zel71]. The latter idea turned out fruitful and prepared the ground for the development of the Standard Tunnelling Model which, despite of building upon rather simple phenomenological assumptions, describes and predicts quite accurately the low-temperature behaviour of a broad variety of glasses. In Section 2.1 at first the formation and resulting structure of glasses is discussed before the Standard Tunnelling Model is described in detail starting from a microscopic picture of tunnelling systems. Next, the most important consequences of this model for susceptibility measurements are derived. The second, important theoretical building block, to be reconciled with the tunnelling model, is the theory of quadrupole moments, resonance effects and relaxation phenomena, all of which are subject of Section 2.2.

### 2.1 Low-Temperature Dynamics in Glasses

#### 2.1.1 Glass Formation and Thermal Properties

When a liquid is cooled down slowly enough the atoms have a sufficient amount of time to find and occupy the energetically most favourable positions within the potential energy landscape that is created by all surrounding atoms starting from an arbitrary initial configuration. However, in the case of glasses the atoms are not able to occupy the configuration that minimises the energy. Upon cooling the viscosity of the glass melt increases more and more. The temperature at which the viscosity equals the conventional threshold  $10^{12}$  Pa.s is called the glass transition temperature  $T_g$  of this specific substance at a certain cooling rate. In contrast to crystals, which exhibit a sharp peak in the specific heat and thermal conductivity, in glasses these quantities do not show but a smooth step when cooled or heated through  $T_g$ . This also leaves its mark in the temperature dependence of the sample's volume. In a crystalline system there is a discontinuous drop in volume from the liquid to the crystalline phase at the melting temperature  $T_m$  while the glass first exhibits a phase of supercooled melt until the volume reaches its value of the condensed phase at  $T_g$ . The fact that the volume of the glass below  $T_g$  is larger than for the crystalline counterpart reflects the argument above, namely that the ground state is not reached. The glass transition is thus not an ordinary phase transition; its nature is yet not fully understood. Hence, a glass is not in thermal equilibrium and remains even to lowest temperatures in a state of finite entropy. Work by Strehlow et al. on the multicomponent glass AlBaSi [Str98] indicated, though, that there is an additional phase transition associated with the ordering of atomic degrees of freedom, the so called tunnelling systems that will be introduced in Section 2.1.3; if the interactions between them are strong enough these systems might form a macroscopic wave function and thus enable the sample to reduce its entropy, similar to the ordering of electrons in momentum space as Cooper pairs.

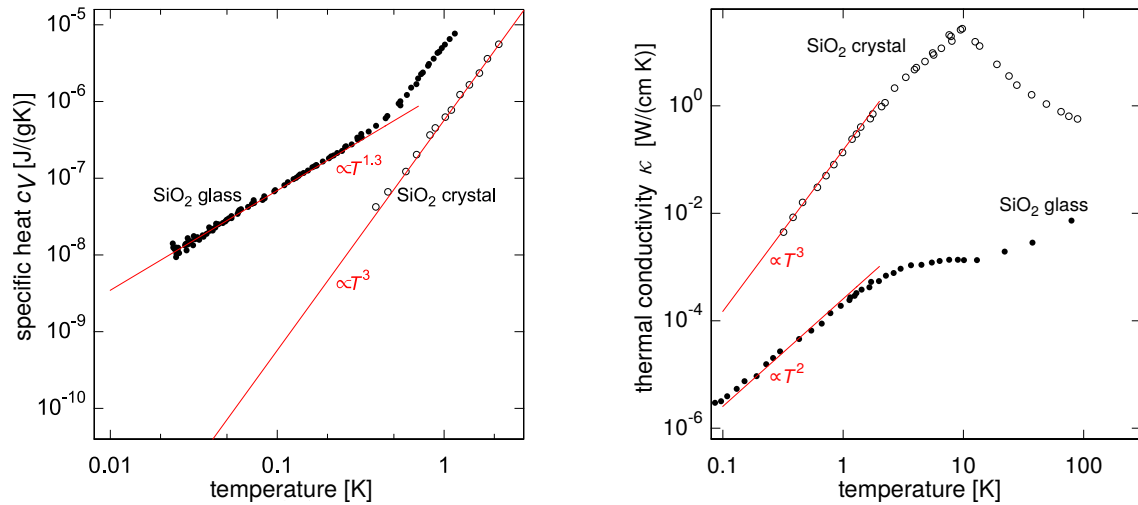


**Figure 2.1:** Comparison of the temperature dependence of the specific heat (left) and of the thermal conductivity (right) of vitreous and crystalline silica (specific heat data from [Las75, Zel71] and thermal conductivity data from [Cah88]).

Going to low temperatures additional differences between glasses and crystals can be observed in two important solid state quantities. The specific heat or heat capacity  $c_V = \partial E / \partial T$  is defined as the amount of energy  $dE$  needed to increase the temperature of the sample by  $dT$ . It is therefore a measure of the internal microscopic degrees of freedom since in the more ways microscopic entities such as spins, vibrations, electrons etc. can be excited the more energy is needed for a given temperature rise. One can thus learn something about the distribution function of the contributing excitations by measuring the specific heat's temperature dependence. If it is dominated by lattice vibrations, that is phonons, it is expected to follow the prediction of the Debye model: a  $T^3$ -dependence at low temperatures and a constant term recovering the classical Dulong-Petit law at high temperatures. However, in 1971 Zeller and Pohl found that in vitreous silica there is an anomalous, almost linear contribution, cf. left hand side of Fig. 2.1, that could not be attributed to any phenomenon that was known at that time [Zel71]. Another remarkable observation was the fact that unlike for crystals the thermal conductivity  $\kappa$  of glasses, a measure for how fast a temperature gradient is equilibrated, does not follow the predicted  $T^3$ -dependence derived from the Debye model, either. It rather exhibits a quadratic dependence as shown on the right hand side of Fig. 2.1. With the thermal conductivity being a transport quantity it reveals more about the nature of the involved excitations, namely about their mobility and interactions. When more and more amorphous samples were investigated besides quartz glasses yet another interesting experimental fact was established: the specific heat and thermal conductivity of different kinds of glasses as different as vitreous silica ( $\text{SiO}_2$ ), arsenic trisulfide ( $\text{As}_2\text{S}_3$ ) or polymethyl methacrylate ( $\text{C}_5\text{O}_2\text{H}_8$ , PMMA) all lie within one order of magnitude and have the same temperature dependence [Las75, Zel71]. The specific heat of these different glasses is consistently larger than in the case of the corresponding crystal while the thermal conductivity is consistently smaller.

### 2.1.2 Structure of Amorphous Materials

Diffraction experiments with x-rays or neutrons are able to offer hints on how the atoms that make up a certain sample are arranged. If applied to crystalline samples this method yields sharp and well defined diffraction patterns from which the crystal lattice, the bonding lengths and angles in different directions along the crystal axes and the pair correlation function

$$g(\mathbf{r}_1, |\Delta\mathbf{r}|) = \frac{1}{n_0^2} \overline{n(\mathbf{r}_1)n(\mathbf{r}_1 + \Delta\mathbf{r})}, \quad n_0 = \overline{n(\mathbf{r})}, \quad (2.1)$$

where  $n(\mathbf{x})$  is the particle density, can be determined. The pair correlation function measures the probability to find another atom at position  $\mathbf{r}_1 + \Delta\mathbf{r}$  if there is already an atom at position  $\mathbf{r}_1$ .

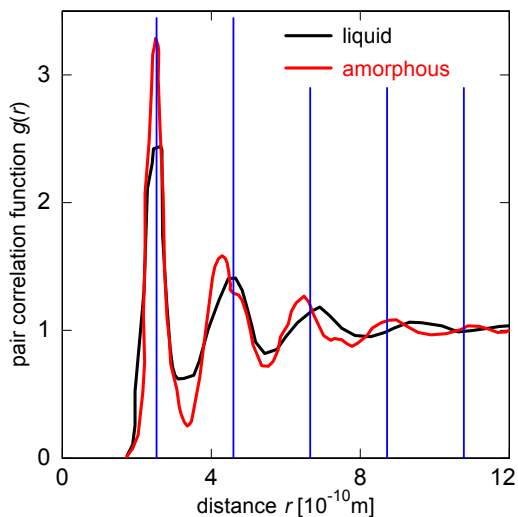


**Figure 2.2:** The pair correlation function  $g(r)$  of amorphous nickel resembles the one of liquid nickel (data from [Was80]). In blue the pair correlation function of a perfect crystal is sketched schematically.

Comparing the pair correlation functions of crystals, which exhibit sharp peaks at multiples of the lattice constant, to the ones of glasses and liquids, shown in Fig. 2.2, one notices that the amorphous case is much more similar to the liquid case which leads to the conclusion that a glass can be thought of as a supercooled liquid for which only a mean distance between atoms can be defined. Long-range order is replaced by short-range order over only a few atomic spacings and the atoms find themselves embedded in a random network with a broad distribution of bonding lengths and angles. This interpretation dates back to the work by Zachariassen in the 1930ies in which he also argued that the forces between neighbouring atoms were the same for both crystals and glasses, that the atoms oscillated about given equilibrium positions and that the only difference was the lack of symmetry, periodicity, and order in the latter [Zac32].

Recent studies on amorphous silicate bilayers which were grown on a single crystal ruthenium substrate using scanning tunnelling microscope and x-ray diffraction also seem to confirm that the Zachariassen picture is the correct one [Max14]. The real atomic structure of at least two-dimensional amorphous samples as shown in Fig. 2.3 thus justifies continuing to use this model.

An amorphous structure of the Zachariassen kind results in a similarly irregular potential energy landscape since the overall potential is the sum of all contributions from different

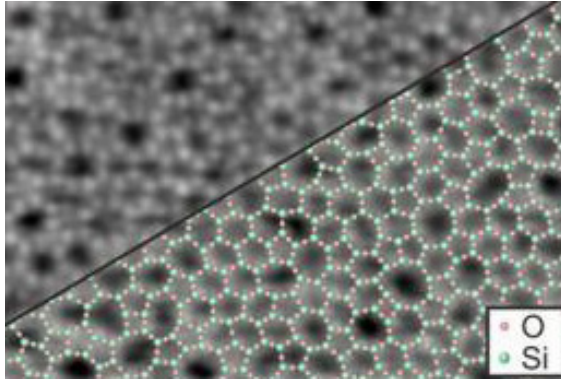


**Figure 2.3:** Scanning tunnelling microscope picture of an amorphous two-dimensional  $\text{SiO}_2$  bilayer [Max14]. The raw image is shown in the upper left half of the image. In the lower right half the centres-of-mass of the oxygen and silicon atoms are overlaid as calculated from an image analysis algorithm.

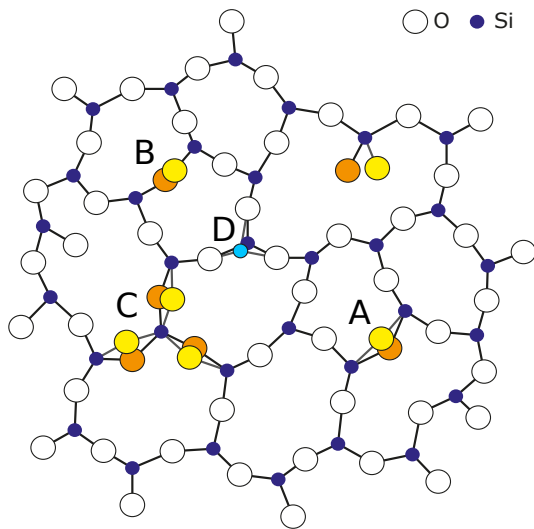


**Figure 2.4:** Schematically depicted amorphous structure of vitreous silica with different equilibrium positions marked in yellow and orange (adapted from [Ens05, p.317]). The oxygen atom at position A can occupy two transversely displaced, the atom at position B two longitudinally displaced positions (relative to the bond) while the group C can rotate as a whole by some angle. For the silicon atoms, for example atom D, changing their positions is more difficult due to their four tetrahedrally arranged bonds and their larger mass.

bonding types (ionic, van-der-Waals, covalent, ...), depending on the constituting atoms, their positions and interactions. Therefore, handy solid state concepts such as Brillouin zones and the Bloch theorem are not applicable. Even the phonon, a collective excitation of the entire sample, can no longer be defined as an eigenstate of the lattice Hamiltonian. However, for low enough phonon energies  $E_{\text{ph}}$ , i.e. sufficiently low temperatures  $T$ , one can write with the dominant phonon approximation

$$k_{\text{B}}T \approx E_{\text{ph}} = \hbar\omega \approx \hbar kv. \quad (2.2)$$

Here,  $v$  is the speed of sound of the material. In this case the wave vector  $k = 2\pi/\lambda$  is small or correspondingly the wavelength  $\lambda$  large and the dispersion curve is in the linear regime. Then, the second approximation in Eq. (2.2) becomes valid and the phonon wavelength stretches over many average atomic distances  $a \ll \lambda$ . The phonons should then be insensitive to the exact microscopic structure of the sample and a phonon dispersion can be measured. This could lead one to the deduction that the low-temperature properties of glasses and crystals should be identical if the phonons were the only relevant excitation in the solid. Yet, another type of local modes occurs in glasses thanks to their irregular distribution of potential energy. As depicted in Fig. 2.4 the irregular atomic network offers to some atoms or groups of atoms several local potential minima configurations separated by an energy barrier. Those atoms can tunnel quantum mechanically through this barrier and occupy both configurations with some finite probability. In polymer glasses, like the one that is studied in this thesis, besides

single atom TLS one can also think of entire side groups of the polymeric backbone, such as benzene, to perform displacements or rotations [McI06].

### 2.1.3 Energy States in a Double Well Potential

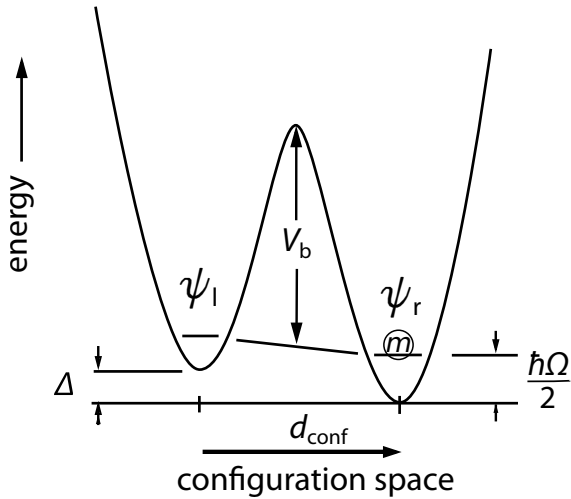


**Figure 2.5:** A generic double well potential with the two lowest lying states  $\Psi_l$  and  $\Psi_r$ . The two wells, lying a configurational distance  $d_{\text{conf}}$  apart, are separated by an energy barrier  $V_b$  and differ in the minimum energy by the asymmetry energy  $\Delta$ . The states have a harmonic oscillator ground state energy of  $\hbar\Omega/2$  above the well minimum. Here, a particle of mass  $m$  is localised inside the right well (adapted from [Phi81]).

Cutting through such an energy landscape along some configuration dimension  $d_{\text{conf}}$  which could either be real space,  $\mathbf{d}_{\text{conf}} = \mathbf{r}$ , or rotational space,  $d_{\text{conf}} = \varphi$ , or any other description of atomic configuration, one will find a succession of energy valleys and hills of different depths or heights, respectively. The most simple unit is schematically shown in Fig. 2.5. It is made up of two neighbouring wells which are separated by a potential barrier of height  $V_b$ . The two wells are not necessarily symmetric but can in general differ in their potential minimum by the *asymmetry energy*  $\Delta$ . The shape of the individual wells can be approximated by a *harmonic potential* of the form

$$V_{\text{harm}} = V_{0,l/r} + \xi(d_{\text{conf}} \pm d_{\text{conf},0})^2 \quad (2.3)$$

if only the first terms up to second order of a Taylor expansion around the potential minima  $V_{0,l/r}$  are taken into account where  $\xi$  determines the curvature of the well. Solving for the energy states of a particle with mass  $m$  in such a harmonic potential, as can be found in many textbooks e.g. [Mes05, p. 722], one obtains equally spaced energy levels

$$E_n = \hbar\Omega \left( \frac{1}{2} + n \right), \quad n \in \mathbb{N}_0 \quad (2.4)$$

with the resonance frequency

$$\Omega = \sqrt{\frac{2\xi}{m}}. \quad (2.5)$$

At low temperatures  $T \ll \hbar\Omega/k_B$  only the ground state of the well is occupied. Bringing two of these wells in proximity the wave function  $\Psi_l$  of the particle in the left well has a finite value in the right well and vice versa as it decays exponentially inside the energy barrier. Restricting ourselves to one-dimensional real space with  $d_{\text{conf}} = x$ , where the distance between the minima  $d_{\text{conf},0}^r - d_{\text{conf},0}^l = d$  is estimated to be smaller than  $20 \text{ \AA}$  [Sch76], the time independent

Schrödinger equation for this system can be written as

$$\tilde{E}\Psi(x) = \tilde{\mathcal{H}}_0\Psi(x) = \left(-\frac{\hbar^2}{2m}\frac{d^2}{dx^2} + V(x)\right)\Psi(x). \quad (2.6)$$

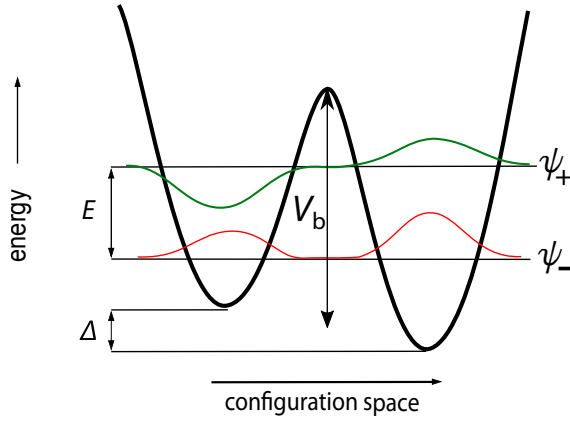


**Figure 2.6:** The overlap of the single well wave functions in both wells leads to the formation of new states  $\Psi_+$  and  $\Psi_-$ , which are separated by the energy splitting  $E$ . The position probability  $\langle\Psi|\Psi\rangle$  is now spread over both wells leading to a delocalisation of the particle (adapted from [Klo08]).

The eigenstates and eigenenergies of Eq. (2.6) will be altered since the potential of Eq. (2.4) entering the equation must be replaced by the combined potential function. In order to avoid the knowledge of the exact shape of the double well we can treat the existence of the barrier as a weak perturbation and the new wave functions as appropriately formed superpositions of the single-well wave functions. This problem is well known and was analysed amongst others by [Nar70] for the case of ion impurity tunnelling in crystals. Making use of the *Wentzel-Kramers-Brillouin approximation* (WKB) one obtains for the wave functions in the left or respectively right well

$$\Psi_{l/r}(x) = \left(\frac{4\lambda}{\pi d^2}\right)^{\frac{1}{4}} \exp\left(-\frac{\lambda}{2}\left(\frac{2x}{d} \pm 1\right)^2\right) \quad (2.7)$$

with the *tunnelling parameter*

$$\lambda = \frac{\xi d^2}{2\hbar\Omega} \approx \sqrt{\frac{mV_b d^2}{2\hbar^2}}. \quad (2.8)$$

Since the mixing of the states needs to preserve the normalisation of the basis vectors a simple way to obtain mixed states  $\Psi_{\pm}$  is a rotation by an angle  $\varphi$  so that

$$\begin{pmatrix} \Psi_+ \\ \Psi_- \end{pmatrix} = \begin{pmatrix} \cos(\varphi) & \sin(\varphi) \\ -\sin(\varphi) & \cos(\varphi) \end{pmatrix} \begin{pmatrix} \Psi_l \\ \Psi_r \end{pmatrix} \quad (2.9)$$

or in index notation  $\Psi_{\alpha} = R_{\alpha i}(\varphi)\Psi_i$  using the Einstein sum convention with  $\alpha \in \{+, -\}$  and  $i \in \{l, r\}$ . Multiplying the Schrödinger Eq. (2.6) with the dual vector and integrating using the normalisation condition  $\langle\Psi_i|\Psi_i\rangle = 1$  we arrive in the left-and-right basis at

$$0 = |\Psi\rangle\langle\Psi|\tilde{\mathcal{H}}_0|\Psi\rangle - \tilde{E}|\Psi\rangle\langle\Psi| = \frac{1}{2} \begin{pmatrix} \hbar\Omega + \Delta & -\Delta_0 \\ -\Delta_0 & \hbar\Omega - \Delta \end{pmatrix} - \tilde{E} \begin{pmatrix} 1 & e^{-\lambda} \\ e^{-\lambda} & 1 \end{pmatrix}. \quad (2.10)$$

As a convention the *tunnelling splitting*  $\Delta_0 = \hbar\Omega e^{-\lambda}$  is used to reparametrise the tunnelling parameter. Solving this eigenvalue problem one finds the two solutions of the eigenenergies

of the combined well

$$\tilde{E}_{\pm} = \frac{\hbar\Omega}{2} \pm \frac{1}{2}\sqrt{\Delta^2 + \Delta_0^2} := \frac{\hbar\Omega}{2} \pm \frac{1}{2}E \quad (2.11)$$

where the energy difference of the two new states  $E = E_+ - E_- = \sqrt{\Delta^2 + \Delta_0^2}$  is introduced. In the following the constant offset arising from the single well ground mode  $\hbar\Omega/2$  shall be omitted for the sake of compactness since it does not alter the dynamics of the system. In the basis of the individual wells Eq. (2.6) then becomes

$$\mathcal{H}_0\Psi = \frac{1}{2} \begin{pmatrix} E & 0 \\ 0 & -E \end{pmatrix} \Psi. \quad (2.12)$$

In order to find the corresponding states  $\Psi_{\pm}$  the mixing angle  $\varphi$  from Eq. (2.9) can be calculated by solving

$$\tilde{\mathcal{H}}_0 = R^{-1}(\varphi)\mathcal{H}_0R(\varphi) = R(-\varphi)\mathcal{H}_0R(\varphi) \quad (2.13)$$

which yields

$$\varphi = \frac{1}{2} \arctan\left(\frac{\Delta_0}{\Delta}\right). \quad (2.14)$$

The mixed states are shown in Fig. 2.6. The atom is no longer localised in one well but can be found in either well. Since one well has a lower minimum energy, the ground state  $\Psi_-$  has a higher amplitude in this well than in the other one and vice versa for the excited state  $\Psi_+$ .

#### 2.1.4 The Standard Tunnelling Model

The derivations of the previous section by themselves do not explain anything about the peculiar behaviour of glasses. The merit of Anderson, Halperin and Varma [And72] and Phillips [Phi72], who first formulated the Standard Tunnelling Model (STM), was to take the established knowledge of a single atom in a double well potential and to combine this with further assumptions on the structure of glasses. They claimed that there was an additional degree of freedom which was responsible for the unexpected non-phononic contribution in the low-temperature specific heat and thermal conductivity, cf. Fig. 2.1. According to them this local mode was a set of atomic two-level systems (TLS), i.e. atoms or groups of atoms confined in a double-well, that dominate the low-temperature properties of glasses. Certainly, as we are dealing with a random network the defining parameters of such TLS, that is  $\Delta$  and  $\lambda$ , will not be the same for all TLS of the sample. The second important assumption was then to take the distribution  $p$  of the asymmetry energy and tunnelling parameter to be uniform.

A Jacobian transformation to the energy splitting  $E = E(\Delta, \Delta_0)$  and the tunnelling splitting  $\Delta_0 = \Delta_0(\lambda)$  yields

$$\begin{aligned} p(\Delta, \lambda)d\Delta d\lambda &= p_0 d\Delta d\lambda \\ &= p_0 \frac{E}{\Delta_0 \sqrt{E^2 - \Delta_0^2}} d\Delta_0 dE \\ &= p(\Delta_0, E) d\Delta_0 dE \end{aligned} \quad (2.15)$$

as plotted in Fig. 2.7.

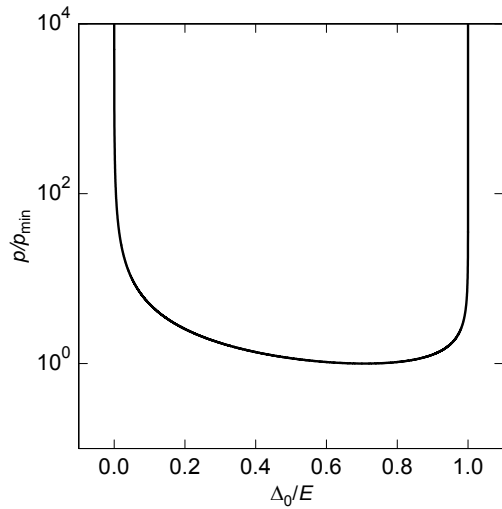


**Figure 2.7:** The distribution of TLS  $p(\Delta_0, E)$  diverges for  $\Delta_0 \rightarrow 0$  and  $\Delta_0 \rightarrow E$ . The latter singularity is integrable unlike the first one which is why a minimum tunnelling splitting  $\Delta_{0,\min}$  is required as lower integration boundary.

Note that the distribution function diverges both for  $\Delta_0 \rightarrow 0$  and  $\Delta_0 \rightarrow E$  which makes it necessary to restrict the integration at some minimum tunnel splitting  $\Delta_{0,\min}$  whenever macroscopic quantities of a material are to be calculated. The exact choice of  $\Delta_{0,\min}$  does not influence the result of the integration provided that  $\Delta_{0,\min} \ll k_B T$  if  $T$  is of the order of the temperature scale of interest. This suffices to derive a linear term in the specific heat. The internal energy of a single TLS is given in the canonical ensemble as

$$U = \frac{1}{Z} E \exp\left(-\frac{E}{k_B T}\right) = \frac{E \exp\left(-\frac{E}{k_B T}\right)}{1 + \exp\left(-\frac{E}{k_B T}\right)} \quad (2.16)$$

with the partition function  $Z = \sum_i \exp(-E_i/(k_B T)) = 1 + \exp\left(-\frac{E}{k_B T}\right)$ . The specific heat follows as

$$c_V = \int_{E_{0,\min}}^{\infty} dE p(\Delta_0, E) \frac{\partial U}{\partial T} \quad (2.17)$$

$$= \int_{E_{0,\min}}^{\infty} dE \frac{E^2}{k_B T^2} \exp\left(-\frac{E}{k_B T}\right) \frac{1}{\left(1 + \exp\left(-\frac{E}{k_B T}\right)\right)^2} \quad (2.18)$$

$$\sim \frac{\pi^2}{6} k_B^2 T p_0. \quad (2.19)$$

Anderson et al. integrated only with respect to  $E$  arguing that  $p$  was almost constant on the relevant energy scale of TLS that contribute to  $c_V$ . The anomalous thermal conductivity can also be explained by this model. Acoustic phonons with frequency  $\omega$  scatter resonantly at TLS with an energy splitting that matches their frequency. Using the STM the mean free path of phonons, which carry the heat since the TLS are non-mobile excitations, becomes restricted to

$$\ell = \frac{1}{\sigma p} \propto \omega^{-1} \quad (2.20)$$

where  $\sigma$  stands for the scattering cross section. Along with the dominant phonon approximation stating that  $\hbar\omega \sim k_B T$  the measured temperature dependence is found:

$$\kappa = \frac{1}{3}c_V v \ell \propto T^3 T^0 T^{-1} = T^2. \quad (2.21)$$

### 2.1.5 Frequency Response of Amorphous Samples

**Analogy to Spin Systems** So far we have only considered static phenomena in glasses, that means a situation in which the occupation of the two levels agrees with thermal equilibrium on temporal average. Applying an external field  $\tilde{e}$  to the sample changes the energetic configuration of the TLS. If we make the whole sample oscillate or couple an ultrasonic transducer to it  $\tilde{e}(t) = e(t) = e_0 \sin(\omega t)$  will be a strain field  $e$  of a certain frequency  $f = \omega/(2\pi)$ . That means we probe the sample with phonons. The strain wave changes the displacement of the atoms periodically which in turn changes the asymmetry energy. To a minor extent the tunnelling splitting is altered as well which is a much weaker effect, though, and thus usually neglected because of its exponential suppression [Phi87]. For sufficiently small driving amplitudes the response is linear and can be written as

$$\delta\Delta(t) = 2\gamma e(t), \quad \delta\Delta_0 \approx 0, \quad (2.22)$$

where the coupling strength of phonons to TLS  $\gamma$ , whose tensor character has been omitted, is typically of the order of 1 eV (e.g. in BK-7  $\gamma_l = 0.35$  eV and  $\gamma_t = 0.24$  eV [Hun75] for the longitudinal and the transversal phonon branches, respectively). The change in asymmetry energy alters the level splitting  $E$  as well by an amount

$$\delta E \approx \frac{\Delta}{E} \delta\Delta. \quad (2.23)$$

The unperturbed Hamiltonian of Eq. (2.10) must now be amended by the perturbation Hamiltonian  $\tilde{\mathcal{H}}_{\text{pert}}$ . In the single-well basis we obtain

$$\tilde{\mathcal{H}} = \tilde{\mathcal{H}}_0 + \tilde{\mathcal{H}}_{\text{pert}} = \frac{1}{2} \left( \begin{pmatrix} \Delta & -\Delta_0 \\ -\Delta_0 & -\Delta \end{pmatrix} + \begin{pmatrix} \delta\Delta & -\delta\Delta_0 \\ -\delta\Delta_0 & -\delta\Delta \end{pmatrix} \right) \approx \frac{1}{2} \begin{pmatrix} \Delta + \delta\Delta & -\Delta_0 \\ -\Delta_0 & -\Delta - \delta\Delta \end{pmatrix}. \quad (2.24)$$

Transforming into the basis of the eigenstates as in Eq. (2.13) we arrive at

$$\mathcal{H} = \mathcal{H}_0 + \mathcal{H}_{\text{pert}} = \frac{1}{2} \begin{pmatrix} E & 0 \\ 0 & -E \end{pmatrix} + \frac{1}{2E} \begin{pmatrix} \Delta & \Delta_0 \\ \Delta_0 & -\Delta \end{pmatrix} \delta\Delta. \quad (2.25)$$

Following the treatment of Hunklinger and Arnold [Hun76] who first identified the Hamilton operator in Eq. (2.25) with the Hamiltonian of a spin- $\frac{1}{2}$  particle in an external magnetic field, one can make use of the formal analogy between these two equations. With the Pauli matrices

$$\sigma_x = \begin{pmatrix} 0 & 1 \\ 1 & 0 \end{pmatrix}, \quad \sigma_y = \begin{pmatrix} 0 & -i \\ i & 0 \end{pmatrix}, \quad \sigma_z = \begin{pmatrix} 1 & 0 \\ 0 & -1 \end{pmatrix} \quad (2.26)$$

Eq. (2.25) becomes

$$\mathcal{H} = \frac{1}{2} E \sigma_z + \frac{\delta\Delta}{2E} (\Delta \sigma_z + \Delta_0 \sigma_x) = \frac{1}{2} \left( E + \frac{\Delta}{E} \delta\Delta \right) \sigma_z + \frac{\Delta_0}{2E} \delta\Delta \sigma_x. \quad (2.27)$$

Hence, the TLS essentially behaves like a spin- $\frac{1}{2}$  particle with a (formal) gyromagnetic ratio  $\tilde{\gamma}$  in a (formal) static magnetic field  $\mathbf{B}_0$  that is perturbed by an oscillating magnetic field  $\mathbf{B}_1$  with

$$\mathbf{B}_0 = -\frac{1}{\hbar\tilde{\gamma}}(0, 0, E), \quad \mathbf{B}_1 = -\frac{2}{E\hbar\tilde{\gamma}}(\Delta_0, 0, \Delta)\gamma e. \quad (2.28)$$

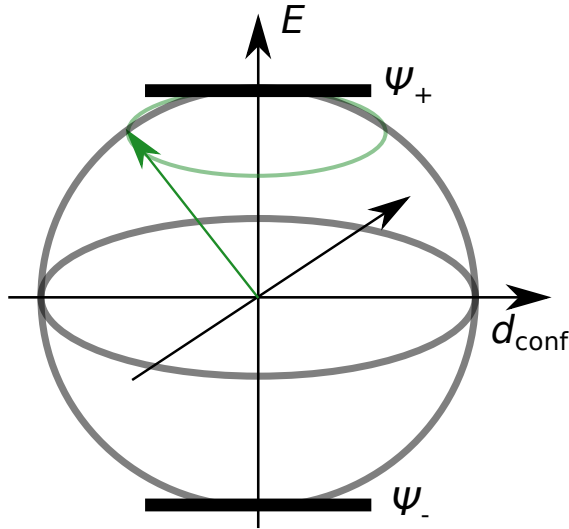


**Figure 2.8:** The phase of the TLS, which is represented by the green arrow, changes periodically as a consequence of the Larmor precession in a static field  $\mathbf{B}_0$ . This can be imaged as a motion around the (formal)  $z$ -axis of a Bloch sphere. The external driving field  $\mathbf{B}_1$  can induce transitions between the lower and upper energy levels  $\Psi_-$  and  $\Psi_+$  or formation of superposition states.

In the case of spin particles  $\mathbf{B}_0$  makes them precess around the  $z$ -axis, i.e. changes the phase of the wave function, and lifts the degeneracy of the two levels by Zeeman splitting.  $\mathbf{B}_1$  on the other hand causes transitions between the lower and upper energy levels. The same applies to the TLS with the sole difference that here no external static field is required. The occurrence of the intrinsically present separate energy states are caused by the asymmetry of the double well potential together with the chance to tunnel between the wells. The spin components  $\langle S_i \rangle$  correspond to a vector inside a *Bloch sphere* with the north (south) pole being the upper (lower) energy state  $\Psi_+$  ( $\Psi_-$ ) as illustrated in Fig. 2.8.

The analogy can be taken one step further to derive an expression for the susceptibility, i.e. the AC response of a TLS to a probing field. Rewriting the contribution of the internal energy of  $N$  identical tunnelling systems  $u = -N\hbar\tilde{\gamma}\mathbf{B}(t) \cdot \langle \mathbf{S}(t) \rangle$  to the dynamical elastic constant  $\delta\mathcal{C} = 1/e \partial u / \partial e$  yields

$$\delta\mathcal{C}(\omega) = \frac{2N\tilde{\gamma}}{eE}(\Delta_0 \langle S_x \rangle + \Delta \langle S_z \rangle) = -\frac{4N\tilde{\gamma}^2}{E^2}(\Delta_0^2 \chi_x(\omega) + \Delta^2 \chi_z(\omega)). \quad (2.29)$$

In the last step the dynamic susceptibilities  $\chi_i = S_i / (\hbar\gamma B_i)$ , that relate the spin response to an applied  $B$ -field, were used. The elastic constant  $\mathcal{C}$  is a complex quantity and thus not directly accessible in experiments. In order to obtain measurable quantities we have to separately consider the real part, which is connected to the relative change of the speed of sound  $\frac{\delta v}{v}$ , and the imaginary part, which is linked to the internal friction  $Q^{-1}$ :

$$\frac{\delta v}{v}(\omega) = \frac{1}{2\rho v^2} \Re(\delta\mathcal{C}(\omega)), \quad Q^{-1}(\omega) = \rho v^2 \Im(\delta\mathcal{C}(\omega)), \quad (2.30)$$

where  $v$  is the speed of sound in the material without TLS interactions and  $\rho$  its mass density.

**Solution of the Bloch Equations** In order for Eq. (2.29) to yield quantitative results the temporal evolution of the spin components has to be deduced. It is described by the Bloch Equations (2.31), first derived in [Blo46]:

$$\frac{d\langle\mathbf{S}\rangle}{dt} - \gamma\langle\mathbf{S}\rangle \times \mathbf{B} + \begin{pmatrix} \tau_2^{-1} & 0 & 0 \\ 0 & \tau_2^{-1} & 0 \\ 0 & 0 & \tau_1^{-1} \end{pmatrix} \langle\mathbf{S}\rangle - \tau_1^{-1} \begin{pmatrix} 0 \\ 0 \\ S'_z \end{pmatrix} = 0 \quad (2.31)$$

where  $S'_z = \frac{1}{2} \tanh(\hbar\tilde{\gamma}B_z/(2k_B T))$  is the equilibrium value for the magnetisation along the  $z$ -axis,  $\tau_1$  the longitudinal or spin-lattice and  $\tau_2$  the transversal or spin-spin relaxation time. These time constants measure how fast the system loses energy either to the lattice, e.g. by the interaction with phonons, or to other surrounding spins, e.g. via flip-flop processes, respectively. Fourier transforming Eq. (2.31) and changing to transverse variables  $S_{\pm} = S_x \pm iS_y$  a series of calculations yield as a final result four equations for the real and imaginary part of the transverse and the longitudinal variables. They can be identified with *resonant interaction* stemming from  $\chi_{\pm}(\omega)$  and *relaxation processes* due to  $\chi_z(\omega)$ :

$$\delta\mathcal{C}_{\text{res}} = -2N\gamma^2 \left(\frac{\Delta_0}{E}\right)^2 \tau_2 \tanh\left(\frac{E}{2k_B T}\right) \left(\frac{1}{i + (\omega_0 - \omega)\tau_2} - \frac{1}{i + (\omega_0 + \omega)\tau_2}\right) \quad (2.32)$$

and

$$\delta\mathcal{C}_{\text{rel}} = 2N\gamma^2 \left(\frac{\Delta}{E}\right)^2 \frac{\text{sech}^2\left(\frac{E}{2k_B T}\right)}{2k_B T} \frac{1}{1 - i\omega\tau_1}. \quad (2.33)$$

Details of the calculation can be found in the literature [Hun76, p. 184–186]. The resonance frequency  $\omega_0 = E/\hbar$  of the TLS is determined by its energy splitting  $E$ .

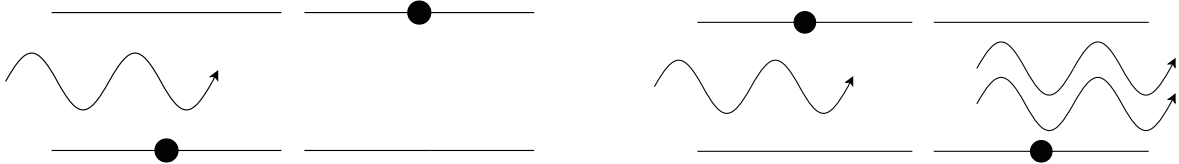


**Figure 2.9:** An external field, e.g. a phonon, interacts resonantly with a TLS via absorption (left) resulting in annihilation of the phonon or via stimulated emission (right) resulting in coherent creation of another phonon (adapted from [Ens05, p. 292]).

**Resonant Processes** As mentioned in the previous paragraph, one way for a strain field to interact with a TLS is via a resonant process. The phonon can either be absorbed by the TLS causing the tunnelling particle to be excited into the upper state or it can stimulate the emission of another phonon when interacting with a TLS that is already in the upper state. Both processes are shown schematically in Fig. 2.9. Separating the real or in-phase and the imaginary or out-of-phase component of the complex resonant elastic constant  $\delta\mathcal{C}_{\text{res}}$  one obtains the two frequency dependencies

$$\Re(\delta\mathcal{C}_{\text{res}}) = -\hat{\mathcal{C}}_{\text{res}} \left( \frac{(\omega - \omega_0)\tau_2^2}{1 + (\omega - \omega_0)^2\tau_2^2} - \frac{(\omega + \omega_0)\tau_2^2}{1 + (\omega + \omega_0)^2\tau_2^2} \right) \quad (2.34)$$

$$\Im(\delta\mathcal{C}_{\text{res}}) = \hat{\mathcal{C}}_{\text{res}} \frac{\tau_2}{1 + (\omega - \omega_0)^2\tau_2^2} - \frac{\tau_2}{1 + (\omega + \omega_0)^2\tau_2^2} \quad (2.35)$$

with the common prefactor

$$\hat{\mathcal{C}}_{\text{res}} = -2N\gamma^2 \left(\frac{\Delta_0}{E}\right)^2 \tau_2 \tanh\left(\frac{E}{2k_B T}\right). \quad (2.36)$$

The physical origin of the two terms in Eq. (2.34) and (2.35) arises from decomposing a linearly polarised incident field into two circularly polarised ones. One of them rotates clockwise and the other one anti-clockwise. One field, the first term in the above equations, can thus be tuned to match the resonance frequency  $\omega_0$  of the TLS leading to a peak in the imaginary part of  $\delta\mathcal{C}$  as can be seen in Fig. 2.10. For a better understanding one can think of a transformation into a co-rotating reference system in which this field component and the TLS are at rest in the Bloch sphere and their phase relation is constant. The larger the

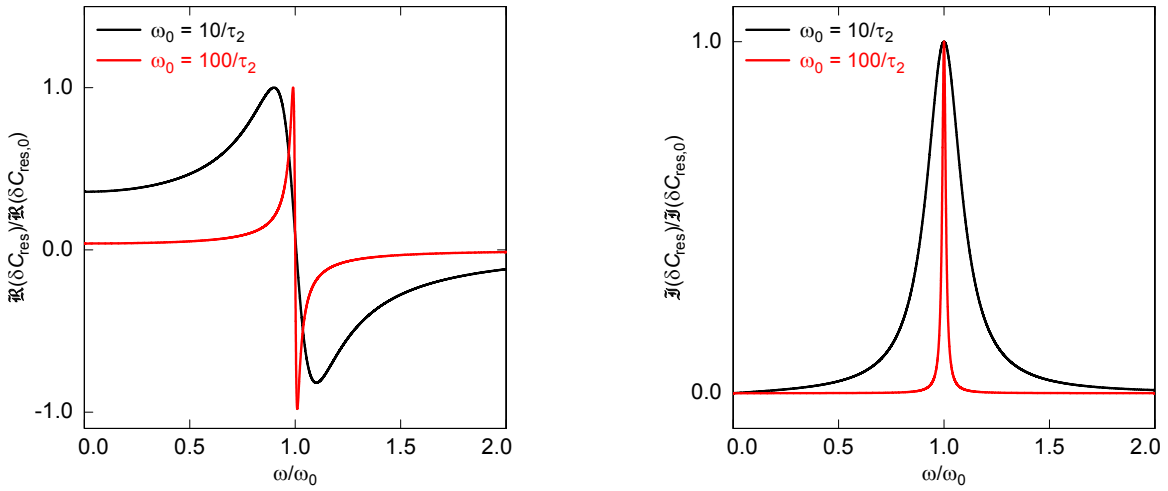


**Figure 2.10:** The real (left) and imaginary (right) part of the resonant contribution to the elastic constant  $\delta\mathcal{C}$  are plotted as a function of the probing frequency  $\omega$  normalised to the resonance frequency of a TLS  $\omega_0$ .

product of resonance frequency and transversal relaxation time  $\omega_0\tau_2$  the more confined to a small frequency interval around  $\omega_0$  are the resonant effects. Evaluating the limits  $\omega \ll \omega_0$  and  $\tau_2^{-1} \ll \omega_0$  one finds

$$\lim_{\omega \rightarrow 0} \Re(\delta\mathcal{C}_{\text{res}}) \propto -\left(\frac{(-\omega_0 - \omega_0)\tau_2^2}{1 + \omega_0^2\tau_2^2}\right) = \frac{2\omega_0}{\tau_2^{-2} + \omega_0^2} \approx \frac{2}{\omega_0} \quad (2.37)$$

$$\lim_{\omega \rightarrow 0} \Im(\delta\mathcal{C}_{\text{res}}) \propto \left(\frac{(1-1)\tau_2}{1 + \omega_0^2\tau_2^2}\right) = 0. \quad (2.38)$$

Hence, even for lowest frequencies the real part still remains finite while the imaginary part dies off. The internal friction can have a non-vanishing value only if there is a difference in the occupation of the two energy levels which is reflected in the factor  $\tanh(E/(2k_B T))$  of Eq. (2.36), derived in appendix A. The lowest temperatures achieved in this work were around  $T_{\text{min}} = 10$  mK which corresponds to a frequency of  $f = E/h = k_B T/h = 200$  MHz. Also, given that all experiments were carried out in the low kHz regime no significant contributions of resonant processes to the internal friction are expected. All TLS that the line shapes (2.35) allow to address exhibit such low level splittings  $E$  that thermal energy suffices to almost equilibrate the occupation, i.e.  $f_{\text{exp}}h \ll k_B T$  with  $f_{\text{exp}}$  being the experimentally employed

frequencies. Another conclusion from the strength of resonant processes can be drawn from the factor  $(\Delta_0/E)^2$ . As  $\Delta_0 \leq E$  we see that symmetric TLS, that is TLS for which  $\Delta \approx 0$  and thus  $\Delta_0 \lesssim E$ , contribute the most to the resonant part of the elastic constant.

The quasi constant density of states is about  $p_0 \sim 10^{20} \text{ cm}^{-3} \text{ eV}^{-1}$  [Las75] so that in an energy range of  $\Delta E = h/\Delta t$ , where  $\Delta t > 10\text{s}$  is the order of time that an external field with a certain frequency is applied to the sample, there are  $n_{\text{TLS}} < \Delta E p_0 \sim 10^5 \text{ cm}^{-3}$  TLS resonant with that field and with each other whose mean distance is  $\bar{s} > n_{\text{TLS}}^{1/3} = 0.02 \text{ cm}$  which is five orders of magnitude larger than atomic spacings. Hence, flip-flop processes that are mediated by dipole-dipole interactions having an  $r^{-3}$ -dependence are strongly suppressed for large separations of the TLS. The transverse relaxation time  $\tau_2$  is thus large enough which justifies the long  $\tau_2$  approximation.

**Relaxation Processes** The second possibility for how the external field can influence the speed of sound and internal friction due to TLS is via relaxation processes. If the level spacing is altered by the action of an external field, as illustrated in Fig. 2.11 this results in a repopulation of the energy levels according to the Boltzmann factor

$$\frac{N_+}{N_-} = \exp\left(-\frac{E + \delta E}{k_{\text{B}}T}\right). \quad (2.39)$$

The use of the Maxwell-Boltzmann instead of the Fermi-Dirac probability distribution is justified since the TLS are well localised and their wave functions scarcely overlap as follows from the above estimation. If the splitting increases some TLS will make transitions from the state of higher to the one of lower energy and vice versa. This assures that on average in the canonical ensemble Eq. (2.39) holds. Again, there is a contribution to the change of the speed

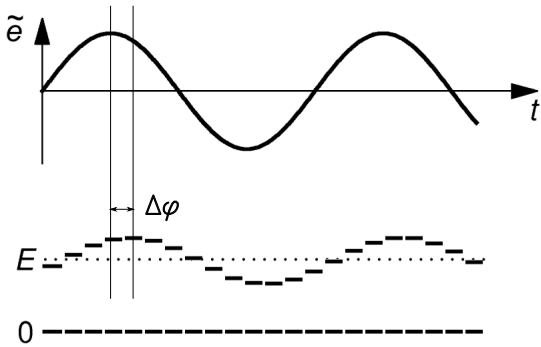


**Figure 2.11:** An external field  $\tilde{e}(t)$  changes the asymmetry energy and thus the energy splitting  $E$  of a system of identical TLS periodically with the same frequency but a lagging phase  $\Delta\phi$  (adapted from [Luc16]).

of sound and absorption coming from the real and imaginary part of Eq. (2.33), respectively,

$$\Re(\delta\mathcal{C}_{\text{rel}}) = -\hat{\mathcal{C}}_{\text{rel}} \frac{1}{1 + (\omega\tau_1)^2} \quad (2.40)$$

$$\Im(\delta\mathcal{C}_{\text{rel}}) = \hat{\mathcal{C}}_{\text{rel}} \frac{\omega\tau_1}{1 + (\omega\tau_1)^2}. \quad (2.41)$$

with the common prefactor

$$\delta\hat{\mathcal{C}}_{\text{rel}} = -\frac{2N\gamma^2}{2k_{\text{B}}T} \left(\frac{\Delta}{E}\right)^2 \text{sech}^2\left(\frac{E}{2k_{\text{B}}T}\right). \quad (2.42)$$

As for the relaxation contribution asymmetric TLS and those having a large potential barrier have the greatest impact since for these ones  $\Delta_0 \ll \Delta$  and therefore  $\Delta \lesssim E$ . If the thermal energy  $k_B T$  is lower than the energy level spacing nearly all TLS occupy the ground state and hence changing the energy splitting remains unnoticed. Only if  $T \geq E/k_B$  can the TLS adapt to the new situation. This behaviour is reflected by the term  $\text{sech}^2(E/(2k_B T))$  which flattens off for  $T < E/k_B$ .

**Debye Relaxator** The line shapes of the change of the speed of sound, the real part, and absorption, the imaginary part, are described by the model of a *Debye relaxator* since the underlying physics is the same as for harmonic oscillators, cf. Section 3.3. The real part reflects the energy saving aspect, i.e. the oscillator or the TLS receives energy from the field and gives it back right away. The imaginary part on the other hand reflects the dissipative aspect, i.e. the received energy is transferred non-coherently to the thermal phonon bath or other relaxation paths. The phase lag  $\Delta\phi$  between an external field and the TLS energy level shift (or between a driving force and a classical oscillator) reflects how much energy is transferred and dissipated. As can be seen in Fig. 2.12 there are three principal frequency regimes. If  $\omega \ll \tau_1^{-1}$  or  $\Delta\phi \approx 0$  the TLS relax much faster than the external field changes which means that they can almost instantaneously restore the preferred thermal occupation numbers. This results in a high impact on the speed of sound causing the low frequency plateau region in the real part, see Fig. 2.12, while no dissipation occurs and the absorption is zero. For resonance condition at  $\omega = \tau_1^{-1}$  or  $\Delta\phi = -\pi/2$  the TLS can receive and deliver energy most effectively resulting in an absorption peak. If the external field changes too fast, though, i.e.  $\omega \gg \tau_1^{-1}$  or  $\Delta\phi \approx -\pi$ , the TLS cannot follow. Hence, no transitions occur and consequently neither speed of sound change nor absorption are observed.

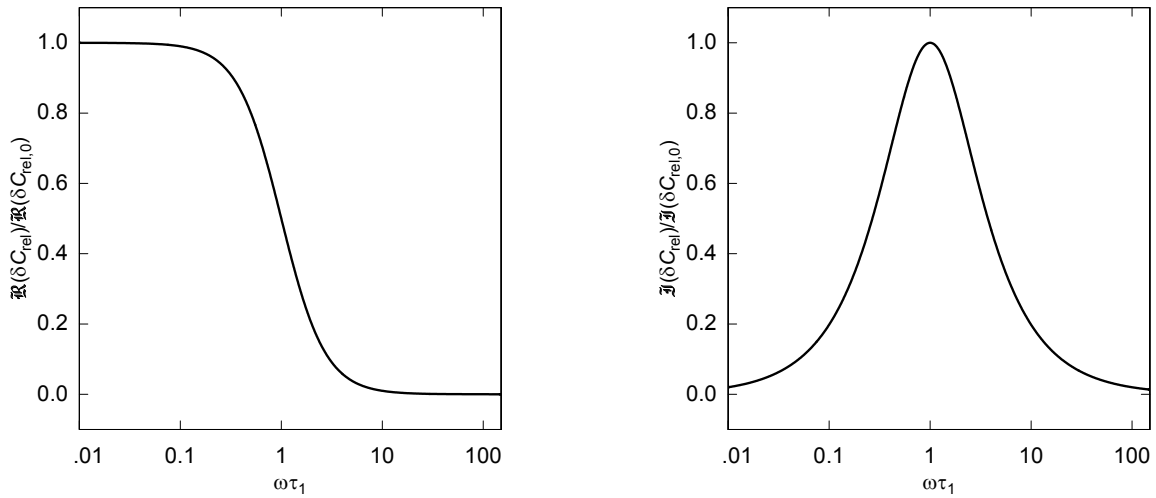


**Figure 2.12:** The real (left) and imaginary (right) part of the relaxation contribution to the elastic constant  $\delta\mathcal{C}$  are plotted as a function of the product of probing frequency and relaxation time  $\omega\tau_1$ .

**Relaxation Mechanisms** The main relaxation mechanism is the interaction of TLS with thermal phonons. As at low temperatures there are only relatively few phonons the most dominant process by which a TLS can relax to thermal equilibrium is the direct process

or *one-phonon process*. From Fermi's Golden Rule

$$W_{\text{if}} = \frac{2\pi}{\hbar} |\langle \Psi_i | \mathcal{H}_{\text{pert}} | \Psi_f \rangle|^2 g(E) n_{\text{BE}}(E, T) \quad (2.43)$$

the transition rate  $W_{\text{if}}$  from initial to final state can be computed [Jäc72]. Here,  $\mathcal{H}_{\text{pert}}$  is the interaction Hamilton operator from Eq. (2.25),  $g(E) = E^2/(2\pi^2\hbar^3v^3)$  the phonon density of states and  $n_{\text{BE}}(E, T) = 1/(\exp(E/k_{\text{B}}T) - 1)$  the Bose-Einstein distribution function. To simplify notation we shall denote the longitudinal relaxation time as  $\tau_1 \equiv \tau$  in the following. The relaxation rate is then the sum of the transition rates in both directions,

$$\tau_{1\text{ph}}^{-1} = W_{\text{if}} + W_{\text{fi}} = \sum_{\alpha} \frac{\gamma_{\alpha}^2}{v_{\alpha}^5} \frac{E\Delta_0^2}{2\pi\hbar^4\rho v^5} \coth\left(\frac{E}{2k_{\text{B}}T}\right), \quad (2.44)$$

where the sum is taken over all phonon polarisations  $\alpha$ , that is two transversal and one longitudinal branch.

At higher temperatures processes involving more than one phonon start to play a role. As calculated by [Dou80] those Raman-like interactions have a very steep temperature dependence:

$$\tau_{2\text{ph}}^{-1} = \frac{k_{\text{B}}^7}{2\pi^3\rho^2\hbar^7} \sum_{\alpha} \frac{\delta_{\alpha}^2}{v_{\alpha}^{10}} \left(\frac{\Delta_0}{E}\right)^2 T^7 F\left(\frac{E}{2k_{\text{B}}T}\right) \quad (2.45)$$

with

$$F(x) = \frac{x}{70} (x^2 + \pi^2) \left(x^4 - \pi^2 x^2 + \frac{10}{3}\pi^4\right) \coth(x). \quad (2.46)$$

Here  $\delta \sim 100$  eV [Dou80] is a multi-phonon coupling constant.

Upon further increasing the temperature higher and higher energy states of the harmonic well become thermally accessible. This on the one hand changes the probability for tunnelling and on the other hand for classically hopping over the barrier [Wür97]. This relaxation mechanism can be described by an *Arrhenius* law:

$$\tau_{\text{th}}^{-1} = \tau_{\text{th},0}^{-1} \exp\left(-\frac{V_{\text{b}}}{k_{\text{B}}T}\right). \quad (2.47)$$

In Fig. 2.13 the temperature dependence of the three mentioned relaxation rates are compared to each other. One observes that symmetric TLS,  $\Delta = 0$ , relax faster than asymmetric ones. Also, multi-phonon and thermally activated processes only play a role for  $T \gtrsim 1$  K depending on the exact set of parameters and their distribution. In vitreous silica the thermally activated relaxation crosses the phonon dominated rate at around 5 K [Tie92]. The total relaxation rate is always the sum of all possible rates

$$\tau^{-1}(T) = \tau_{1\text{ph}}^{-1}(T) + \tau_{2\text{ph}}^{-1}(T) + \tau_{\text{th}}^{-1}(T) + \dots \quad (2.48)$$

For a common dielectric glass, in which there are no conduction electrons that constitute a relaxation channel as in metallic glasses, these three are the main relaxation rates. However, if interactions with additional excitations such as due to nuclear quadrupole moments are allowed one might have to add more rates.

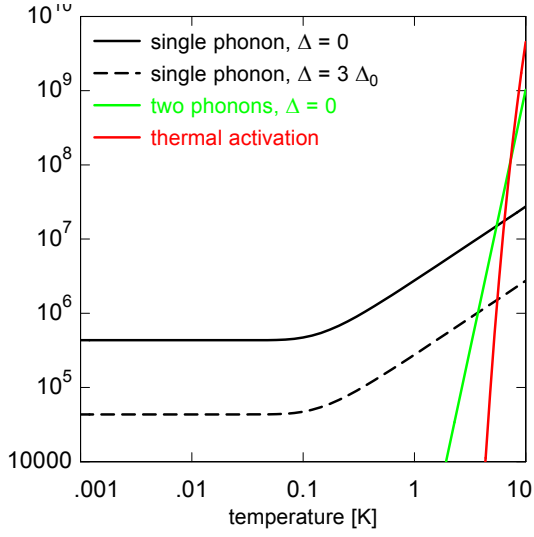


**Figure 2.13:** The longitudinal relaxation rates  $\tau_1^{-1}$  of one-phonon, multi-phonon and thermally activated processes are shown as a function of temperature. One-phonon processes dominate the relaxation at low temperatures. Relaxation in symmetric TLS ( $\Delta = 0$ ) is more efficient than in asymmetric ones.

**Integration of Individual TLS Contributions** Thus far we only have considered the frequency response of  $N$  identical TLS. Yet, in a macroscopic sample TLS with different parameters  $\Delta_0, E$  occur according to the distribution (2.15) and integration with respect to these parameters is required. In the low frequency and large  $\tau_2$  approximation the resonant part of the change of speed of sound follows from Eq. (2.35) to be

$$\left. \frac{\delta v}{v} \right|_{\text{res}} = \frac{p_0 \gamma^2}{\rho v^2} \int_{\Delta_{0,\min}}^{E_{\max}} \frac{dE}{E} \tanh\left(\frac{E}{2k_B T}\right) \int_{\Delta_{0,\min}}^E \frac{d\Delta_0}{\Delta_0} \left(\frac{\Delta_0}{E}\right)^2 \left(1 - \left(\frac{\Delta_0}{E}\right)^2\right)^{-\frac{1}{2}} \approx C \ln\left(\frac{T}{T_0}\right). \quad (2.49)$$

The integral over the tunnelling splitting is solvable analytically. The approximation towards the last expression stems from setting  $E_{\max} \rightarrow \infty$  and acknowledging that the major contribution of resonant processes comes from TLS with  $E \sim k_B T$ , cf. Fig. 2.10. The scale of this logarithmic increase is set by the constant

$$C = \frac{p_0 \gamma^2}{\rho v^2}. \quad (2.50)$$

Since  $\frac{\delta v}{v}$  is merely a relative quantity the reference temperature  $T_0$  is arbitrary. As for the relaxation branch the overall real part result is

$$\left. \frac{\delta v}{v} \right|_{\text{rel}} = C \int_{\Delta_{0,\min}}^{E_{\max}} \frac{dE}{2k_B T} \text{sech}^2\left(\frac{E}{2k_B T}\right) \int_{\Delta_{0,\min}}^E \frac{d\Delta_0}{\Delta_0} \sqrt{1 - \left(\frac{\Delta_0}{E}\right)^2} \frac{1}{1 + (\omega\tau)^2}. \quad (2.51)$$

This integral is not solvable analytically and can only be approximated by numerical methods.

Both contributions to the speed of sound are shown on the left hand side of Fig. 2.14. The temperature at which the relaxation branch flattens off corresponds to the fastest TLS fulfilling the resonance condition with the field  $\omega\tau_{\min} = 1$ . For even lower temperatures their relaxation time becomes yet longer, thus  $\omega\tau > 1$ . They then find themselves in the third regime of Fig. 2.12 where the real part of the Debye relaxator curve vanishes. At high temperatures almost all TLS are sufficiently fast that they are on top of the  $\omega\tau \ll 1$  plateau.

In this limit the integral (2.51) evaluates to

$$\left. \frac{\delta v}{v} \right|_{\text{rel}} \approx -\frac{3}{2}C \ln \left( \frac{T}{T_0} \right) \quad (2.52)$$

so that in total the change of the speed of sound amounts to

$$\frac{\delta v}{v} = \left. \frac{\delta v}{v} \right|_{\text{res}} + \left. \frac{\delta v}{v} \right|_{\text{rel}} = -\frac{1}{2}C \ln \left( \frac{T}{T_0} \right). \quad (2.53)$$

The position of the maximum of  $\frac{\delta v}{v}$

$$T_{\text{max}} = 1.3 \sqrt[3]{\frac{2\pi\rho\hbar^4 \omega}{\sum_{\alpha} \frac{\gamma_{\alpha}^2}{v_{\alpha}^3} k_{\text{B}}^3}} \quad (2.54)$$

can be computed from material parameters and is an appropriate measure for the strength of one-phonon relaxation. The semi-logarithmic slopes far below and above  $T_{\text{max}}$  are thus  $+C$  and  $-C/2$ , respectively. The slope ratio predicted by the STM is therefore  $2 : -1$ .

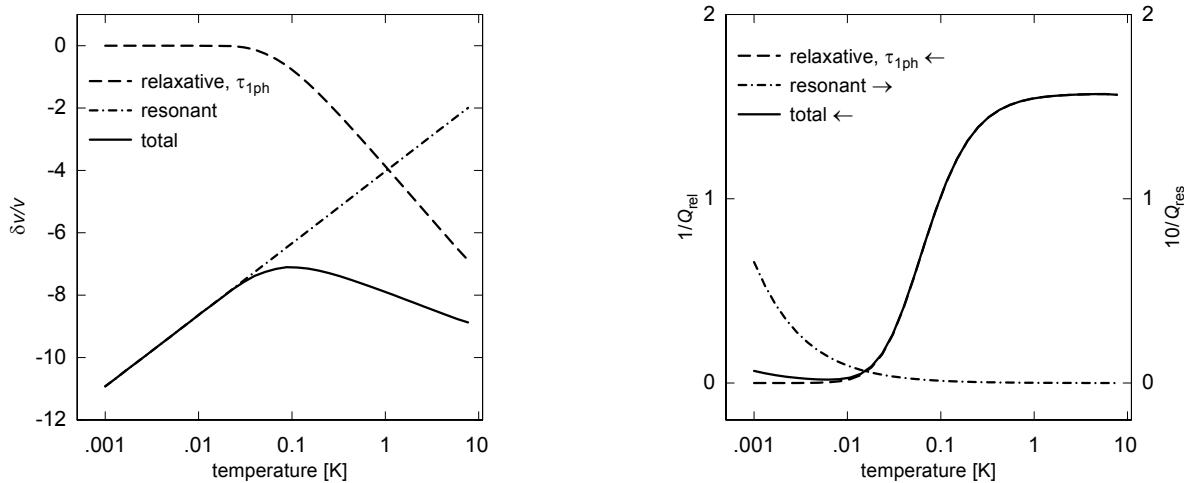


**Figure 2.14:** The numerical results for the relative change of the sound speed (left) and the internal friction (right) are plotted as a function of temperature at a probing frequency of 1 kHz. Note that the resonant internal friction is amplified by a factor of 10 in order to be visible on the view graph.

In the low-frequency and long  $\tau_2$  limit integrating the imaginary resonant part yields

$$\begin{aligned} Q_{\text{res}}^{-1} &= C \int_{\Delta_{0,\text{min}}}^{E_{\text{max}}} dE \int_{\Delta_{0,\text{min}}}^E d\Delta_0 \left( \frac{\Delta_0}{E} \right)^2 \tanh \left( \frac{E}{2k_{\text{B}}T} \right)^2 \\ &\quad \frac{E}{\Delta_0 \sqrt{E^2 - \Delta_0^2}} \left( \frac{\tau_2}{1 + (\omega - \omega_0)^2 \tau_2^2} - \frac{\tau_2}{1 + (\omega + \omega_0)^2 \tau_2^2} \right) \\ &\approx C \frac{\hbar\omega}{2k_{\text{B}}T}. \end{aligned} \quad (2.55)$$

Quantity	Interaction	$T \ll T_{\max}$	$T \gg T_{\max}$
speed of sound	resonant	$C \ln\left(\frac{T}{T_0}\right)$	$C \ln\left(\frac{T}{T_0}\right)$
	relaxation	$\approx 0$	$-\frac{3}{2}C \ln\left(\frac{T}{T_0}\right)$
internal friction	resonant	$\approx 0$	$\approx 0$
	relaxation	$\propto CT^3/\omega$	$\frac{\pi}{2}C$

**Table 2.1:** Summary of the low-frequency temperature dependencies of the speed of sound and internal friction as predicted by the STM.

For the measurements presented here at frequencies  $\hbar\omega \ll 2k_B T$  this is a negligible contribution which barely shows up in Fig. 2.14. The relaxation contribution, however,

$$Q_{\text{rel}}^{-1} = C \int_{\Delta_{0,\min}}^{E_{\max}} dE \int_{\Delta_{0,\min}}^E d\Delta_0 \left(1 - \left(\frac{\Delta_0}{E}\right)^2\right) \text{sech}^2\left(\frac{E}{2k_B T}\right)^2 \frac{E}{\Delta_0 \sqrt{E^2 - \Delta_0^2}} \frac{\omega\tau}{1 + \omega^2\tau^2} \quad (2.56)$$

has a constant plateau value for high temperatures,

$$Q_{\text{rel}}^{-1}(T \gg T_{\max}) \approx \frac{\pi}{2}C. \quad (2.57)$$

It falls off with  $T^3$  to zero at temperatures much lower than  $T_{\max}$  [Esq98, p. 153]. Thus, within the STM the slope of the real part and the plateau of the imaginary part are linked by the constant  $C$ . The different regimes and the corresponding temperature dependencies are summarised in Table 2.1.

The position of the speed of sound maximum shifts by a constant amount for each order of magnitude increase in frequency as given by Eq. (2.54) and so does the turning point of the internal friction as depicted in the semi-logarithmic plot of Fig. 2.15.

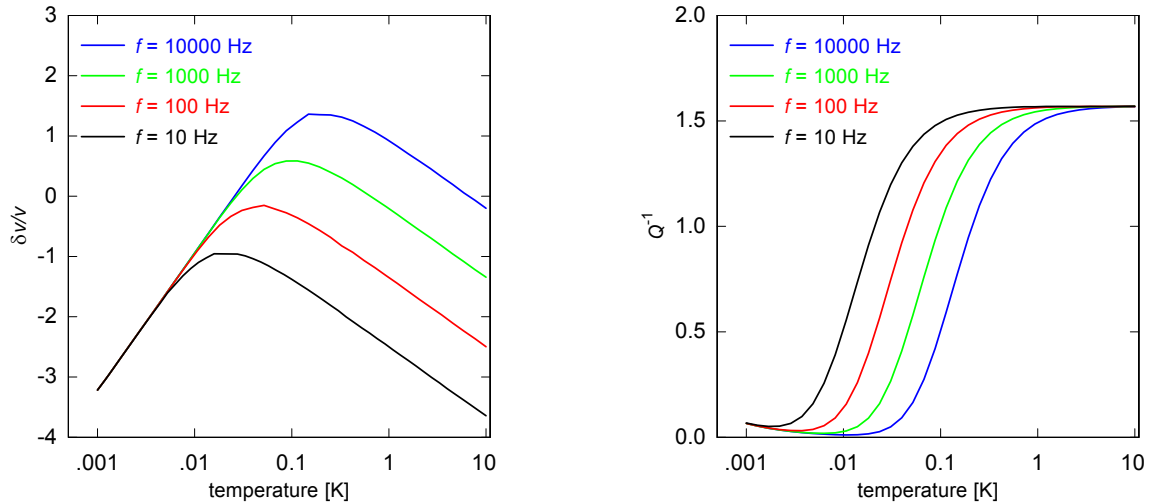


**Figure 2.15:** Varying the probing frequency  $f$  from 10 Hz to 10 000 Hz results in a shift of  $T_{\max}$  towards higher temperatures which is seen both in the speed of sound (left) and absorption (right). For the simulation the constant  $C$  was chosen as 1 so that the plateau lies at  $\pi/2$ .

**Dielectric Constant** The above shown results are formulated for the case of acoustic probing. However, with minor modifications they are equally valid for experiments using electric probing fields. The subset of TLS which carry a charge distribution  $\rho$  and thus a dipole moment

$$\mathbf{p} = \langle \Psi | \rho(\mathbf{r}) \mathbf{r} | \Psi \rangle, \quad (2.58)$$

are susceptible to changes in the surrounding electrical field  $\tilde{\mathbf{e}}(t) = \mathbf{F}(t)$ . In analogy to Eq. (2.22) the asymmetry energy changes by

$$\delta\Delta(t) = 2\mathbf{p} \cdot \mathbf{F}(t). \quad (2.59)$$

Irrespective of the kind of probing the result is a change in  $E$  given by Eq. (2.23). Instead of the dynamic elastic constant  $\mathcal{C}$  and changes thereof, in this scenario one is sensitive to the complex dielectric constant or permittivity  $\varepsilon$ , defined as the susceptibility of the electrical polarisation to an electric field:

$$P_i = (\varepsilon'(\omega) + i\varepsilon''(\omega))_{ij} F_j. \quad (2.60)$$

In the most general case this is a tensor but for the sake of simplicity we will take it to be a scalar. Again, changes in the real part  $\delta\varepsilon'/\varepsilon'$  define the dispersion of electromagnetic waves in the material for the speed of light of a non-magnetic substance is given by  $c = c_0/\sqrt{\varepsilon'}$ . The imaginary part  $\varepsilon''$  describes the absorption, that is the loss of a signal travelling through the material. The latter is often rewritten as the loss tangent  $\tan(\delta) = \varepsilon''/\varepsilon'$ . Therefore, in the case of dielectric measurements the macroscopic coupling constant  $C$  determining the slopes in the real part must be replaced by

$$C \rightarrow C_d = \frac{|\mathbf{p}|^2 p_0}{\varepsilon_0 \varepsilon_r}. \quad (2.61)$$

## 2.2 Nuclear Quadrupole Moments

### 2.2.1 Nuclear Quadrupole Resonance

Atomic nuclei, just like electrons, have a magnetic dipole moment  $\mu = \gamma_n \mathbf{S}_n$ . This arises from their nuclear spin  $|\mathbf{S}_n| = \hbar I$  where  $I \in \{1/2, 1, 3/2, \dots\}$  is the nuclear spin quantum number and  $\gamma_n$  is the gyromagnetic ratio. However, unlike electrons, which are point-like particles, nuclei as a composition of finite sized protons and neutrons exhibit an extended charge distribution  $\rho$ . Therefore, they can have electric moments of higher order in addition to the magnetic dipole moment. Since single nuclei only possess positive charge the dipole moment vanishes and the first non-vanishing electric moment is the quadrupole moment

$$\mathcal{Q} = \langle \Psi | \rho(\mathbf{r}) (3 \cos^2(\vartheta) - 1) r_{\perp}^2 | \Psi \rangle \quad (2.62)$$

where  $(r_{\perp}, \vartheta)$  are cylindrical coordinates with respect to the principal axis of the nucleus. The nuclear quadrupole moment (NQM) has a finite value only in nuclei with a charge distribution that deviates from spherical symmetry. From fundamental symmetry arguments a nuclear quadrupole moment is always an electrical moment. The typical scale of nuclear quadrupole moments ranges from nuclei such as deuteron with  $|\mathcal{Q}_{2D}| = 3 \times 10^{-31} \text{ m}^2 = 3 \text{ mb}$  to nuclei with large NQM such as holmium with  $|\mathcal{Q}_{165\text{Ho}}| = 3.5 \text{ b}$  [Sto05]. An illustration of an oblate, disc-shaped nucleus with  $\mathcal{Q} < 0$  is shown in Fig. 2.16.

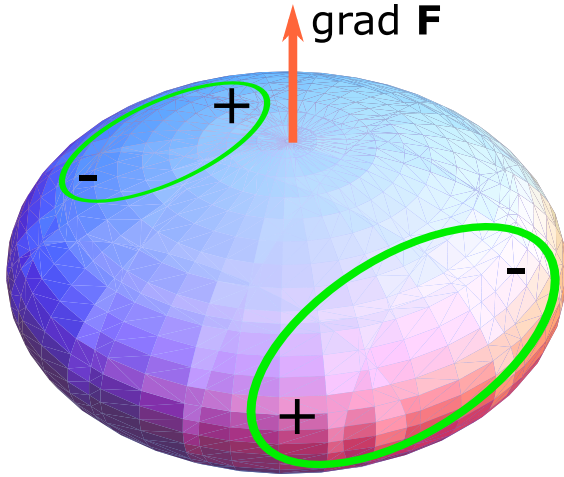


**Figure 2.16:** A non-spherically symmetric nucleus results in an ellipsoidal charge distribution. In a classical picture two anti-aligned dipoles (green) precess around the electric field gradient tensor (orange). Here, the principal axes of the nuclear charge distribution and the electric field gradient are aligned so that  $\vartheta = 0$ .

Following the derivation in [Bol93, ch. 1] a multipole expansion of the interaction between the electric field  $\mathbf{F} = -\mathbf{grad} V$  and the charge of the nucleus yields the quadrupole Hamiltonian

$$\mathcal{H}_q = Q_{ij} \left. \frac{\partial^2 V}{\partial r_i \partial r_j} \right|_{\mathbf{r}=0} := Q_{ij} V_{ij}. \quad (2.63)$$

Here,  $V$  is the electric potential energy and

$$Q_{ij} = \frac{eQ}{6I(2I-1)} \left( \frac{3}{2} (I_i I_j + I_j I_i) - \delta_{ij} I(I+1) \right) \quad (2.64)$$

is the nuclear quadrupole tensor with Kronecker's  $\delta_{ij}$  and the elementary charge  $e$ . Thus, the NQM is by definition only sensitive to changes of the electric field, that is to the electric field gradient (EFG)  $\mathbf{grad} \mathbf{F}$ . It is a tensor quantity but its principal axis is depicted as a vector for the sake of illustration in Fig. 2.16. In order to facilitate calculations one can transform into the principal coordinate system of the field distribution in which the field gradient becomes diagonal, i.e.  $V_{ij} = 0$  for  $i \neq j$ . Laplace's equation

$$0 = \Delta V = V_{xx} + V_{yy} + V_{zz}, \quad (2.65)$$

is applicable here since within the volume of the nucleus no charge generating the test field  $\mathbf{F}$  is present. Thus there remain only two free variables which are usually chosen as

$$eq = V_{zz}, \quad \eta_a = \frac{V_{xx} - V_{yy}}{V_{zz}} \quad (2.66)$$

with the convention  $V_{zz} \leq V_{xx}, V_{yy}$  so that the asymmetry parameter  $\eta_a \leq 1$ . Using perturbation theory the energy levels  $E_m$  of a NQM for the case of an axially symmetric EFG with  $V_{xx} = V_{yy}$  and thus  $\eta_a = 0$  are found to be

$$E_m = \frac{e^2 q Q}{4I(2I-1)} \frac{3 \cos^2(\vartheta) - 1}{2} (3m^2 - I(I+1)) \quad (2.67)$$

where  $\vartheta$  is the angle between the principal axes of the electric field gradient and of the nuclear charge distribution. They are labelled by their magnetic quantum number  $-I \leq m \leq I$  with  $\Delta m = 1$ . The energy levels are thus doubly degenerated due to the  $m^2$  term for  $E_{-|m|} = E_{+|m|}$ . The resonance frequency for transitions between levels with different absolute value of  $|m|$  is

given by

$$\nu_{q,|m-1|\leftrightarrow|m|} = \frac{3e^2qQ}{4I(2I-1)} \frac{3\cos^2(\vartheta) - 1}{2} (2m - 1 - I(I+1)). \quad (2.68)$$

We see that no external magnetic field is required as it is for nuclear magnetic resonance (NMR) spectroscopy because the obligatory level splitting is already intrinsically present thanks to an inhomogeneous electrical field. This can be caused by the local chemical environment of the nucleus, e.g. a covalent bond to a neighbouring atom in a molecule. Once the energy levels are set the same methods and pulse sequences can be applied for this zero-field or pure *nuclear quadrupole resonance* (NQR) as for standard NMR. This allows one to determine relaxation times and line widths by measuring the decay of an echo signal. One can of course combine this technique with NMR and apply a magnetic field  $B_0$  which then lifts the degeneracy of the energy levels by virtue of the *Zeeman effect*:

$$\Delta E_m = \hbar\gamma_n m B_0. \quad (2.69)$$

Depending on how strong the magnetic field is compared to the pure quadrupole splitting the opposite can also be the case, namely that the quadrupole energy shift is a correction to the Zeeman levels. If the nucleus in question happens to be involved in a TLS which already possesses two distinct energy levels then these will split up further in accordance with the corrections from Eq. (2.68) and potentially also from Eq. (2.69). In Fig. 2.17 the level diagram of such a model nucleus is drawn for the case where the tunnelling energy splitting dominates and the Zeeman effect yields the smallest correction.

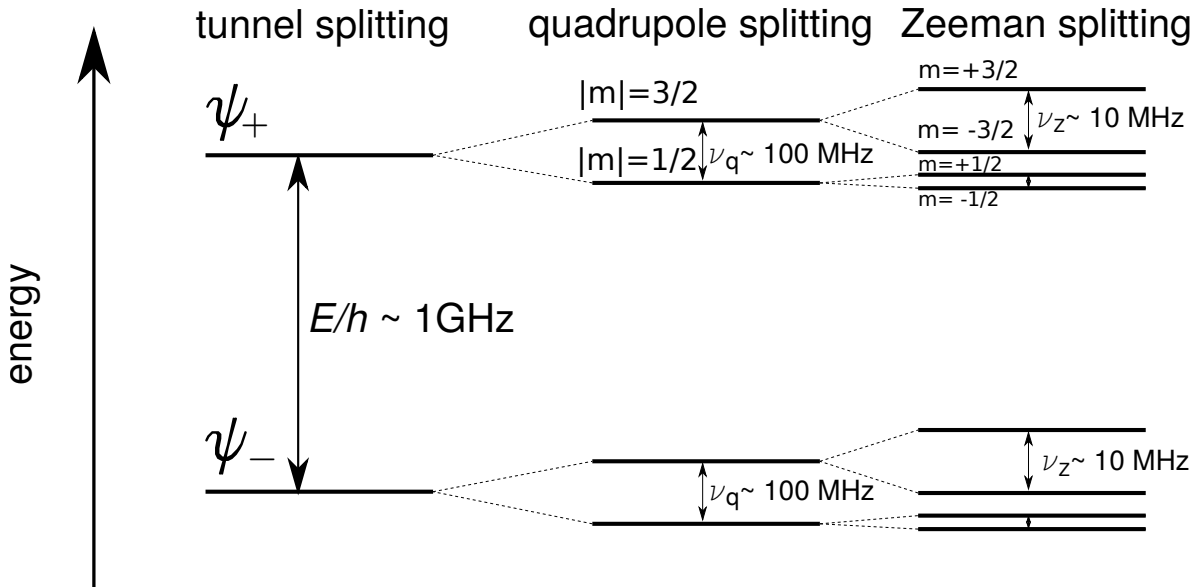


**Figure 2.17:** Energy level diagram of a TLS with an energy splitting of  $E/h \sim 1\text{GHz}$ . The nucleus carries a quadrupole moment. The TLS is additionally exposed to a static magnetic field. The states originating from  $\Psi_-$  are labelled analogously to the ones stemming from  $\Psi_+$ . The order of magnitude of the energy spacings corresponds to a halide compound in a magnetic field of around 1 T.

### 2.2.2 Resonant Susceptibility

First indications of a link between NQM and TLS were found by the observation of a strong magnetic field dependence of spontaneous polarisation echo amplitudes in a non-magnetic amorphous sample [Lud02]. The authors observed that the integrated echo amplitude first decreased a little for small magnetic fields and then increased for rising field even exceeding the zero-field value by a factor of up to three. They concluded that due to the strength of the effect most of the TLS had to take part. Soon after, NQM were identified as a likely cause for this phenomenon. Würger et al. argued that the application of an external magnetic field gradually rotated the quadrupole quantisation axis parallel to the field. The initially misaligned principal axes in the two wells of a TLS would become more and more similar and therefore the dephasing mechanism is reduced due to unmatched quadrupole sublevels [Wür02]. On a scale  $\mu_n B_0 \gg h\nu_q$  the external field completely overrides the effect of the local EFG, which causes the quadrupole splitting, and saturation at a high echo amplitude can occur.

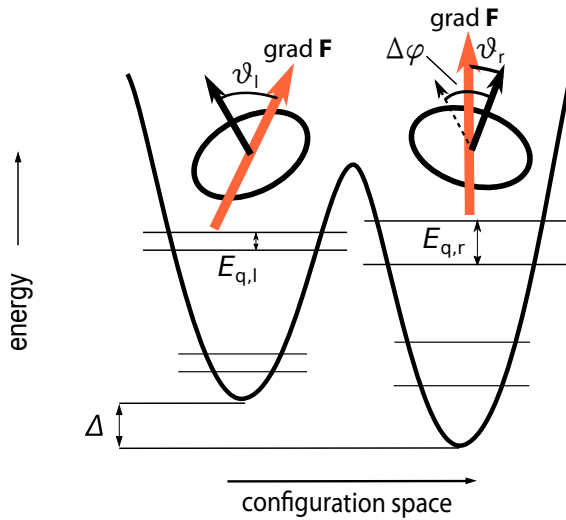


**Figure 2.18:** If the electric environment on the two sides of the double well potential is different or the tunnelling motion involves a rotation of the quadrupole quantisation axis of the nucleus by an angle  $\Delta\varphi$  the angles  $\vartheta_i$  and thus the quadrupole resonance frequency  $\nu_q$  will differ between the two sides (adapted from [Wür02]).

The introduction of this idea into the glass physics community triggered both theoretical and experimental work to predict and test consequences of the novel role that NQM were bestowed upon. One approach is the analysis of the impact of NQM on the resonant contribution to the dielectric and elastic susceptibility. In the limit of highly non-linear but sufficiently slow driving the non-linear resonant susceptibility of the STM can be written as

$$\delta\varepsilon_{\text{res, nl}} \propto \frac{\mathbf{F} \cdot \mathbf{p}}{k_B T} \ln \left( \frac{\mathbf{F} \cdot \mathbf{p}}{\hbar\omega} \right) \quad (2.70)$$

ignoring NQM [Sto95]. This translates to  $\mathbf{F} \cdot \mathbf{p} \gg \Delta_0$ , for non-linear drive, and simultaneously  $\mathbf{F} \cdot \mathbf{p} \omega \hbar \ll \Delta_0^2$ , for assuring that the TLS follow the field adiabatically. What limits the transition rate between the two wells in this scenario is the mismatch between the energy levels on either side. Yet, with NQM interaction there are now more non-degenerate levels separated by  $E_q = h\nu_q$  on both sides which increases the probability that some of them coincide in energy. Hence, if the energy states caused by the quadrupole splitting are resonant with the TLS energy levels the transition probability and the contribution to the susceptibility should increase [Bur06a]. For  $k_B T \ll E_q$  only the lowest lying states are occupied and tunnelling is suppressed due to the misalignment of the principal axes. One expects thus a constant susceptibility. For  $k_B T \gg E_q$  Eq. (2.70) is supplemented by the factor  $E_q/T$ . Experiments on a multicomponent barium aluminosilicate glass indeed found a plateau region in the dielectric

function at very low temperatures below 5 mK [Str00]. Another possibility to explain this plateau would be claiming a minimum tunnelling splitting of  $\Delta_0 \sim 3$  mK. This would be contradictory to measured relaxation times of one week and longer [Sal94], though, since  $\tau_1 \propto \Delta_0^{-2}$ , see Eq. (2.44).

Further work by Burin et al. also addressed the linear resonant susceptibility [Bur06b, Bur06c]. The misalignment between the two wells is quantified in terms of the overlap between the nuclear spin ground state wave functions of the left and right well

$$\begin{aligned} \eta &= \langle \Psi_{s,l} | \Psi_{s,r} \rangle \\ &= \begin{cases} \cos(\Delta\phi) & I = 1 \\ \left| \cos^2(\Delta\phi) - \frac{\sin^2(\Delta\phi)}{2} \right| & I = 2 \end{cases}, \end{aligned} \quad (2.71)$$

where  $\Delta\phi$  is the misalignment angle defined in Fig. 2.18. If  $n$  atoms make up a TLS each of which carries a NQM then the overlap becomes

$$\eta_* = \eta^n \quad (2.72)$$

since the overall wave function can be written as the product of the individual ones.

This has direct consequences for the tunnelling splitting. If the tunnelling process is just a weak perturbation to the quadrupole interaction then a small overlap results in a strong suppression of the tunnelling process. The renormalised tunnelling splitting can be computed to be

$$\Delta_{0*} = \begin{cases} \Delta_0 & \Delta_0 \gg nE_q \\ \eta_* \Delta_0 & \Delta_0 \ll nE_q \end{cases}. \quad (2.73)$$

Hence, a gap is formed in the distribution function of the effective tunnelling splitting

$$p(\Delta_{0*}) < 1, \quad \eta_* nE_q < \Delta_{0*} < nE_q. \quad (2.74)$$

In a simplified model where the NQM are replaced by harmonic oscillators with equal energy spacing  $E_q$  this distribution function can be calculated analytically. It is shown in Fig. 2.19 for different numbers of atoms  $n$  making up a TLS. As expected the gap gets larger for larger  $n$ . The energy at which it opens up is determined by  $E_q$  as can be seen in Fig. B.2 in the appendix. Also, the gap deepens for smaller overlap integrals  $\eta$  and it extends to lower  $\Delta_{0*}$ .

If one integrates the resonant contribution of a generic harmonic oscillator with respect to  $\Delta_{0*}$  using the new distribution (2.74) one retrieves a reduced slope for temperatures below  $h\nu_q/k_B$ . This is demonstrated in Fig. 2.20. Above  $h\nu_q/k_B$  more nuclear spin states than just the ground state are occupied and different transitions become possible. If only the lowest lying states on each side are populated they effectively form a new TLS and the chain of argument is valid. The entire theory is based on the likelihood of resonant transitions that are hindered (or facilitated in the case of adiabatic non-linear driving as explained above) by the NQM interaction. Therefore, it will mostly be TLS with small asymmetry  $\Delta \sim 0$  that contribute to this effect. These, however, hardly contribute to the relaxation part since  $\delta\mathcal{C}_{\text{rel}} \propto \Delta^2$ , cf. Eq. (2.33). This is why this phenomenon is termed anomalous resonant susceptibility and reveals itself only in the resonant part. For low probing frequencies and obtainable temperatures the resonant part has a non-vanishing value only in the real part. The imaginary part, i.e. the internal friction, is not expected to show an anomalous behaviour.

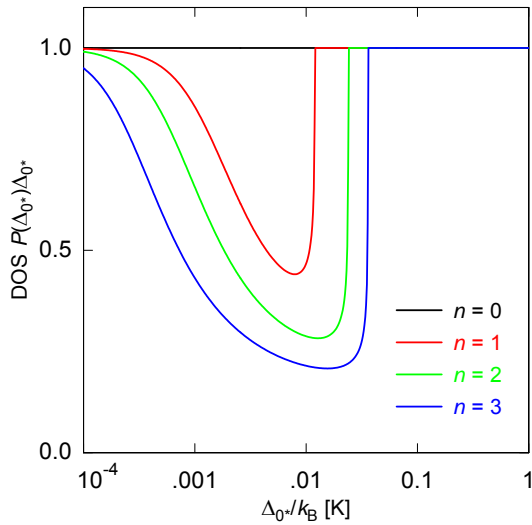


**Figure 2.19:** Logarithmic density of states of TLS at constant overlap integral  $\eta = 0.1$  with varying numbers of atoms  $n$  whose nuclei carry a quadrupole moment with a resonance frequency  $\nu_q = 0.01 k_B/\hbar$  as a function of the renormalised tunnelling splitting  $\Delta_{0*}$ . The black curve,  $n = 0$ , corresponds to the flat distribution of the STM.

Again, the application of an external static magnetic field should restore the resonant slope by aligning the two principal axes of the two wells.

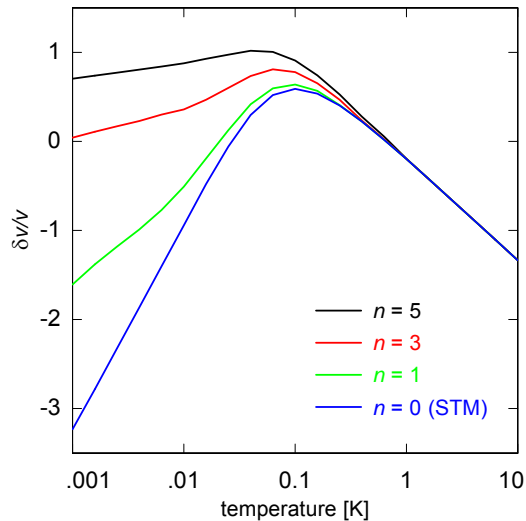


**Figure 2.20:** Changes of the speed of sound for varying numbers  $n$  of quadrupole carrying nuclei that make up one TLS as a function of temperature at constant overlap integral  $\eta = 0.1$  and constant resonance frequency  $\nu_q = 0.01 K k_B/h$ .

### 2.2.3 Relaxation Mechanisms

**Relaxation of Nuclear Spins in Amorphous Samples** Using nuclear magnetic or acoustic resonance techniques one can measure the linewidths of transitions associated with nuclear energy levels arising from Zeeman or quadrupole interactions. The less a nuclear spin ensemble interacts with the environment the longer it remains in a coherent state of defined magnetisation, the narrower the width  $\Delta\nu$  of its resonance peak in a spectrum and the shorter its transverse relaxation time  $T_2 \propto 1/\Delta\nu$ . The longer a spin system remains in the excited state the shorter the longitudinal or spin-lattice relaxation rate  $1/T_1$ . It always holds that  $T_2 \leq 2T_1$ . All time dependent interaction Hamiltonians  $\mathcal{H}_{\text{int}}(t)$  offer possibilities of relaxation whose origin can be severalfold. If a nucleus possesses a quadrupole moment it can interact with the local EFG and changes thereof can cause relaxation as well [Abr61, p. 409]. In those nuclei this is also often the most dominant relaxation mechanism. From time dependent

perturbation theory one finds that the relaxation rates depend on spectral density functions, which are the Fourier transforms of the autocorrelation functions

$$R_{\mathcal{H}_{\text{int}}\mathcal{H}_{\text{int}}}(t) = \int_{-\infty}^{\infty} du \mathcal{H}_{\text{int}}(u+t) \mathcal{H}_{\text{int}}^{\dagger}(u) \quad (2.75)$$

of the underlying fluctuating interactions. An approximated calculation of relaxation rates for the case of a tumbling motion disturbing a nuclear spin was performed by Bloembergen, Pound and Purcell [Blo48]. Their BPP-theory assumes an exponential autocorrelation function proportional to  $\exp(-t/\tau_c)$  where  $\tau_c$  is the correlation time of the motion defining on what time scale the motion starts to appear random. Then, the relaxation rates can be derived as

$$\frac{1}{T_1} = K \left( \frac{\tau_c}{1 + \omega_0^2 \tau_c^2} + \frac{4\tau_c}{1 + 4\omega_0^2 \tau_c^2} \right) \quad (2.76)$$

$$\frac{1}{T_2} = \frac{K}{2} \left( 3\tau_c + \frac{5\tau_c}{1 + \omega_0^2 \tau_c^2} + \frac{2\tau_c}{1 + 4\omega_0^2 \tau_c^2} \right). \quad (2.77)$$

Here,  $\omega_0$  is the resonance frequency of the nuclear spin system, i.e. the Larmor frequency  $\omega_L = \gamma B_0$  for NMR and  $\omega_q$  for NQR, and the coupling factor  $K$  is proportional to the square of the interaction strength, that is  $K \propto (\gamma_n^2/r^3)^2$  for dipolar coupling. As early as 1963, that is ten years before the STM was formulated, Woessner and Gutowsky calculated the corresponding quadrupole relaxation rate assuming that the local EFG was altered by random, large-angle reorientations of groups of atoms [Woe63]. They obtained

$$\frac{1}{T_1} = \frac{e^2 Q^2}{12\hbar^2} \langle (V_{xx}(0) - V_{yy}(0))(V_{xx}^*(0) - V_{yy}^*(0)) \rangle \frac{\tau_c}{1 + \omega_q^2 \tau_c^2}. \quad (2.78)$$

If the tumbling entities are TLS the mathematical set of tools provided by the STM allowed to have a clearer idea about the correlation time of the motion. The nuclear spin relaxation rate caused by TLS following the usual distribution is then given by [Rub75, Est91]

$$\frac{1}{T_1} = K \int_{\Delta_{0,\min}}^{E_{\max}} dE \int_{\Delta_{0,\min}}^E d\Delta_0 \frac{E p_0}{\Delta_0 \sqrt{E^2 - \Delta_0^2} \cosh\left(\frac{\Delta}{2k_B T}\right)} \frac{\tau}{1 + \omega_0^2 \tau^2}. \quad (2.79)$$

The correlation time  $\tau$  in this model is taken as the longitudinal relaxation time of TLS (2.48). In the above cited publications only one-phonon processes, dominant at low temperatures, and thermally activated processes at higher temperatures were taken into account neglecting multi-phonon processes. The TLS can perturb the EFG at the site of the nucleus for instance by displacing or stretching electronic bonds. Thus, the coupling will be predominantly of quadrupole nature, that means  $K \propto Q^2$  and  $\omega_0 = \omega_q$ . Alternatively, if the TLS carries a dipole moment and the nucleus has no quadrupole moment then the coupling will be mainly dipolar, that is  $K \propto \gamma_n^4/r^6$  and  $\omega_0 = \omega_L$ . This Equation (2.79) in the quadrupole case and the relaxation rate of TLS (2.41) are very similar. Both show the frequency dependence of the imaginary part of a Debye relaxator being proportional to  $\omega\tau/(1 + \omega^2\tau^2)$  if the  $\omega$  in the numerator is taken from the coupling factor since  $K \propto Q^2 \propto \omega^2$ . Yet, the meanings of the involved frequency and time constants are different. This demonstrates that the TLS driven relaxation is most effective for  $\omega_q\tau_{\text{TLS}} = 1$ . These considerations were able to explain the low-temperature relaxation rates measured in amorphous samples and in particular the deviations

to corresponding data from crystals. The latter exhibit much longer relaxation times, which are exemplary compared in Fig. B.1, due to their lack of TLS [Sze75, Rub75].

**Relaxation of TLS via Nuclear Quadrupole Moments** From a quantum mechanical point of view TLS and nuclear spins are in certain aspects quite similar to each other in that both systems consist of at least two levels separated by an energy which can be modified by external fields or local effects. Also, both can be described by the Bloch sphere formalism. Hence, the idea is not too far fetched to imagine a relaxation process from TLS to the nuclear bath as suggested by [Luc16] in order to qualitatively explain low-temperature anomalies in samples containing large nuclear quadrupole moments. In this phenomenological model a constant relaxation rate  $\tau_0^{-1}$  between NQM and TLS is assumed which is modulated by the thermal population factor  $\coth(E/(2k_B T))$  and the weighting  $(\Delta_0/E)^2$ . This is motivated by the fact that in the coherent tunnelling regime symmetric TLS should yield the highest contribution as they do for one-phonon relaxation as well, cf. Eq. (2.44). This relaxation mechanism does not extend down to lowest temperatures, though. If the thermal energy becomes smaller than the quadrupole splitting  $E_q$  most nuclear spin systems will occupy the quadrupole ground state and thus will not be able to transfer any energy to the TLS. As relaxation requires both uptake and release of energy depending on where the thermal equilibrium lies relaxation into the nuclear spin bath should decrease below  $E_q/k_B$ . In the model this is incorporated by a cut-off function  $1 - \exp(-(k_B T/(2E_q))^{2a})$  which can be purely exponential,  $a = 0.5$ , Gaussian,  $a = 1$ , or even steeper,  $a > 1$ . All together the quadrupole driven relaxation rate in this empirically motivated model is given by

$$\tau_q^{-1} = \tau_0^{-1} \left( \frac{\Delta_0}{E} \right)^2 \coth \left( \frac{E}{2k_B T} \right) \left( 1 - \exp \left( - \left( \frac{k_B T}{E_q} \right)^{2a} \right) \right). \quad (2.80)$$

If not stated otherwise the parameters that were chosen for the simulations of this section are a quadrupole splitting of  $E_q/k_B = 0.01$  K, a constant rate of  $\tau_0^{-1} = 100$  kHz, a Gaussian cut-off  $a = 1$  and a probing frequency of  $f = 1$  kHz. The nuclear spin driven relaxation rate is compared to the one-phonon processes induced rate in Fig. 2.21 for symmetric and asymmetric TLS. One can see that at temperatures above  $E_q/k_B$  the system is in the nuclear spin dominated relaxation regime. Below, it enters the one-phonon processes governed regime.

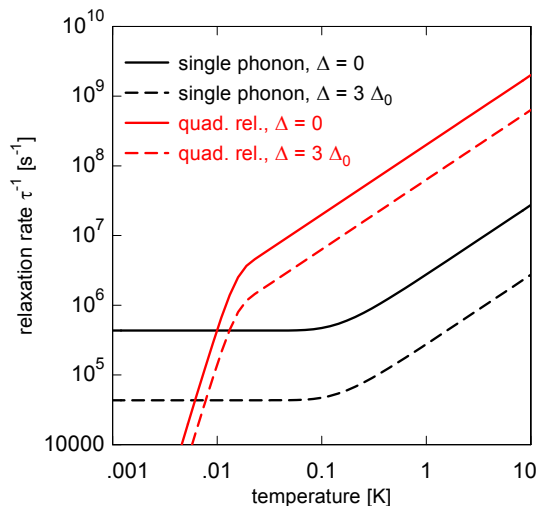


**Figure 2.21:** Relaxation rate by one-phonon processes (black) compared to nuclear quadrupole driven relaxation (red) for two TLS with different asymmetry energy. The energy splitting was in each case  $E/k_B = 1$  mK. The quadrupole driven relaxation rate rapidly decreases below the hyperfine splitting of  $E_q/k_B = 0.01$  K.

The consequences of such a relaxation mechanism for the macroscopic quantities, speed of sound and internal friction, are shown in Fig. 2.22. The relaxation branch displays now two distinct bending features. The first feature marks the temperatures at which the fastest TLS with respect to phononic relaxation meet the resonance condition  $\omega\tau = 1$ . The second one lies at a temperature where this is the case for quadrupole relaxation. Below that temperature the corresponding relaxation process is strongly suppressed. The resonant branch is not affected by this additional relaxation process so that the sum of both branches exhibits two local maxima. The lower one at  $E_q/k_B$  corresponds to NQM driven relaxation and the upper one at  $T_{\max}$  corresponds to the dying out of one-phonon relaxation.

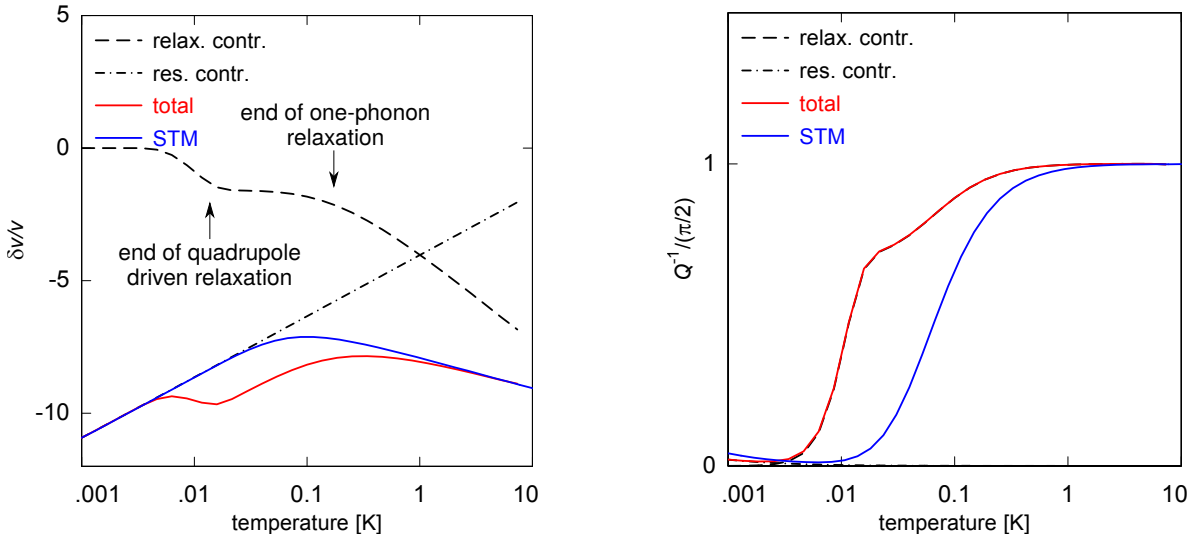


**Figure 2.22:** In the real part (left) the additional nuclear quadrupole driven relaxation causes a second local maximum at a temperature slightly below  $E_q/k_B = 10$  mK. The other maximum, which has shifted from  $T_{\max} = 0.1$  K in the STM case to  $T_{\max} = 0.3$  K is a sign of the end of one-phonon relaxation, cf. Eq. (2.54). In the imaginary part this manifests itself as two plateaus that extend down to those temperatures and add up. The slope beyond the second plateau, i.e. the one caused by NQM, is much steeper than the slope beyond the first plateau because the NQM rate vanishes exponentially while the phonon rate converges to a certain constant value for a given TLS as  $\lim_{T \rightarrow 0} \coth(E/(2k_B T)) = 1$ .

As long as  $E_q/k_B$  is below the temperature of the speed of sound maximum caused by one-phonon relaxation two separate local maxima are distinguishable. If the quadrupole splitting is larger, though, due to nuclei with an enormous quadrupole moment or very strong EFG the second maximum moves to the high temperature side of the phonon maximum and appears only as a slight kink as presented in Fig. 2.23. In this case the position of the phonon maximum also shifts back to where it would have been in an analogous scenario without NQM driven relaxation. If quadrupole relaxation dominates in the temperature interval  $T_{\max} > T > E_q/k_B$  the apparent position of the phonon maximum is not frequency dependent anymore as illustrated in Fig. 2.24. The observation of this effect motivated the formulation of a nuclear spin governed relaxation in the first place. From the known frequency dependence of the Debye relaxator one sees that for  $\omega\tau \ll 1$  the real part is at maximum. At  $\omega\tau = 1$  it starts decreasing towards zero. This is reflected in the fact that the deviation to the STM gets smaller as the probing frequency approaches  $\tau_0^{-1}$  and then completely disappears for  $\omega\tau \gg 1$ . This explains why low-frequency measurements are chosen in order to look for this effect. Increasing the exponent  $a$  leads to a more pronounced second maximum in the real

part and a steeper decrease of the quadrupole plateau in the imaginary part as is summarised in the appendix in Fig. B.4. The magnitude of the constant rate  $\tau_0^{-1}$  also has a positive impact both on the height of the quadrupole maximum in the real and on the level of the quadrupole plateau in the imaginary part as shown in Fig. B.5.

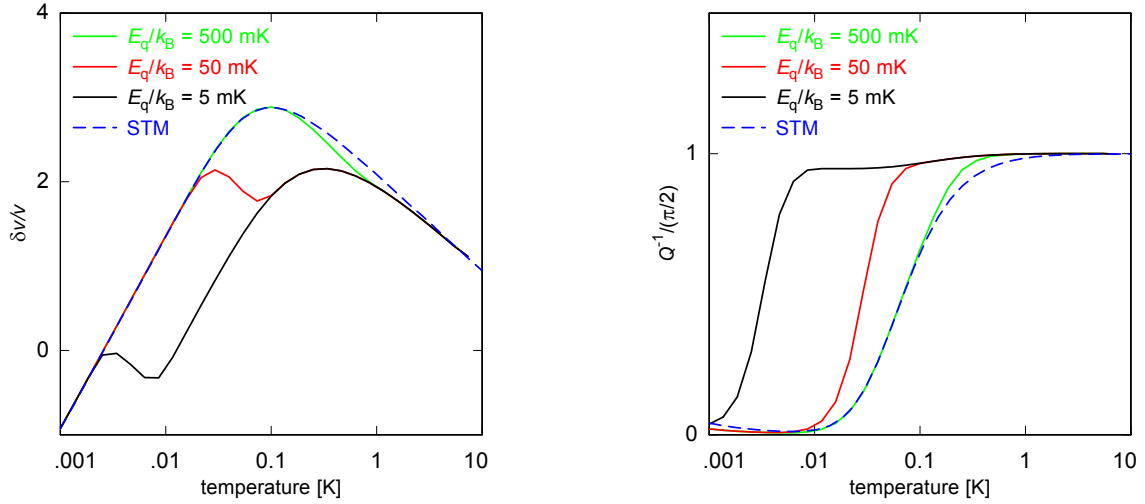


**Figure 2.23:** Varying the quadrupole energy splitting  $E_q/k_B$  from 5 mK to 500 mK shifts the position of the NQM caused local maximum in the speed of sound (left) and the end of the plateau in the absorption (right) to higher temperatures. Note that the curves differ from each other and from the STM only in the temperature interval where merely one relaxation mechanism is present.

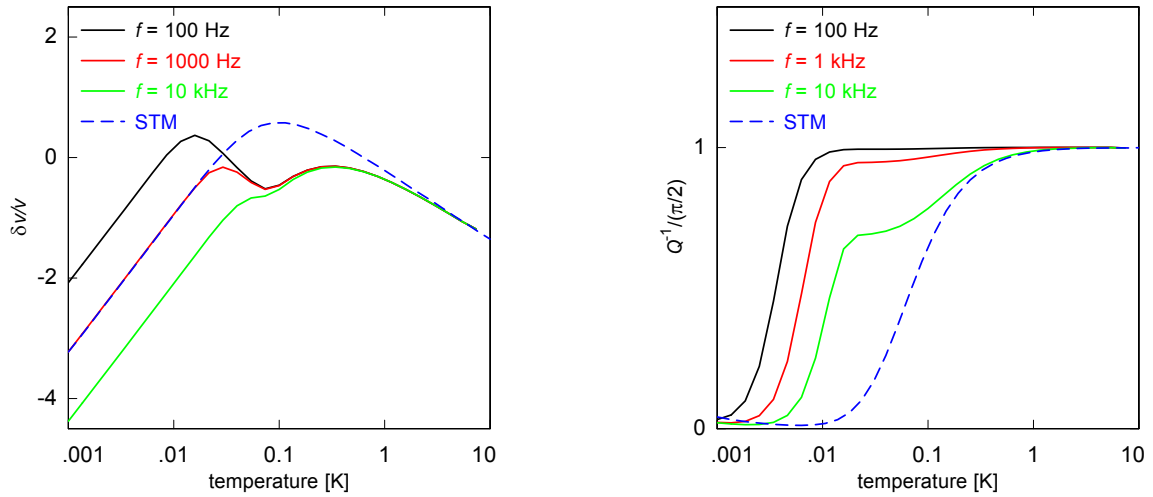


**Figure 2.24:** Varying the probing frequency  $f$  from 100 Hz to 10 000 Hz reduces the height of the NQM caused local maximum in the speed of sound (left) and unveils a second, lower lying plateau in the absorption (right). The STM data were simulated at a frequency of 1 kHz explaining the match of the STM curve with the 1 kHz-curve of the combined relaxation at higher and lower temperatures.

### 3. Experimental Methods

It is only at low temperatures that quantum mechanical tunnelling processes and hence two-level systems become the key player in the dynamics of amorphous solids. The first and foremost requirement for the investigation of the behaviour of these TLS is thus the achievement and monitoring of low temperatures which is the subject of Section 3.1. In Section 3.2 the chemical structure of the investigated sample is elucidated and its physical properties discussed. The set-up and measuring strategy of low-frequency acoustic experiments using a capacitively read-out mechanical resonator are laid out in Section 3.3. The design and characterisation of a novel experimental module offering a chance to drive the nuclear quadrupole transition is subject of Section 3.3.3. The acoustic experiments were complemented by measurements of the dielectric function in a capacitance bridge set-up as explained in Section 3.4.

#### 3.1 Working at Low Temperatures

##### 3.1.1 Cooling Methods

**Cryogenic Substances** In order to reach the required low temperatures for the experiments at hand, when the TLS start to become the dominant degree of freedom, that is the subkelvin regime, sophisticated cooling techniques are of importance. The first step to achieve low temperatures is the use of liquefied gases. To this end the internal energy of the gas has to be reduced until its temperature falls below the boiling temperature  $T_b$ , which is summarised in Table 3.1 for cryogenic substances used in this work.

**Refrigerators** After obtaining liquefied cryogenic substances these can be used to cool down the samples to be investigated when inserted into a cryostat, a device to reach and stabilise well defined low temperatures at its experimental stage. The base temperature  $T_0$  is the lowest achievable temperature of a given cryostat which would be maintained without external disturbances. In order to measure at temperatures greater than  $T_0$  energy is deposited on the experimental stage by an electrical resistance  $R$  through which a heating current  $I$  is sent which defines the heating power

$$P_h = VI = RI^2. \tag{3.1}$$

Substance	$T_b(p = 1 \text{ bar})$ [K]	$T_b(p = 1 \text{ mbar})$ [K]
nitrogen ( $\text{N}_2$ )	77.4	$\approx 50$
helium ( $^4\text{He}$ )	4.21	$\approx 1.1$
helium ( $^3\text{He}$ )	3.19	$\approx 0.6$

**Table 3.1:** The boiling temperatures of three cryogenic substances used in this thesis for cooling down the experiment (1 bar data from [Wei98] and 1 mbar data from [Sch67]).

The difference between the cooling power  $P_c(T)$  of the cryostat and the heating power defines the change in temperature

$$\dot{T} = \frac{P_h - P_c(T) + P_s}{C_V} \quad (3.2)$$

where  $C_V$  is the absolute heat capacity of all parts of the cryostat that are thermally coupled to the experimental platform and  $P_s$  is the stray power from thermal conductance because of insufficient thermal insulation (e.g. due to cables, imperfect vacuum, ...) or incident radiation (e.g. due to surrounding black-body radiation or cosmic rays). The cooling power increases with rising temperature which limits the base temperature to  $P_c(T_0) = P_s$  and allows to set a constant measuring temperature  $T \geq T_0$  by adjusting the heating current.

**Nitrogen Bath Cryostat** For the preliminary high-temperature measurements which served for the validation of the data acquisition software and testing of the acoustic experimental set-up, presented in Section 3.3, a *nitrogen-bath cryostat* was employed which is schematically depicted in Fig. 3.1. The experimental stage is attached to a container with liquid nitrogen so that  $T_0 \approx T_b(\text{N}_2) = 77.4 \text{ K}$ . The container has a volume of about 2 l and has to be refilled with liquid nitrogen approximately every nine hours at base temperature. From this a base temperature cooling rate of this cryostat of

$$P_c = \dot{V} \frac{L\rho}{M} L \approx 20 \text{ W} \quad (3.3)$$

can be estimated where  $L = 5.59 \text{ kJ mol}^{-1}$  [Kay11] is the molar latent heat of evaporation,  $M = 14 \text{ g mol}^{-1}$  is the molar mass and  $\rho = 0.8 \text{ g cm}^{-3}$  [Jen80] is the density of liquid nitrogen at  $T_b$ .

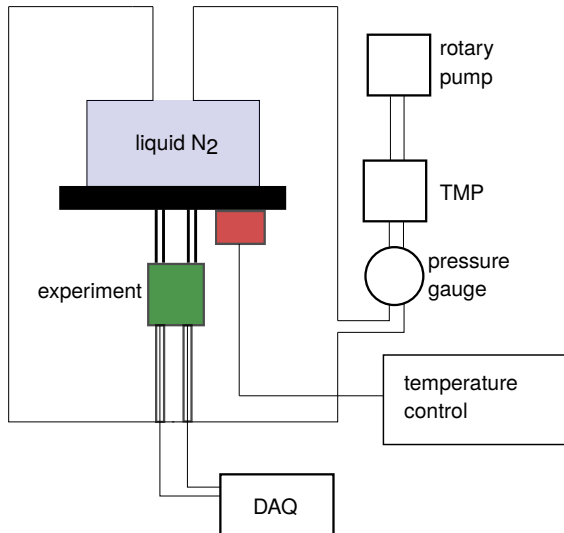


**Figure 3.1:** Schematic set-up of the nitrogen-bath cryostat. The experiment is thermally coupled to a container with liquid nitrogen via four threaded rods of a diameter of 4 mm and a length of 5 cm. Using a rotary vane pump<sup>a</sup> and a turbomolecular pump<sup>b</sup> (TMP) the vacuum chamber is evacuated to a pressure smaller than  $10^{-4}$  mbar. The pressure is monitored by a pressure gauge<sup>c</sup>. With a data acquisition system (DAQ) the experiment is controlled.

<sup>a</sup>TRIVAC D8B, Oerlikon Leybold Vacuum GmbH, Bonner Str. 498, 50968 Cologne, Germany

<sup>b</sup>TurboVac TMP 50, Oerlikon Leybold Vacuum GmbH

<sup>c</sup>Thermovac TM 230, Leybold Vacuum GmbH

**$^3\text{He}/^4\text{He}$  Dilution Cryostat** The main experiments were carried out in a  $^3\text{He}/^4\text{He}$  dilution cryostat as shown in Fig. 3.2. Details of the working principle of such a refrigerator can be found in [Ens05, p. 471–480] and [Pob07, p. 149–188].

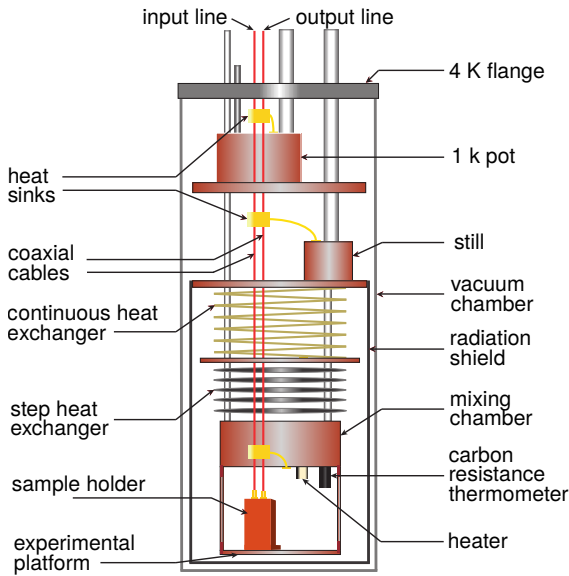


**Figure 3.2:** Schematic set-up of a  $^3\text{He}/^4\text{He}$  dilution cryostat. The outermost part, which is situated inside the helium dewar, is at around 4 K. Evaporation cooling inside the 1 K pot reduces the temperature further and the transition of pure  $^3\text{He}$  into the dilute phase inside the mixing chamber, which is thermally well coupled to the experimental stage, achieves the final temperature reduction to temperatures in the mK range (adapted from [Sch16a]).

If only heat input from warm incoming  $^3\text{He}$  is taken into account the cooling power of a dilution refrigerator is given by

$$P_c = \dot{N}_3 (95T_{\text{mc}}^2 - 11T_{\text{ex}}^2) \left( \frac{\text{J}}{\text{mol K}^2} \right) \quad (3.4)$$

where  $T_{\text{mc}}$  ( $T_{\text{ex}}$ ) is the temperature of the mixing chamber (heat exchanger) and  $\dot{N}_3$  is the  $^3\text{He}$  circulation rate. So besides stray heat input the ultimate limitation of achievable temperatures is determined by the efficiency of the heat exchangers. The cryostat<sup>1</sup> employed for the acoustic experiments was able to reach a base temperature of  $T_0 = 10$  mK as measured by the carbon resistance thermometer, see Section 3.1.2.

Most components of the cryostat, which are to be kept at the lowest temperatures such as the experimental platform, are made from annealed oxygen-free copper because of its good thermal conductivity. The sample holder was firmly attached to the experimental stage by a brass screw. Two semi-rigid coaxial cables are used as input and output lines. Heat sinking is done at the 4 K flange, the 1 K pot, the still and the mixing chamber. The employed heat sinks are gold plated copper boxes with an inner sapphire substrate at the bottom on top of which niobium lines are sputtered. Niobium becomes superconducting at 9.2 K [Ens05, p. 345] while sapphire is a poor electric but rather good thermal conductor. Two subminiature version A (SMA) adapter, which are bonded to the niobium lines, are installed for electric connection to the signal lines on either side of the heat sink. The heat can flow from the heat sink to the copper backbone of the cryostat via gold plated copper links.

### 3.1.2 Thermometry

At high temperatures  $T > 10$  K the temperature of the experimental platform inside the cryostat is recorded by a thermometer<sup>2</sup> which measures the bandgap change of a silicon

<sup>1</sup>Kelvinox 400, Oxford Instruments, Tubney Woods, Abingdon, Oxfordshire, OX13 5QX, UK

<sup>2</sup>331 Temperature Controller, Lake Shore Cryotronics Inc., 575 McCorkle Blvd, Westerville, OH 43082, USA

diode<sup>3</sup>. At low temperatures a carbon resistance thermometer is used which is read out by a resistance bridge<sup>4</sup>. The calibration of the thermometer was done using a noise thermometer which itself was calibrated by a fixed point thermometer [Rei17]. The noise thermometer used for calibration was again employed in the bias measurements, see Section 3.3.3, to obtain a second temperature reading. The reason for using a second thermometer which is based on a different measuring principle is that this way potential stray couplings between the bias signal line and the resistance thermometer, which would otherwise lead to an artefactual recording of a temperature rise, could be ruled out. The working principle of the noise thermometer is based on recording the current  $I$  or voltage  $V$  white noise density

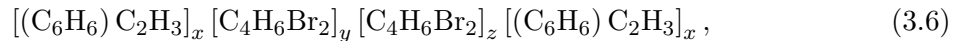
$$S(T) = \frac{d\langle V^2 \rangle}{df} = R^2 \frac{d\langle I^2 \rangle}{df} = 4k_B RT \quad (3.5)$$

of a resistor  $R$  at temperature  $T$  as was first demonstrated by Johnson and Nyquist [Joh28, Nyq28]. In the present noise thermometer, built and improved by [Rei17], the magnetic flux noise spectrum was detected inductively using a superconducting quantum interference device (SQUID).

## 3.2 Polymer Glass FR-122P

### 3.2.1 Chemical Structure

The material whose low-temperature acoustic properties were investigated is a dielectric polymer glass of high molecular weight with the trade name FR-122P. It is distributed by the manufacturer<sup>5</sup> as a white powder. Thanks to its large bromine content of at least 62.5% with respect to mass [Pro16] it is most commonly used as an ingredient for insulating flame retardant applications. From the chemical structure formula



where the first polybutadiene block is a 1,4-isomer and the second one a 1,2-isomer, the atomic bromine concentration can be calculated from the atomic masses  $m_{Br} = 79.9$  u,  $m_C = 12$  u and  $m_H = 1$  u:

$$c_{Br}(\text{FR-122P}) = 11.2\% \quad (3.7)$$

### 3.2.2 Sample Production

In order to obtain a sample from this substance an iteratively modified procedure based on the experience gathered in [Rei05] was developed. First, the powder was pressed into a disc shape of a diameter of 20 mm and a thickness of 2 mm. Then the disc was put between two heading tools preheated to approximately 200 °C and pressed to a thickness of 0.5 mm. Above about 50 °C the material crosses the glass transition temperature. It starts softening and enters a deformable state. Subsequently, the heading tools containing this melt are cooled down quickly by wet wipes. After having reached room temperature the pressure is released and

<sup>3</sup>Sensor DT 470, Lake Shore Cryotronics Inc.

<sup>4</sup>LR-700, Linear Research Inc., 5231 Cushman Place, Suite 21, San Diego, CA 92110-3910, USA

<sup>5</sup>ICL Industrial Products, Kroitzer St. 12, Beer Sheva 84101, Israel

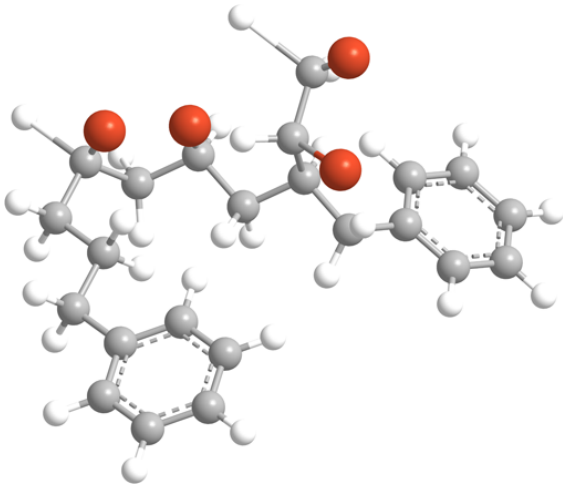


**Figure 3.3:** Solid sphere model of the chemical formula of FR-122P (reconstructed with chemical structure software<sup>a</sup> from [Pro16]). The carbon backbone (grey) forms a polybutadiene block in the middle with polystyrene units on either side. Some of the hydrogen atoms (white) are replaced by bromine atoms (red). The polybutadiene and polystyrene units can be repeated several times so that the overall size of the molecule may be much larger (here:  $x = y = z = 1$ ).

<sup>a</sup>Chem3D, CambridgeSoft, 100 CambridgePark Drive, Cambridge, MA 02140, USA

the sample is taken out. It can then be further processed either to the mechanical oscillators as described in Section 3.3 or to a sample for dielectric measurements as explained in Section 3.4.

There is no direct evidence, e.g. from x-ray diffraction, that the thus obtained samples indeed possessed an amorphous structure. Various facts make it very certain, though, that the samples are at least to the most part amorphous [Ste16]. First, the obtained discs are not stiff and rigid but rather elastic and flexible. Second, the discs are not opaque but rather transparent and clear. Third, upon heating the discs do not start melting at a well defined temperature but rather become more and more soft, the viscosity drops and they exhibit a smooth transition to a liquid state. Finally, measurements of the dielectric function at different frequencies [Aßm17] revealed a relaxation process that is described by an Arrhenius law which is typical of but not exclusive to secondary or  $\beta$ -relaxation in glasses [Kre03, p. 241–251].

### 3.2.3 Material Choice

There are several reasons why this particular substance was chosen for the experiments at hand. First and foremost, thanks to its large bromine concentration of 11 % more than one in ten nuclei carries a nuclear quadrupole moment so the chances to observe an impact of these moments on TLS are quite high. There are two naturally occurring isotopes of bromine,  $^{79}\text{Br}$  and  $^{81}\text{Br}$ , with a nuclear spin of  $I_{\text{Br}} = 3/2$  each. Due to the different numbers of neutrons in the nuclei the resulting nuclear magnetic moments are  $\mu_{^{79}\text{Br}} = (2.110 \pm 0.021)\mu_{\text{n},0}$  and  $\mu_{^{81}\text{Br}} = (2.271 \pm 0.023)\mu_{\text{n},0}$  [Bro47] where  $\mu_{\text{n},0} = e\hbar/(2m_{\text{p}})$  is the nuclear magneton with the proton mass  $m_{\text{p}}$ . The natural abundances of the two isotopes are almost identical with 50.54 % for  $^{79}\text{Br}$  and 49.46 % for  $^{81}\text{Br}$  [Lin76]. The gyromagnetic ratio of bromine can then be calculated to be

$$\gamma_{\text{Br}}^A = \frac{\mu_{\text{Br}}^A}{I\hbar} = \begin{cases} 10.8 \text{ MHz T}^{-1} & A = 79 \\ 11.6 \text{ MHz T}^{-1} & A = 81 \end{cases}. \quad (3.8)$$

The non-spherical charge distribution results in a nuclear quadrupole moment which was measured by atomic beam magnetic resonance [Haa00]

$$Q_{\text{Br}}^A = \begin{cases} (0.305 \pm 0.005) \text{ b} & A = 79 \\ (0.254 \pm 0.006) \text{ b} & A = 81 \end{cases}. \quad (3.9)$$

Other measurements listed in [Sto05] report values ranging from 0.305 b to 0.331 b for  $^{79}\text{Br}$  and from 0.254 b to 0.276 b for  $^{81}\text{Br}$ . The second reason for choosing this substance for the experiments is that all bromine atoms are situated at a carbon bond so to first order the chemical environment and thus the electric field gradient is identical for all quadrupole moments. For a bromine-carbon bond the electric field gradient tensor components can be computed [Bai03] and measured with pure nuclear quadrupole resonance techniques. The quadrupole levels are degenerated, cf. Eq. (2.67), so that  $E_{-m} = E_{+m}$ . Thus, there is only a single quadrupole frequency observable in a bromine nucleus because of its nuclear spin of  $3/2$ , namely from the transition  $\pm 1/2 \leftrightarrow \pm 3/2$ . The measured values for  $^{79}\text{Br}$  range from  $\nu_q = 265$  MHz to 277 MHz depending on the exact stoichiometry of the molecule, for example for 9,10-dibromoanthracene  $\nu_q = (271.59 \pm 0.15)$  MHz [Lud56]. Since the EFG depends only on the atomic site but not on the concerned nucleus it is the same for both  $^{79}\text{Br}$  and  $^{81}\text{Br}$ . Hence, the quadrupole splitting frequency differs by a factor

$$\frac{\nu_{^{79}\text{Br}}}{\nu_{^{81}\text{Br}}} = \frac{Q_{^{79}\text{Br}}}{Q_{^{81}\text{Br}}} = 1.20 \pm 0.03. \quad (3.10)$$

Comparing the nuclear quadrupole splitting with the Zeeman effect an external magnetic field of around 12 T would be required for the  $|m_I = -3/2\rangle$  and the  $|m_I = +1/2\rangle$  levels to cross which is far greater than the Earth magnetic field of around 50  $\mu\text{T}$  or other spuriously present fields in the laboratory environment proving the dominance of the quadrupole splitting. Apart from the physico-chemical reasons an important aspect is the processibility of the material. Unlike for example brominated bisphenol A diglycidether (Br-DGEBA), which also contains bromine nuclei at carbon bonds, FR-122P is suitable for the production of mechanically oscillating specimen. At room temperature Br-DGEBA is a very soft and glue-like substance so that only dielectric susceptibility measurements could be conducted [Aßm18].

### 3.3 Acoustic Measurements

#### 3.3.1 Double Paddle Oscillator

**Acoustic Resonators** For high-frequency acoustic experiments ultrasound transducers, that is piezoelectric elements, are used to probe the sample [Hun72, Jäc72]. The resonance frequencies of a resonance cavity are of the order of  $f \sim v/l$  where  $v$  is the speed of sound in the material and  $l$  is a characteristic length of the cavity. With  $v \sim 10^3 \text{ m s}^{-1}$  and  $l \sim 1 \text{ cm}$  a typical lower limit of the frequency is thus  $f \sim 100 \text{ kHz}$ . On the other hand for low-frequency measurements in the (sub-)kHz-range macroscopic mechanical resonators are suited [Ray84]. A possible realisation of such a resonator is the vibrating reed design [Bar74], cf. left side of Fig. 3.4. Here, driven oscillations of a reed, made of the sample to be investigated and clamped on one side, are read out. Other implementations such as vibrating wires or tuning forks [Pob07, p. 382–384], used mainly in liquid helium experiments, are possible but less common for glass studies.

In this thesis the mechanical resonator was realised as a double paddle oscillator (DPO). It was first proposed by [Kle85] as a torsional oscillator with a high quality factor for the study of superfluid helium, quantum-crystals or liquid-crystal films. It consists of a thin rod with two pairs of opposing masses, a lighter one at the top and a heavier one in the middle of the rod. The main advantages of the DPO design over that of the vibrating reed or wire are the beneficial strain distribution and the fact that the leg acts as an acoustic low-pass filter. In

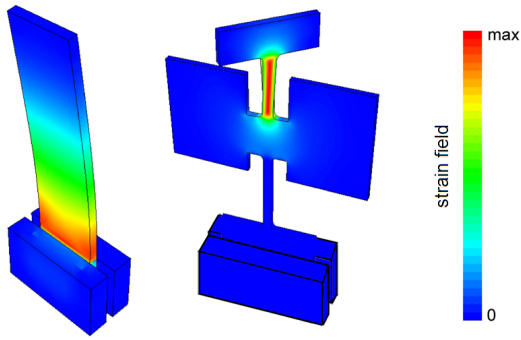


**Figure 3.4:** Strain field distribution in the first order bending mode of a vibrating reed (left) compared to the torsional mode inside a DPO (right). In case of the vibrating reed set-up the strain is at maximum near the clamping for all modes. For the DPO modes exist for which the strain near the clamping is neglectable (adapted from [Hei02]).

the torsional modes the strain is concentrated inside the bulk and therefore away from the clamping, as can be seen on the right side of Fig. 3.4. This leads to very little unwanted additional loss contribution in these modes. Another advantage of the DPO design is its rich mode spectrum where besides the torsional modes also bending and flapping modes are available, each in several orders. This allows for broad frequency interval coverage with a single oscillator. A beneficial aspect of using a mechanical resonator is the fact that the resonator also constitutes its own frequency filter whose selectivity is governed by the linewidths of the resonances. Hence, unlike for dielectric measurements, no additional low-pass filtering is necessary since spurious high-frequency (HF) signal components which might couple into the set-up are not able to excite oscillations. Thus, stray HF signals do not show any effect unless they are large enough to result in dissipative eddy currents which might cause a slight temperature increase.

**Production** After the FR-122P powder had been cast into a solid disc the surface was covered with a thin metallic film. This served two purposes. For once to enhance the thermal connection to the sample holder and thus the cryostat and additionally, to electrically excite and detect the DPO oscillations as explained in Section 3.3.2. For this purpose gold was chosen because of its good thermal conductivity. The gold layer was produced using in-situ sputter deposition by an ultra high vacuum (UHV) sputtering machine<sup>6</sup>. Several trials were necessary to tune the sputtering parameters such that neither the sample dissolved during the sputtering process because of the deposited heat nor the gold layer could easily be taken off by adhesive tape, which would mean that there was not sufficient contact between sample and gold. A good result could be achieved with the following protocol. The disc was thermally connected to a sample holder by vacuum grease<sup>7</sup> and then inserted into the sputtering machine. First, the surface was cleaned for 10 s using the ion source in order to remove spurious water. Then, a niobium layer of < 10 nm was sputtered as an adhesion layer. Finally, an 800 nm thick gold layer was sputtered on top of the niobium in steps of 200 nm with breaks of 15 min in between to avoid too large a temperature increase of the sample.

The subsequent production step involved cutting out the DPO shape with an automated programmable milling machine<sup>8</sup> using a milling head with a diameter of 300  $\mu\text{m}$  rotating at a frequency of 29 000 rpm and advancing at a speed of 50  $\text{mm min}^{-1}$ . The dimensions of the DPO are given in Fig. 3.5. Due to the precision of the milling machine the actually obtained size might deviate from the sketch by less than 10  $\mu\text{m}$ . At four places a bridge of about

<sup>6</sup>S450 UHV Sputtering System, DCA Instruments Oy, Vajossuonkatu 8, 20360 Turku, Finland

<sup>7</sup>Baysilone paste, GE Bayer Silicones, 5 Cranfield Road, Loslock, Devon, BL6 4QD, UK

<sup>8</sup>Sorotec CL403, Sorotec GmbH, Withig 12, 77836 Rheinmünster, Germany

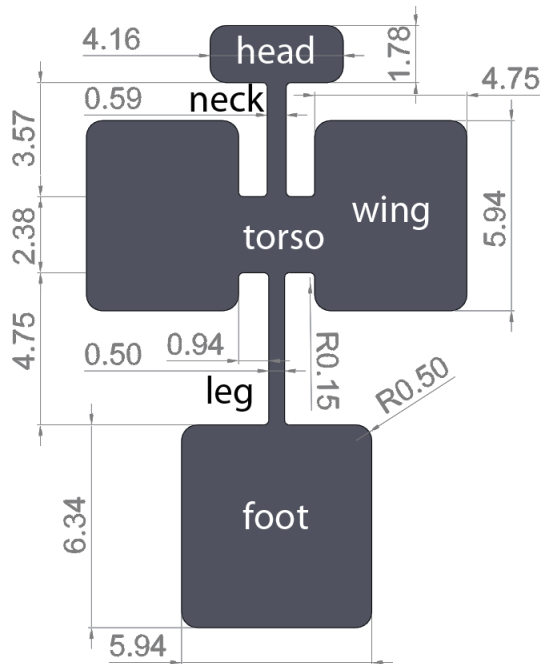


**Figure 3.5:** Dimensions of the DPO in mm. The thickness of the DPO orthogonal to the drawing plane amounts to 0.5 mm.

150  $\mu\text{m}$  was left out which holds the DPO in place making it less fragile when transported. A picture of the DPO at this point of the fabrication process can be found in the appendix in Fig. B.6. The bridges were cautiously removed with a scalpel before inserting the DPO onto the sample holder. In the past different cutting techniques such as anisotropic wet chemical etching (in case of metallic samples) [Kle85] or laser cutting (in case of vitreous silica) [Cla00] were employed for the production of DPO. For this polymeric sample milling constituted a simple and robust way to cut out the DPO with satisfactory quality. As shown in Fig. 3.6 milling resulted in small spalling defects of the gold layer on a scale below 50  $\mu\text{m}$  which is less than 10% of the smallest structure, the leg of the paddle, and thus continuous thermal contact is guaranteed.

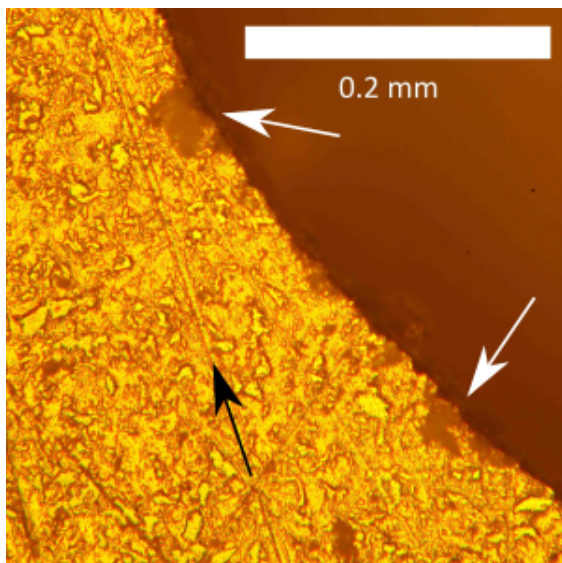


**Figure 3.6:** Quality of an edge and of the gold layer of the DPO after milling as viewed under a top light microscope. One observes spalling defects (white arrows) and surface scratches (black arrow), which do not penetrate the entire gold layer, though.

When the DPO was covered with a gold layer only on one side bending of the DPO towards the sputtered side was observed which resulted in a displacement of the DPO head of about

1 mm from its original position. This was highly problematic given the gap size between DPO and sample holder of 40  $\mu\text{m}$  since like that the paddle would touch the sample holder, cf. Section 3.3.2. During the sputtering process the sample heated up, exceeded the glass transition temperature and softened. When the sample cooled down afterwards now with the deposited gold layer on one side and became fully solid again, mechanical strain between sample and gold layer built up. It was released when the DPO was milled out along the weakest structure, i.e. the leg and neck, defining the direction of the bending. Therefore, a DPO was produced with a sputtered gold layer of the same thickness on either side to counterbalance the strain. This one indeed showed less bending, however, it was not sufficient for the use in the experiment yet. As only one side could be sputtered at a time there still remained an asymmetry between the two sides. What resolved this issue was a post-processing step after milling. Placing the DPO on a metallic block which had been heated to a temperature at which the material started to soften and exerting constant high pressure on the DPO helped the amorphous sample to relax to a configuration with less internal strain and thus less bending.

**Thermal Coupling** At low temperatures radiation losses are negligible because of  $P_{\text{rad}} \propto T^4$  and convection does not occur in vacuum. Thermal conduction is therefore the only way for the sample to reach thermal equilibrium with the experimental platform whose temperature gives feedback to the heating unit. The sample is coupled to the experimental platform only via the thin DPO leg. This constitutes a group of thermal resistances that are arranged in series. The total thermal resistance consists of the thermal transport resistance through the sample and the gold film, and the thermal boundary resistance between different materials.

With a residual resistivity ratio (RRR) of around 2 for sputtered gold [Kar04] and a room temperature resistivity of  $\rho_{\text{Au},0} = 2.44 \times 10^{-8} \Omega \text{m}$  [Mat79] the thermal conductivity of gold at  $T = 10 \text{ mK}$  is given by the Wiedemann-Franz law:

$$\kappa_{\text{Au}} = \frac{\text{RRR}L}{\rho_{\text{Au},0}}T = 20 \text{ mW K}^{-1} \text{ m}^{-1} \quad (3.11)$$

where  $L = 2.44 \text{ W } \Omega \text{ K}^{-2}$  is the Lorenz number. The low-temperature thermal conductivity of amorphous polystyrene

$$\kappa_{\text{ps}} \sim \kappa(T_0) \left( \frac{T}{T_0} \right)^2 = 1 \mu\text{W K}^{-1} \text{ m}^{-1}, \quad (3.12)$$

is estimated with  $\kappa(1 \text{ K}) = 10 \text{ mW K}^{-1} \text{ m}^{-1}$  [Ree66] and the known quadratic temperature scaling of amorphous materials. As a compromise between the requirements of thermal coupling and not too much mechanical influence a gold layer thickness of 800 nm, that is 0.16 % of the paddle thickness, was chosen, which improves the thermal conductivity of the DPO at 10 mK by a factor 32 according to Eq. (3.11) and (3.12).

The second part of the thermal resistance series is the thermal boundary resistance or *Kapitza resistance*. It is caused by a mismatch of the acoustic impedance between two materials 1 and 2 resulting in backscattering of heat carrying phonons. It is given by

$$R_{\text{K}} = \frac{15\hbar^3 \rho_1 v_1^3}{2\pi^2 k_{\text{B}}^4 \rho_2 v_2} \frac{1}{T^3}. \quad (3.13)$$

Here,  $\rho_i$  and  $v_i$  are the mass density and speed of sound of material  $i$ , respectively. From the Kapitza resistance between copper and vacuum grease  $R_{K,Cu-vg}T^3 = 6.7 \text{ cm}^2\text{K}^4/\text{W}$  [And70] and with  $\rho_{Cu} = 8.96 \text{ g cm}^{-3}$ ,  $\rho_{Au} = 19.3 \text{ g cm}^{-3}$ ,  $v_{Cu} = 3300 \text{ m s}^{-1}$  and  $v_{Au} = 1990 \text{ m s}^{-1}$  [Swa89] the Kapitza resistance between gold and vacuum grease at  $T = 10 \text{ mK}$  can be computed to be  $R_{K,Au-vg} = 516 \text{ m}^2 \text{ K W}^{-1}$ . This serves as an order-of-magnitude estimate of the corresponding value between gold and FR-122P, also an organic compound as the grease.

The weakest point for thermalisation of the DPO is the thin leg which connects the DPO torso with the clamped foot. With a cross section of  $A_{leg} = 0.25 \text{ mm}^2$  and a length of  $l_{leg} = 5 \text{ mm}$  the total thermal conductance  $G$  amounts to

$$G_{tot} = \kappa_{ps} \frac{A_{leg}}{l_{leg}} + \kappa_{Au} \frac{A_{Au}}{l_{leg}} \approx 2 \text{ nW K}^{-1}. \quad (3.14)$$

The total surface area of the DPO  $A_{DPO} = 1.1 \text{ cm}^2$  yields a Kapitza conductance of

$$G_K = A_{DPO}/R_K \approx 200 \text{ nW K}^{-1}. \quad (3.15)$$

Hence, the Kapitza resistance is negligible compared to the weak thermal link of the DPO leg.

**Eigenmodes** Unlike in the case of a vibrating reed whose eigenmodes can be determined analytically this is not possible for the geometry of a DPO and one has to rely on numerical calculations. In this thesis these were carried out using a finite-element method (FEM) algorithm implemented in the software package SolidWorks<sup>9</sup>. In Fig. 3.7 a synopsis of the most important eigenmodes is presented. The bending modes B1 through B3 are also present in the vibrating reed while the other ones are not. Waving modes cannot be excited nor detected by the employed experimental set-up since for these modes the distance between DPO and electrodes does not change so no charge is moved and consequently no signal acquired as explained in Section 3.3.2. In particular the torsional modes ST and AT are well suited for measuring the mechanical susceptibility because of their beneficial strain distribution unaffected by the clamping.

The resonance frequencies of the DPO eigenmodes are listed in Table 3.2. The antisymmetric torsion mode could not be found experimentally. For the torsional modes there is a phase difference in the signal between the excitation and the detection side of  $\pi$  in contrast to most other modes. That means whenever one side approaches the electrode the opposing side moves away. This feature allows to experimentally better distinguish the torsional modes from the other ones. The resonance frequencies from simulations and measurements do not agree perfectly. This is probably because the exact mechanical parameters such as the elastic modulus  $E$  and the Poisson ratio  $\nu_P = -\partial e_{tr}/\partial e_{ax}$ , a measure of transverse strain when compressed axially, are not known for FR-122P and therefore the corresponding values for polystyrene,  $E = 2.1 \text{ GPa}$  and  $\nu_P = 0.387$  [Sys14], were used in the simulations. From this we can calculate the shear modulus

$$G = \frac{E}{2(1 + \nu_P)} = 0.757 \text{ GPa}. \quad (3.16)$$

The mass density of the sample was calculated by dividing the mass of the disc  $m_{disc} = (0.5268 \pm 0.0001) \text{ g}$  by its cylindrical volume  $V = \pi(d/2)^2 h$  where the diameter  $d =$

<sup>9</sup>Dassault Systmes, 10 rue Marcel Dassault, CS 40501, 78946 Vlizy-Villacoublay Cedex, France

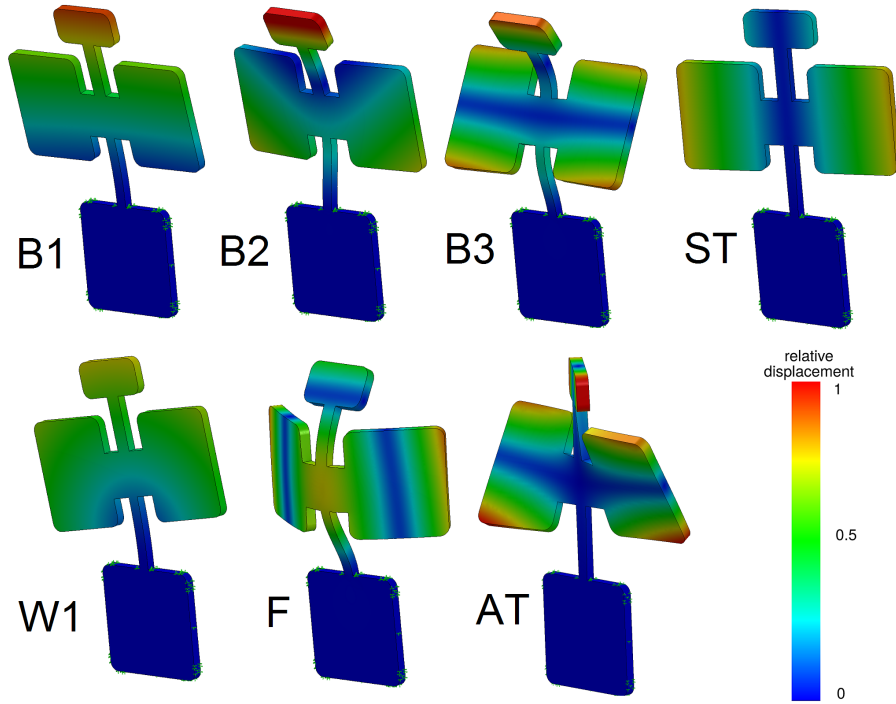


**Figure 3.7:** Seven lowest eigenmodes of the DPO (from left to right). Top: bending mode (Bx) 1, 2, 3, symmetric torsion mode (ST). Bottom: waving mode (Wx) 1, flapping mode (F), antisymmetric torsion mode (AT). The false colours encode the amplified relative displacement to the unperturbed situation.

$(29.7 \pm 0.3)$  mm and the height  $h = (0.41 \pm 0.02)$  mm were measured at different positions of the disc. The density of the sample then amounts to  $\rho_s = (1.8 \pm 0.1)$  g cm<sup>-3</sup>. Another reason for the deviation is the impact of the gold film. According to [Whi95] for the torsional modes the resonance frequency changes by

$$\frac{\Delta f_0}{f_0} = \frac{d_{\text{Au}}}{2d_s} \left( \frac{3G_{\text{Au}}}{G_s} - \frac{\rho_{\text{Au}}}{\rho_s} \right) = 0.08 \quad (3.17)$$

where the indices Au and s refer to the gold film or the sample, respectively, and  $d$  denotes the thickness. The parameters of the gold film are  $E_{\text{Au}} = 78$  GPa,  $\nu_{\text{P,Au}} = 0.42$  and  $\rho_{\text{Au}} = 19$  g cm<sup>-3</sup> [Sys14]. This results in a constant shift that does not affect the relative frequency change, which is the actual quantity of interest. The internal friction is also altered by

$$\Delta Q^{-1} = \frac{3d_{\text{Au}}}{d_s} \frac{G_{\text{Au}}}{G_s} Q_{\text{Au}}^{-1} \approx 0.17 Q_{\text{Au}}^{-1}. \quad (3.18)$$

Hence, one might have to account for an additional constant loss contribution which depends on the absolute internal friction of a hypothetical gold DPO of 800 nm thickness.

### 3.3.2 Measurement Strategy

**Experimental Set-Up** The aim of acoustic measurements is to determine the elastic susceptibility, defined in Eq. (2.32) and (2.33), by measuring its real part, connected to the relative change in speed of sound  $\frac{\delta v}{v}$ , and its imaginary part, connected to the internal fric-

mode	rel. phase	$f_0$ [Hz] (sim.)	$f_0$ [Hz] (exp. at 297 K)	deviation [%]
B1	0	286	225	21
W1	—	287	not measurable	—
ST	$\pi$	393	306	22
B2	0	1 531	1 350	12
B3	0	3 016	2 686	11
F	0	4 200	4 660	11
AT	$\pi$	4 626	not found	—

**Table 3.2:** The resonance frequencies  $f_0$  of the relevant DPO eigenmodes as determined by FEM calculations (third column), by experiment (fourth column) and the relative deviation (last column) are sorted with respect to frequency. The second column lists the phase difference between the excitation and the detection side of the DPO.

tion  $Q^{-1}$ , separately. To this end a mechanical resonator, in this thesis a double paddle oscillator (DPO), described in Section 3.3.1, is driven around its resonance frequency  $f_0$  at varying temperatures. The change of the resonance curve, that is its spectral position and width, is analysed in order to study the temperature dependence of the susceptibility. A sketch of the experimental set-up, which was developed and built by [Hem08] is shown in Fig. 3.8. The resonator is fixed to the sample holder by a leaf spring that is itself clamped by a copper block and two brass screws.

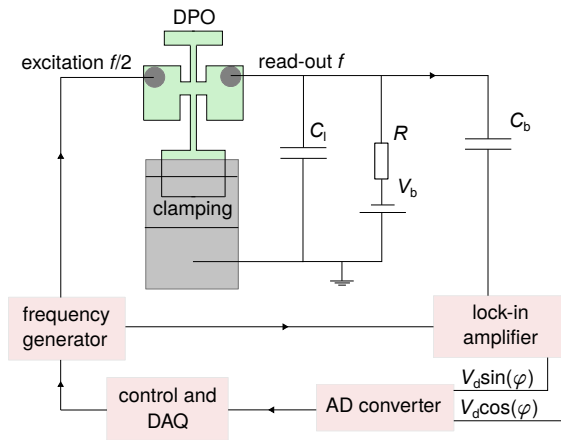


**Figure 3.8:** Measuring set-up for acoustic experiments. The DPO is driven electrically with an electrode on one side at frequency  $f/2$ . It oscillates at  $f$  and is read out capacitively on the other side. A lock-in amplifier measures both the in-phase signal  $V_d \cos(\varphi)$  and the out-of-phase signal  $V_d \sin(\varphi)$  of the oscillation amplitude  $V_d$ . Both components are digitised and saved to a computer by data acquisition software (DAQ).

**Excitation** Below the upper outer corners of both wings of the DPO round electrodes with an area of  $A_{el} \approx 2.5 \text{ mm}^2$  are located. They are connected to a frequency generator on the excitation side and to a bias voltage on the detection side. A distance of  $40 \mu\text{m}$  between the platform where the foot of the DPO is fixed and the plane of the electrodes makes sure that the DPO can oscillate freely. The frequency generator periodically changes the voltage of the excitation electrode  $V_{ex} = V_0 \cos(\omega t/2)$ . The electrode and the wing of the DPO, being separated by a distance  $x$ , constitute a plate capacitor with capacitance

$$C_{ex} = \frac{\varepsilon_0 A}{x} \approx 1 \text{ pF} \quad (3.19)$$

if operated in an evacuated chamber with the vacuum permittivity  $\epsilon_0$ . The resulting electric force

$$F(t) = \frac{1}{2} C_{\text{ex}} \frac{V_{\text{ex}}^2(t)}{x} = \frac{1}{4} \frac{V_0^2}{x} (1 + \cos(\omega t)) \quad (3.20)$$

leads to an attraction of the DPO and the electrode. This drives the oscillations at twice the excitation frequency since the DPO is attracted twice per cycle, once with a positive and the second time with a negative charge.

**Detection** On the read-out side the capacitor formed by DPO and electrode changes its capacitance  $C_d$  according to the paddle oscillations. For sufficiently low driving voltages  $V_0$  and consequently small deflections  $|\xi| \ll x$ , defined to be positive for deflections to the electrode, the capacitance change can be Taylor expanded to first order yielding

$$C_d(t) = C_{d,0} \frac{1}{1 - \frac{\xi}{x}} \approx C_{d,0} \left( 1 + \frac{\xi}{x} \right). \quad (3.21)$$

Applying a bias voltage  $V_b = 300 \text{ V}$  parallel to the detection electrode generates an AC current accounting for the change of charge at the electrode which causes a voltage drop  $V_d(t)$  at the series resistor  $R = 400 \text{ M}\Omega$ . A capacitor  $C_b$  separates the DC bias voltage from the lock-in amplifier. Accounting for stray capacitances  $C_1 \sim 100 \text{ pF}$  of the wiring, the detected AC voltage is given by [Ber75]

$$\begin{aligned} V_d(t) &= V_b \frac{\xi(t)}{x} \frac{C_{d,0}}{C_{d,0} + C_1} \frac{\omega R (C_{d,0} + C_1)}{1 + (\omega R (C_{d,0} + C_1))^2} \\ &\stackrel{\omega \gg RC_1, C_{d,0}}{\approx} V_b \frac{\xi(t)}{x} \frac{C_{d,0}}{C_{d,0} + C_1} \\ &\stackrel{C_1 \gg C_{d,0}}{\approx} V_b \frac{\xi(t)}{x^2} \frac{\epsilon_0 A}{C_1} \end{aligned} \quad (3.22)$$

The values given above explain the approximation  $\omega \sim 1000 \text{ s}^{-1} \gg 4 \times 10^{-4} \text{ s}^{-1} \sim RC_1$  for the involved measuring frequencies. The scale of typical detection voltages is  $10 \text{ }\mu\text{V}$  to  $100 \text{ }\mu\text{V}$  which translates to deflections of around  $1 \text{ \AA}$  to  $10 \text{ \AA}$  justifying the assumption in Eq. (3.21).

**Driven Harmonic Oscillator** For small deflections  $|\xi| \ll d_{\text{DPO}}$ , where  $d_{\text{DPO}}$  is the length scale of the DPO, it can be treated as a damped harmonic oscillator with a restoring force  $F_{\text{re}} \propto -\xi$  performing driven oscillations described by the inhomogeneous ordinary linear differential equation

$$\ddot{\xi}(t) + \omega_0 Q^{-1} \dot{\xi}(t) + \omega_0^2 \xi(t) = \frac{F(t)}{m} \quad (3.23)$$

where  $m$  is the oscillating mass of the paddle. The damping factor

$$Q^{-1} = \frac{\Delta E}{2\pi E} \quad (3.24)$$

is defined as the energy loss  $\Delta E$  per cycle divided by the energy  $E = 1/2 \omega_0^2 m \tilde{\xi}^2$  stored in the oscillation where  $\tilde{\xi}$  is the oscillation amplitude. The force  $F(t) = F_0 + \tilde{F}(t)$  is given by Eq. (3.20) and can be decomposed in a constant part  $F_0 = V_0^2/(4x)$  and a periodically varying part  $\tilde{F}(t) = V_0^2/(4x) \cos(\omega t) := m \hat{F} \cos(\omega t)$ . In reality the force will not strictly follow the sinusoidal dependence because  $x \rightarrow x + \xi(t)$  but in the small deflection approximation

$\xi \sim 1 \text{ \AA} \ll 40 \mu\text{m} = x$  this helps to derive analytic results for the oscillations. Inserting the ansatz  $\xi(t) = A \exp(-i\omega t)$  into Eq.(3.23) and solving for the complex amplitude  $A$  one obtains solutions for the real or in-phase part  $\Re(A) = A \cos(\varphi)$  and the imaginary or out-of-phase part  $\Im(A) = A \sin(\varphi)$  (details e.g in [Dem06]) which are given by

$$A \cos(\varphi) = \frac{\hat{F}}{4\pi^2} \frac{Q^2 (f_0^2 - f^2)}{(f_0^2 - f^2)^2 Q^2 + f_0^2 f^2} \quad (3.25)$$

and

$$A \sin(\varphi) = -\frac{\hat{F}}{4\pi^2} \frac{Q f_0 f}{(f_0^2 - f^2)^2 Q^2 + f_0^2 f^2}. \quad (3.26)$$

The phase difference  $\varphi$  between excitation and detection can be computed from its definition in the complex plane,

$$\varphi = \arctan\left(\frac{\Im(A)}{\Re(A)}\right) = -\arctan\left(\frac{f_0 f}{Q (f_0^2 - f^2)}\right), \quad (3.27)$$

and so can the magnitude of the oscillation amplitude

$$|A| = \sqrt{(\Re(A))^2 + (\Im(A))^2} = \frac{\hat{F}}{4\pi^2} \frac{Q}{\sqrt{(f_0^2 - f^2)^2 Q^2 + f_0^2 f^2}} \propto \mathcal{L}(f; f_0, Q). \quad (3.28)$$

The resonance curve has the shape of a Lorentzian function  $\mathcal{L}$  centred around the resonance frequency of the damped oscillator

$$f_{\text{res}} = f_0 \sqrt{1 - \frac{1}{2}Q^{-2}} \quad (3.29)$$

where  $f_0 = \omega_0/(2\pi)$  is the resonance frequency in the undamped case. For high quality factors  $Q \sim 1500$  to  $4000$  as in the case of this work the difference between the damped and undamped case can be neglected.

**Determining the Relative Change of the Speed of Sound** The analytical expressions for both the amplitude and the phase are fitted to a measured resonance curve of the DPO, as shown in Fig. 3.9. At resonance,  $f = f_0$ , the phase equals  $-\pi/2$  and the amplitude is maximum as expected. From these fits  $f_0$  and  $Q$  are obtained and can be used to compute the quantities of interest. The phase offset  $\varphi_0$  is due to imbalanced signal transit times and additional phase uptakes between excitation and detection side. For the temperature dependent measurements it was manually adjusted for by setting a phase difference at the lock-in amplifier. For any wave of wavelength  $\lambda$  inside a medium with speed of sound  $v$  the relation  $f\lambda = v$  holds. The eigenmode wavelengths of the DPO  $\lambda \sim d_{\text{DPO}}$  are of the order of the geometric dimensions of the paddle. If thermal expansion is ignored, which is legitimate for small temperature changes of 1 K at maximum, then  $d_{\text{DPO}} = \text{const}$  and thus  $f \propto v$ . The relative change in speed of sound can then be calculated from the relative change of the resonance frequency

$$\frac{\delta f_0}{f_0} = \frac{\delta v}{v} \quad (3.30)$$

where  $f_0$  ( $v$ ) is the resonance frequency (speed of sound) at some arbitrary reference temperature and  $\delta f_0$  ( $\delta v$ ) the difference to the reference value. Considering the fact that the eigenmodes of the DPO are based on shear motion instead of compression the speed of sound branch which is probed with this method is the transverse one rather than the longitudinal one.

**Determining the Internal Friction** The internal friction is the inverse of the quality factor as the symbol  $Q^{-1}$  already suggests. This is equivalent to a calculation from the resonance linewidth  $\Delta f$  and the resonance frequency:

$$Q^{-1} = \frac{\Delta f}{f_0}. \quad (3.31)$$

The linewidth is defined as the full width at half maximum (FWHM) of the resonance curve, that is the frequency interval in which the power of the oscillation is greater than half of the power at resonance. In Fig. 3.9 voltages are plotted. With  $P \propto V^2$  the FWHM therefore lies at  $1/\sqrt{2}$  of the peak amplitude after the underground is subtracted. If only the relative change of the internal friction is of interest the change of the amplitude can be recorded. Together with the absolute value of the resonance frequency it follows from curve analysis of Eq. (3.28) that

$$Q^{-1} \propto \frac{1}{f_0^2 A}. \quad (3.32)$$

This allows for continuous measurements without the need of acquiring an entire resonance curve. Another possibility is to measure the characteristic time constant  $\tau$  of the exponentially decaying amplitude  $A(t) = A_0 \exp(-t/\tau)$  if the external drive is suddenly switched off at  $t = 0$  [Sie98]. The internal friction can then be calculated absolutely as

$$Q^{-1} = \frac{1}{\pi \tau f_0}. \quad (3.33)$$

**Data Acquisition** The experiment as well as the cryostat were controlled by different LabVIEW<sup>10</sup> algorithms. Two different and in parts complementary measuring strategies, scanning an entire resonance curve and logging the resonance frequency, were pursued.

**Scanning a Resonance Curve** For the first method the frequency generator<sup>11</sup> sampled the resonance peak at a step size of about  $1/50 Q^{-1} f_0$  and within an interval of around  $5 Q^{-1} f_0$ . The lock-in amplifier<sup>12</sup> working in the 2- $f$  mode received the current frequency and measured both the in-phase and out-of-phase voltages. These signals were digitised with an analogue-to-digital converter<sup>13</sup> (ADC) and transformed to the amplitude and phase variables according to Eq. (3.28) and (3.27) which were then stored along with the frequency in a file on the measuring computer.

<sup>10</sup>LabVIEW 2014, National Instruments Corp., 11500 N Mopac Expy, Austin, TX 78759, USA

<sup>11</sup>PM5191, Philips, Amstelplein 2, 1096 BC Amsterdam, Netherlands

<sup>12</sup>Dynatrac 393, DL INSTRUMENTS (formerly Ithaco), 646 76 Rd, Brooktondale, NY 14817, USA

<sup>13</sup>MEphisto Scope 1, Meilhaus Electronic GmbH, Am Sonnenlicht 2, 82239 Alling, Germany

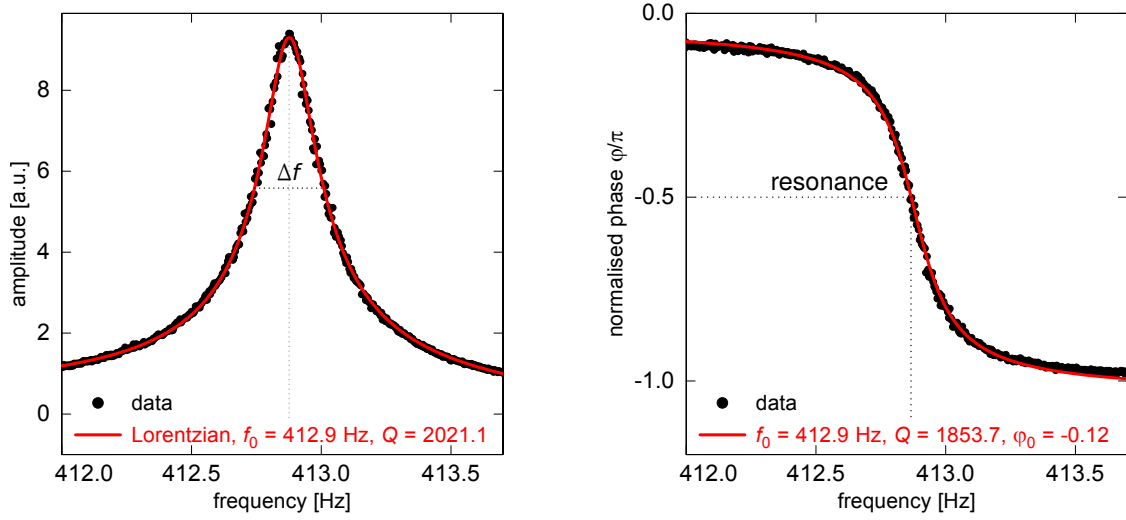


**Figure 3.9:** Resonance curve of the symmetric torsion mode at  $T = 10$  mK using an excitation voltage of  $V_0 = 2$  V. The oscillation amplitude (left) following a Lorentzian line shape and the phase  $\varphi$  between drive and response (right) are plotted as a function of twice the driving frequency  $f/2$ . While the resonance frequencies obtained from both fits agree well there is a difference in the quality factor. This may be because the phase does not change by  $-\pi$  over the course of the resonance, a behaviour that was not understood.

**Logging the Resonance Frequency** For the second approach a proportional (P) control of the resonance frequency was implemented which did not require the acquisition of an entire resonance curve but rather only the recording of the amplitude at resonance. Whenever the resonance frequency changed, for instance due to temperature variations, the phase difference between the current phase and  $-\pi/2$  was evaluated. The larger this deviation by the more was the measuring frequency adjusted until the DPO was at resonance again to within a phase uncertainty of  $\Delta\varphi = 0.005$ . From the slope of the phase course around  $f_0$  this translated to a systematic frequency error of maximum

$$\frac{\Delta f_0}{f_0} \sim \left( \frac{\partial \varphi}{\partial f} \right)^{-1} \Bigg|_{f=f_0} \frac{\Delta \varphi}{f_0} = \frac{\Delta \varphi}{2Q} \sim 1 \times 10^{-6}. \quad (3.34)$$

**Measuring Protocol** LabVIEW data acquisition software was developed and validated using an already existing bronze DPO, which had been mounted in the nitrogen bath cryostat. Once the software was ready and it could communicate with all employed measuring instruments via a general purpose interface bus (GPIB)<sup>14</sup> proof-of-concept experiments with the newly fabricated DPO made from FR-122P followed in the nitrogen bath cryostat.

Upon successful testing of the experimental set-up it was transferred to the  $^3\text{He}/^4\text{He}$  dilution cryostat for the low-temperature measurements. Before the temperature was varied at first the impact of the experimental parameters such as the bias voltage  $V_b$  and the excitation voltage  $V_0$  were investigated at  $T = 12$  mK. This helped to choose appropriate values for each eigenmode of the DPO aiming for as high a signal-to-noise ratio (SNR) as possible without driving the oscillator non-linearly. Next, thermalisation measurements were conducted

<sup>14</sup>GPIB-USB-HS, National Instruments Corp.

in order to determine an approximate time scale  $t_{\text{th}}$  after which the results did not change significantly any more. Then, for all detectable eigenmodes of the DPO resonance curves were recorded along exponential temperature ramps in steps of 10% starting at 10 mK. At each temperature step first, a certain time  $t > t_{\text{th}}$  passed while the resonance frequency was continuously logged. Then, a complete resonance curve was recorded within a refined frequency interval updated by the latest result for the resonance frequency of the logging algorithm.

### 3.3.3 Probing the Nuclear Bath

**Quadrupole Transition Driving Module** Combined acoustic and electromagnetic experiments on the borosilicate glass BK-7 proved that one could manipulate the outcome of the acoustic experiment by changing the intensity of the electromagnetic field [Lae77]. With this idea in mind and in order to learn more about the role of nuclear quadrupole moments in the low-frequency properties of amorphous systems a novel experimental module was designed. The aim was to drive the nuclear quadrupole transition with an appropriate RF bias frequency and thereby to equally populate the two hyperfine levels. Simultaneously low-frequency acoustic susceptibility measurements were made. Intensity induced saturation of TLS as in [Lae77], thermal and other effects have to be excluded by measuring at varying bias frequencies and bias powers. Then, differences between measuring series with and without quadrupole transition drive can be attributed to altered interaction processes, e.g. relaxation phenomena, between TLS and NQM.

The module can be attached to the existing DPO sample holder by two brass screws. As shown in Fig. 3.10 it consists of two u-shaped oxygen-free high-conductivity (OFHC) copper cramps which clamp a wire loop. The wire has a diameter of 1.6 mm and is made from a niobium-titanium (NbTi) alloy which becomes superconducting at 9 K [Kus17]. An SMA adapter connects this wire to one of the signal lines through which an RF bias signal can be transmitted. At the other end the last two centimetres of the outer conductor of the semi-rigid coaxial NbTi-wire were removed. The inner conductor of diameter 0.4 mm was bent to form a loop which was spot-welded to the outer conductor. The total resistance between inner and outer conductor amounts to  $20 \Omega$ . The module can be assembled independently and then be fixed as a whole to the sample holder. It is inserted in place of the module for inductive DPO read-out, developed in [Hem15]. Estimating a lower bound of the mechanical resonance frequencies of the loop yields

$$f_{0,m} \sim \frac{v_a}{\lambda} = \frac{v_a}{2l} \approx 200 \text{ kHz} \quad (3.35)$$

with the speed of sound of the NbTi-alloy  $v_a \approx 0.5(v_{\text{Ni}} + v_{\text{Ti}}) = 3.81 \text{ km s}^{-1}$  [Sam68] and a length scale of the loop  $l \approx 1 \text{ cm}$ . This exceeds all measuring frequencies in this thesis by almost two orders of magnitude so that no disturbing interplay is expected.

**Module Characterisation** When operated at low temperatures an obvious performance criterion is that the RF signal must not deposit too much energy in channels other than the nuclear spin bath which would lead to undesired heating of the sample. A new DPO had to be fabricated with only one side of the paddle, opposite to the bias coil, coated with a gold layer in order to reduce heating due to eddy currents. As this DPO again exhibited bending a thin copper foil was put between the DPO foot and the sample holder in order to ensure free oscillations. To investigate the power distribution around the DPO electromagnetic field

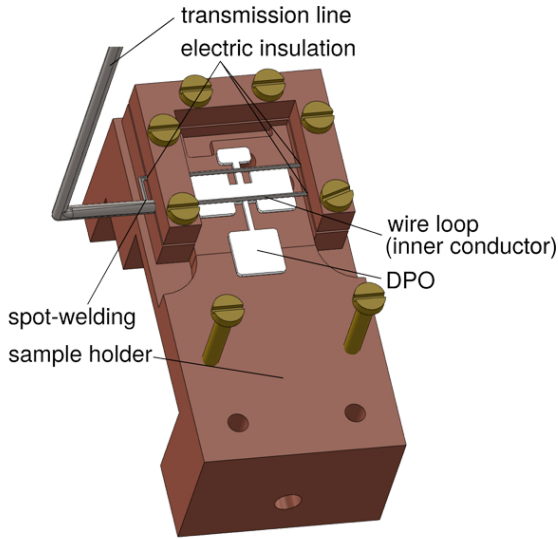


**Figure 3.10:** The novel experimental module mounted onto the sample holder. The wire loop above the DPO emits an RF electromagnetic field which can be tuned to match the nuclear quadrupole splitting frequency. The inner conductor, which forms the wire loop, is electrically insulated from the sample holder by adhesive polyimide tape<sup>a</sup>.

<sup>a</sup>Kapton tape, DuPont, 1007 Market Street, Wilmington, DE 19898, USA

simulations were carried out using the software package Sonnet<sup>15</sup>. In the simulation the geometry of the superconducting loop above and a gold layer below the DPO was reproduced. The resulting power dissipation in the gold layer for a bias frequency  $f_b = 272$  MHz, close to the expected nuclear quadrupole splitting, is depicted in Fig. 3.11. It confirms that the AC field generated by the loop does penetrate the parts of the DPO which are also subject to the AC strain caused by the eigenmode oscillations, in particular the torso and the lower neck. The goal is to provide an electromagnetic field which is strong enough to saturate the quadrupole transition. This would change the interaction between the NQM and the TLS and thus also the corresponding relaxation rate. As a result a deviation from the elastic susceptibility measurements in the unsaturated case would be expected. The total power dissipation integrated over the entire gold layer area is  $P_{t,\text{sim}} = 329$  nW at an input voltage of 1 V at the port. This power is dissipated in form of eddy currents in the resistive gold layer since gold does not become superconducting for any known temperature. Given the thermal conductance of the DPO leg of  $G = 2$  nW K<sup>-1</sup>, cf. Eq. (3.14), this would lead to a massive temperature rise. Considering the power scaling  $P \propto V^2$  one can estimate the input voltage for a tolerable temperature increase of  $\Delta T = 1$  mK to be

$$V \sim \sqrt{\frac{G\Delta T}{P_{t,\text{sim}}}} 1 \text{ V} = 3 \text{ mV}. \quad (3.36)$$

Besides the heating aspect another important condition for successful nuclear quadrupole spectroscopy with this module is the spectral profile of the loop. Response simulations of the loop up to 600 MHz computed the reflection parameter with respect to voltage of the design to be around  $S_{11} \approx -5 \times 10^{-4}$  dB in this frequency range with a broad minimum of  $-1.5 \times 10^{-3}$  dB at 50 MHz. Although such a low value of  $S_{11}$  means that only  $1 - 10^{2S_{11}/10} = 1.2 \times 10^{-4}$  of the input power is emitted by the loop the frequency profile is predicted to be rather flat in the interesting frequency interval from 200 MHz to 300 MHz. However, room-temperature characterisation measurements using a network analyser<sup>16</sup> in transmission mode between the loop and one electrode of the DPO sample holder (and between the two electrodes)

<sup>15</sup>Sonnet Software Inc., 100 Elwood Davis Road, North Syracuse, NY 13212, USA

<sup>16</sup>8752C Network Analyzer, Hewlett Packard Inc., 1501 Page Mill Road, Palo Alto, CA 94304, USA

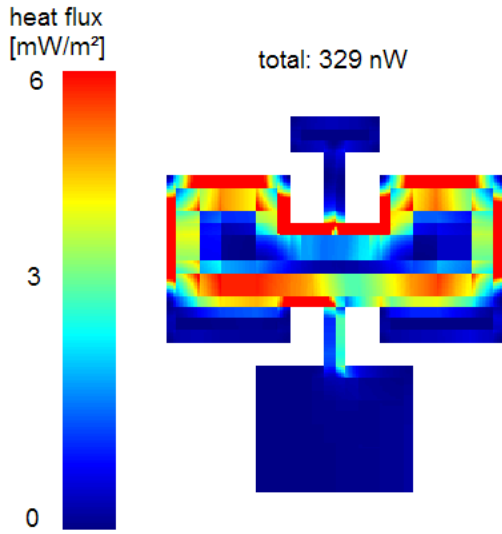


**Figure 3.11:** Power distribution in the gold layer of the DPO at a bias frequency of  $f_b = 272$  MHz and a peak-to-peak voltage at the port of  $V_{pp} = 1$  V.

show a peak at 200 MHz, which can be described by a Lorentzian function as shown in Fig. 3.12. This feature can be reproduced in the simulations if a gold layer on both sides of the DPO is assumed which suggests that this feature is of electrical nature, e.g. a parasitic resonance in the wiring or on the gold surface of the paddle. If for the inductance of the DPO gold layer a value of  $L_{DPO} = 10$  nH is assumed and for the capacitance  $C_{DPO} = \epsilon_0 A_{DPO}/d \sim 10$  pF between DPO and the sample holder an electrical resonance frequency of around  $f_{0,el} = 1/(2\pi\sqrt{L_{DPO}C_{DPO}}) \sim 500$  MHz is expected.

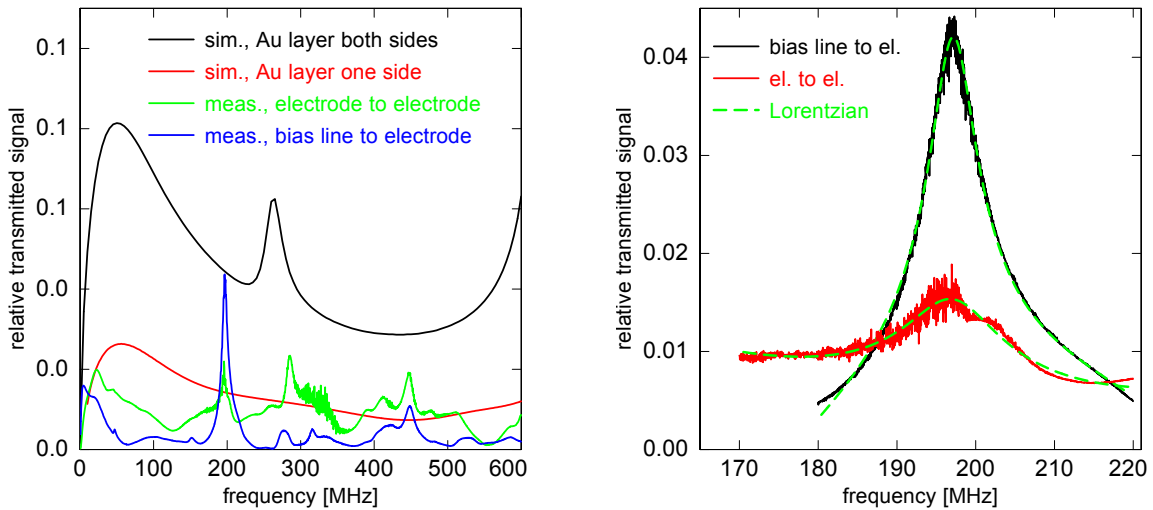


**Figure 3.12:** Measured and simulated transmission spectrum of the wire loop and the sample holder electrodes (left). The peak around 200 MHz can be described by a Lorentzian function (right).

**Measuring Protocol** First, the RF bias field was varied with a MHz frequency generator<sup>17</sup> up to 600 MHz at different constant bias powers while the resonance frequency, the amplitude

<sup>17</sup>8648A Signal Generator, Hewlett Packard Inc.

of the paddle oscillations and the temperature of the cryostat were recorded. To this end the ST mode of the DPO was excited leading to a paddle oscillation frequency of 260 Hz. In order to rule out parasitic coupling of the bias power into the carbon resistance thermometer, which would lead to a wrongly indicated temperature increase, a noise thermometer was installed on the experimental platform as well. With that a second, independent temperature reading was established. In a second measuring series the bias power was varied from -100 dBm to -30 dBm while the bias frequency was set to 270 MHz, the literature value of the quadrupole splitting of one of the bromine isotopes. Again, temperature, resonance frequency and amplitude were measured. Both measurements were automated with the help of LabVIEW programmes.

### 3.4 Dielectric Measurements

**Experimental Set-Up** Measurements of the low-frequency dielectric susceptibility were conducted using a capacitance bridge<sup>18</sup> that is shown schematically in Fig. 3.13. The disc-shaped sample, cf. Section 3.2.2, was put between an upper (H) and a lower (L) copper electrode which forms a circular plate capacitor. Vacuum grease on both sides of the disc was used for a better thermal connection to the electrodes. The electrodes were coupled thermally to and simultaneously isolated electrically from the top and bottom plate by two sapphire layers. By varying tap 1 and tap 2 the voltage over each leg was set. Adjusting the reference impedance  $Z_0 = R_0 + i\omega C_0$  so that the detector voltage was balanced, the unknown impedance could be measured. From its imaginary part  $\Im(Z_s) = -1/(\omega C_s)$  the sample capacitance  $C_s = \varepsilon' \varepsilon_0 A/d$  was calculated. Relative changes of the real part of the dielectric function are equal to relative changes of the capacitance:

$$\frac{\delta\varepsilon'}{\varepsilon'} = \frac{\delta C}{C}. \quad (3.37)$$

The ratio of the ohmic, dissipative current  $I_r = V/R$  to the magnitude of the displacement current through the capacitor  $I_c = V/Z_c = V\omega C$  defines the loss tangent

$$\tan(\delta) = \frac{I_r}{I_c} = \frac{1}{\omega RC}. \quad (3.38)$$

The loss tangent is thus a measure of the signal absorption inside the sample. The sample impedance is calculated from an equivalent circuit of a resistor parallel to a capacitor,

$$i\omega\varepsilon' C_0 - \omega\varepsilon'' C_0 = \frac{1}{Z_s} = \frac{1}{R} + i\omega C, \quad (3.39)$$

where  $C_0$  is the capacitance of the bare set-up, i.e. with the sample replaced by vacuum. Equating the real part of Eq. (3.39) on both sides one finds a way to calculate the imaginary part of the dielectric function from the measurable quantities:

$$\left| \frac{\varepsilon''}{\varepsilon'} \right| = \frac{1}{\omega R \varepsilon' C_0} = \frac{1}{\omega RC} = \tan(\delta). \quad (3.40)$$

**Correction for Stray Capacitances** Although the sample disc has the same diameter as the electrodes, the AC electric field could still bypass the sample at the sides leading to a

<sup>18</sup>AH2700, Andeen Hagerling, 31200 Bainbridge Road, Cleveland, OH 44139-2231, USA

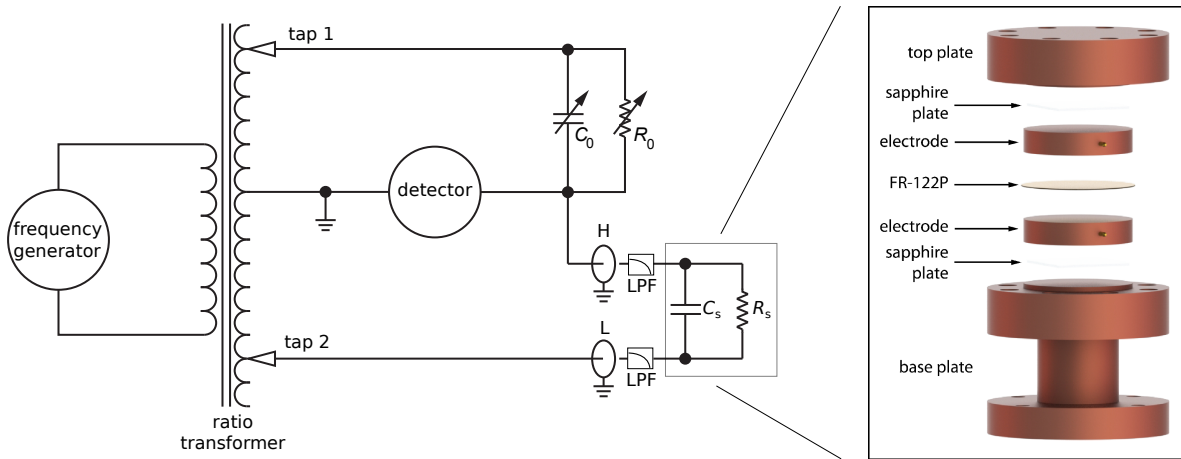


**Figure 3.13:** Circuit diagram of the capacitance bridge (left) used for dielectric measurements (adapted from [AH04]). The measured sample is represented by a capacitance  $C_s$  and resistance  $R_s$ . It is put in a stack between electrodes and sapphire plates (right). The base plate is attached to the experimental stage of the cryostat (adapted from [Sch17]).

stray capacitance  $C_p$ . To obtain the sample capacitance  $C_s$  the measured capacitance  $C_m$  has to be corrected. The stray capacitance due to the inhomogeneous field outside the sample is parallel to the plate capacitor so that  $C_s = C_m - C_p$ . The stray capacitance is assumed to be temperature independent so that  $\delta C_m = \delta C_s$ . Hence, the relative change in the real part must be corrected by

$$\frac{\delta \varepsilon'}{\varepsilon'} = \frac{\delta C_s}{C_s} = \frac{\delta C_m}{C_m} \frac{C_m}{C_m - C_p} := \frac{\delta C_m}{C_m} f^{-1} \quad (3.41)$$

where the filling factor  $f = 1 - C_p/C_m$  was introduced. The same holds for the loss tangent:

$$\frac{\varepsilon''}{\varepsilon'} = \frac{1}{\omega R C_s} = \frac{1}{\omega R C_m} f^{-1} = \tan(\delta_m) f^{-1}. \quad (3.42)$$

For the employed set-up the parasitic capacitance was determined to be 2.1 pF [Sch17] which yields, considering the sample capacitance of  $C_s = 18.3$  pF, a filling factor of  $f = 0.89$ .

**Insertion of Low-Pass Filters** In acoustic measurements the resonator is simultaneously a frequency selective filter thanks to its eigenmode spectrum. In contrast, low-frequency dielectric measurements are sensitive to spurious high-frequency components which might couple into the electronics and alter the sample's frequency response as was analysed in [Däh10]. For this reason low-pass filters (LPF) were inserted at the high and low gate of the capacitance bridge. The LPF consisted of a resistor and an inductor, which were in series to the signal line, and a capacitor in parallel to the signal line. The cut-off frequency of these filters was around 1 MHz.

The disadvantage of using LPF is the fact that due to their intrinsic resistance, inductance and capacitance they form an additional  $RLC$ -component which rotates the signal in the complex plane by some angle  $\delta_{\text{LPF}}$ . If the part of the measured loss tangent coming from the filter is assumed to be constant with temperature and to be approximately determinable from

knowing the largest and smallest loss tangent of the measurement,

$$\delta_{\text{LPF}} = \frac{\min(\tan(\delta_m))}{\max(\tan(\delta_m))} \arctan(\min(\tan(\delta_m))), \quad (3.43)$$

then the results can be corrected by transforming capacitance and loss tangent to a complex conductance,  $\tilde{C} = \tilde{C}' + i\tilde{C}'' = C_m(1 + i \tan(\delta_m))$ , rotating  $\tilde{C}$  by  $-\delta_{\text{LPF}}$  in the complex plane,  $\tilde{C}_r = \mathcal{R}(-\delta_{\text{LPF}})\tilde{C}$ , and then retransforming to the common variables,  $C_s = \tilde{C}'$  and  $\tan(\delta_s) = \tilde{C}''/\tilde{C}'$ .

**Measuring Protocol** For three different frequencies, 60 Hz, 1 kHz and 16 kHz covering the accessible frequency range of the capacitance bridge, capacitance and loss were measured from 7.5 mK to 500 mK at an excitation voltage of  $V_{\text{exc}} = 100$  mV. The data were acquired continuously by a LabVIEW programme with 20 subsequent readings being averaged to one data point. After around 4 h the temperature was increased by 10 % to the next temperature step.

## 4. Results and Analysis

In the following chapter the measured data are presented and analysed. At first, in Section 4.1 the results of characterisation measurements of the experimental set-up are shown including an estimation of the noise level and an appropriate choice of measuring parameters such as the excitation voltage and the thermalisation time. Afterwards, in Section 4.2 the elastic and dielectric susceptibilities of FR-122P at low temperatures between 10 mK and 600 mK are displayed and analysed in detail. These measured data are then compared to theoretical models with the help of numerical simulations in Section 4.3. Starting with the STM itself two extensions are examined more closely, a resonant interaction between NQM and TLS and an additional relaxation process that is driven by NQM. Finally, in Section 4.4 the insights gained from different experiments with the quadrupole transition drive module, such as frequency sweeps and power sweeps, are laid out.

### 4.1 Preparatory Measurements

#### 4.1.1 High Temperatures

After identifying the true resonance frequencies of the DPO the symmetric torsion mode and the first bending mode were used for validation measurements of the software and the set-up at high temperatures. The resonance frequency decreases linearly at a rate of

$$\frac{\partial f_0}{\partial T} = \begin{cases} (-267 \pm 1) \text{ mHz K}^{-1} & \text{for ST} \\ (-202 \pm 1) \text{ mHz K}^{-1} & \text{for B1} \end{cases} \quad (4.1)$$

as shown in Fig. 4.1 which translates to a relative decrease of

$$\Delta f_0 / (f_0 \Delta T) = (7.84 \pm 0.03) \times 10^{-4} \text{ K}^{-1} \quad (4.2)$$

for both frequencies. If the main reason for this behaviour was the temperature dependence of the density and the eigenmode wavelength then the frequency would be expected to change as

$$\frac{\sqrt{\frac{G}{\rho}}}{\lambda} \propto \frac{\sqrt{V}}{l} \sim \sqrt{l} \approx \sqrt{l_0} \left( 1 + \frac{1}{2} \alpha T \right) \quad (4.3)$$

where  $\alpha = 6.59 \times 10^{-4} \text{ K}^{-1}$  [Shi16] is the thermal expansion coefficient of polystyrene and  $l$  is the characteristic length scale of the DPO. Although the absolute values of the coefficients are of the same order of magnitude the sign is wrong. Hence, thermal expansion is not responsible for this behaviour by itself. This means that the shear modulus  $G$ , the only remaining quantity, governs the temperature dependence. As the temperature is lowered, the material gets stiffer and the speed of sound and consequently the resonance frequency increases. Note that for higher temperatures  $T \gtrsim 270 \text{ K}$  the derivative of the resonance frequency with respect to temperature gets more negative. This provides further support for the fact that the sample has an amorphous structure since at the glass transition there is a drop in the elastic and thus by Eq. (3.16) also in the shear modulus [Akl81]. The same value of the slope was used for the solid line fitting both frequencies on the left side of Fig. 4.1 demonstrating that the change

in the shear modulus does not depend on frequency on this scale. During the measurement discontinuities in the resonance frequency occurred in the order of one to two percent whose origin might be sudden release of mechanical stress in the material. Since only the change of the frequency was of interest these discontinuities could be corrected for by adding a constant to the concerned data.

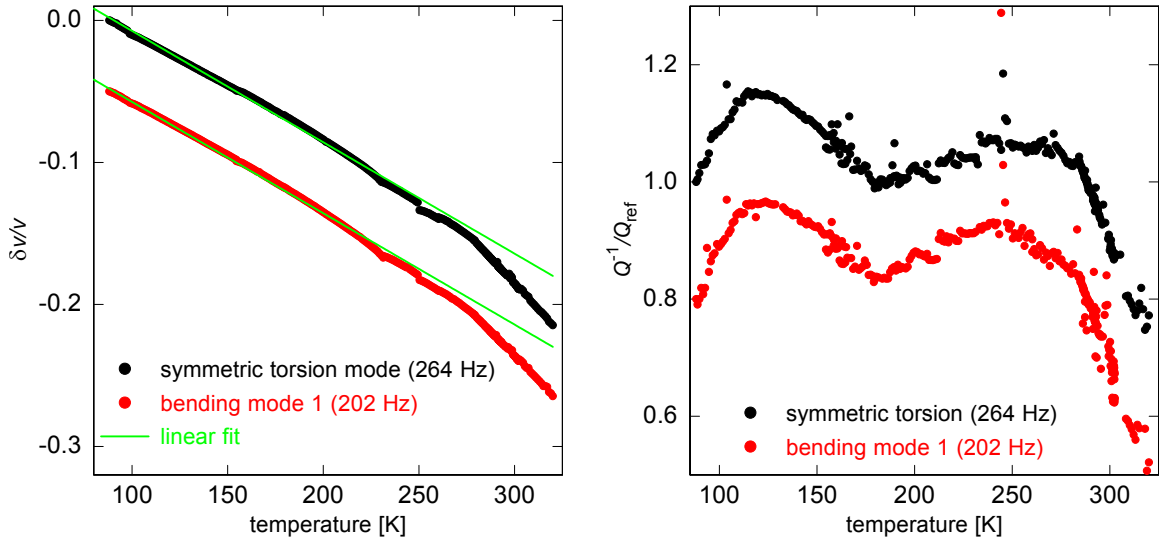


**Figure 4.1:** Validation measurement data from 80 K to 320 K. At such high temperatures the speed of sound decreases linearly with increasing temperature (left). The internal friction data (right) were normalised to an arbitrary reference and the two curves shifted relative to each other for better comparison. The resonance frequencies of the modes refer to room temperature. The data were acquired at a resolution of  $\Delta T = 1$  K using the resonance frequency logging method without averaging and a waiting time of 5 min between subsequent temperature steps.

The high-temperature internal friction data exhibit two broad maxima at around 120 K and 250 K, respectively, with a rather steep decrease for  $T \gtrsim 270$  K. This feature corresponds to the onset of the glass transition confirming the observation in the speed of sound. The maximum at 250 K was also found in dielectric absorption measurements [Aßm17] and can be attributed to a beta-relaxation process present in amorphous polymers involving motion of the polymeric backbone [Smi07]. The position of the maximum is given by the condition  $\omega\tau_{\beta} = 1$  where the relaxation time

$$\tau_{\beta} \propto \exp\left(-\frac{E_a}{k_B T}\right) \quad (4.4)$$

is described by an Arrhenius equation. The shift of the maximum with frequency

$$\Delta T = T_1 T_2 \frac{k_B}{E_a} \ln\left(\frac{\omega_1}{\omega_2}\right) = 3 \text{ K} \quad (4.5)$$

is not discernible for these frequencies given an activation energy of  $E_a = 0.52$  eV [Aßm17].

### 4.1.2 Background

Acoustic measurements are very sensitive to vibrations or other mechanical disturbances due to the small displacements that need to be resolved. Hence, it is of vital importance to mechanically decouple the experiment from the environment. One means is using a pressured air cushion upon which the cryostat is floating. While this helps to suppress the vibrations caused by the pumps or from neighbouring laboratories there are also internal vibration sources, e.g. refilling the dewar with liquid helium. Since this cannot be compensated for the only chance is to pause the measurement during the filling process and for some time afterwards as well which has been done for all experiments. As explained in Section 3.1.1 there is a capillary controlling the inflow rate into the 1 K pot. As Fig. 4.2 demonstrates whenever the 1 K pot is closed the SNR is enhanced by a factor two to three. Especially right after opening the 1 K pot, that is when the valve is moving, the data scatter a lot. For this reason the data acquisition software stopped the measuring process while the 1 K pot was being filled. The valve is closed when the 1 K pot is full and does not open again until the helium level falls below 20 %.

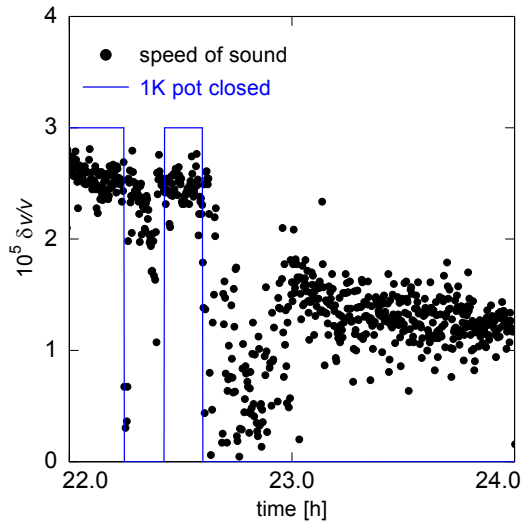


**Figure 4.2:** Impact of opening or closing the 1 K pot. During the time when the 1 K pot is closed (solid line elevated) the data scatter much less than while the 1 K pot is open (solid line at zero). The temperature changed from 41 mK to 46 mK at  $t = 23$  h which is the reason for the two different signal levels. The data in this plot were not averaged in order to reveal the noise of the data.

Despite all these precautions there still remains a certain noise level in the experimental set-up without any excitation voltage applied. This background noise was measured to be Gaussian distributed with a mean value of  $V_n = 0.2 \mu\text{V}$  on one and  $V_n = 0.5 \mu\text{V}$  on the other channel of the lock-in amplifier and a standard deviation of  $\sigma_n = 0.3 \mu\text{V}$ , cf. Fig. B.9. This sets the ultimate lower boundary of the excitation voltage  $V_0$  which was adjusted for each mode such that the resulting SNR at the resonance frequency was between 10 dB and 20 dB. The noise spectrum of the experimental set-up featuring a  $1/f$ - and a white noise component is plotted in Fig. 4.3. This observation made it necessary to account for the noise background in the fitting routines of the resonance curves. Since the noise spectrum fit does not match the data perfectly the  $1/f$ -noise and the white noise are not the only constituents. Therefore, the local noise floor around a resonance peak was Taylor expanded to second order. The Lorentzian fit function was thus extended by a quadratic polynomial

$$\mathcal{L}(f; f_0, Q) \rightarrow \mathcal{L}(f; f_0, Q) + a_0 + a_1 f + a_2 f^2. \quad (4.6)$$

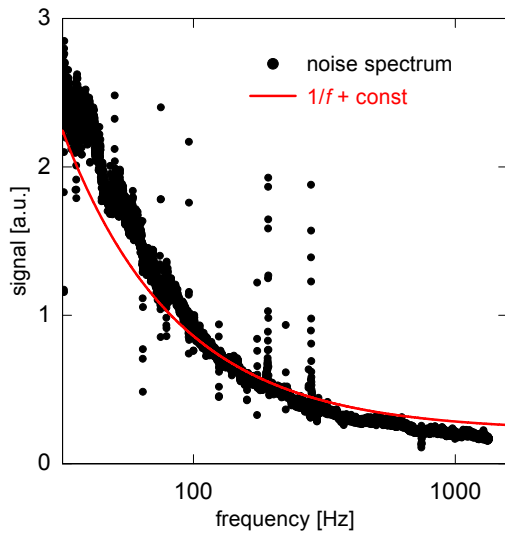


**Figure 4.3:** The noise spectrum of the acoustic experimental set-up (black data points) can be approximately described by  $1/f$ -noise and a constant term (solid line).

### 4.1.3 Voltage Scaling

**Excitation Voltage** In order to determine appropriate measuring parameters the impact of the excitation voltage amplitude  $V_0$  and the bias voltage  $V_b$  were investigated. To this end resonance curves were recorded at varying excitation and bias voltages and fitted with a Lorentzian function. The variance of the fit parameters was used to calculate the error bars. From Fig. 4.4 one can learn that for too low excitation voltages  $V_0 \lesssim 1$  V not only is the uncertainty very large but also do the resonance frequency and the internal friction deviate systematically from the corresponding values at intermediate excitation strengths. Comparing the scale of the frequency scattering at the intermediate voltage plateau,  $\Delta(\delta f_0/f_0) < 10^{-5}$ , to the scale of the low-temperature relative change in speed of sound,  $10^{-4}$ , cf. Section 4.2, the former can be regarded as sufficiently constant. The internal friction exhibits a systematic downward drift with continuously shrinking errors although it would be expected to be constant. A possible explanation might be the impact of the background. As can be inferred from Fig. B.8 in the appendix for very low excitation voltages the background is comparable in magnitude to the resonance peak itself leading to non-symmetric resonance peaks for which the fitting procedure yields too low resonance frequencies.

The resonance peak amplitude rises quadratically with excitation voltage as demonstrated in Fig. 4.5. This behaviour is expected since  $V_d \propto \xi \propto F \propto V_0^2$ , cf. Eq. (3.20) and (3.22). Another observation from Fig. 4.5 is that the error decreases with increasing  $V_0$  because the SNR improves. If the excitation voltage is increased too much, e.g. to 7 V for the case of the ST mode, the resonator does no longer oscillate harmonically and the small displacement approximations from Section 3.3.2 are not valid anymore. Hence, the data cannot be analysed by Lorentzian line shapes. This in itself would be less of a problem since other, asymmetric line shapes exist such as Fano or Duffing resonances. However, what really matters is the strain amplitude  $e$  the TLS experience. If the displacement  $\xi$ , and thus the strain, gets too large then non-linear effects occur [Sto95] and might conceal other phenomena. A strain value for which non-linear effects are not expected is  $e \sim 10^{-7}$ , e.g. [Ray84]. A crude estimation of the strain in our case yields

$$e \sim \frac{\xi}{l_{\text{DPO}}} = \frac{V_d x^2 C_1}{V_b \epsilon_0 A_{\text{el}} l_{\text{DPO}}} \lesssim 3 \times 10^{-7} \quad (4.7)$$

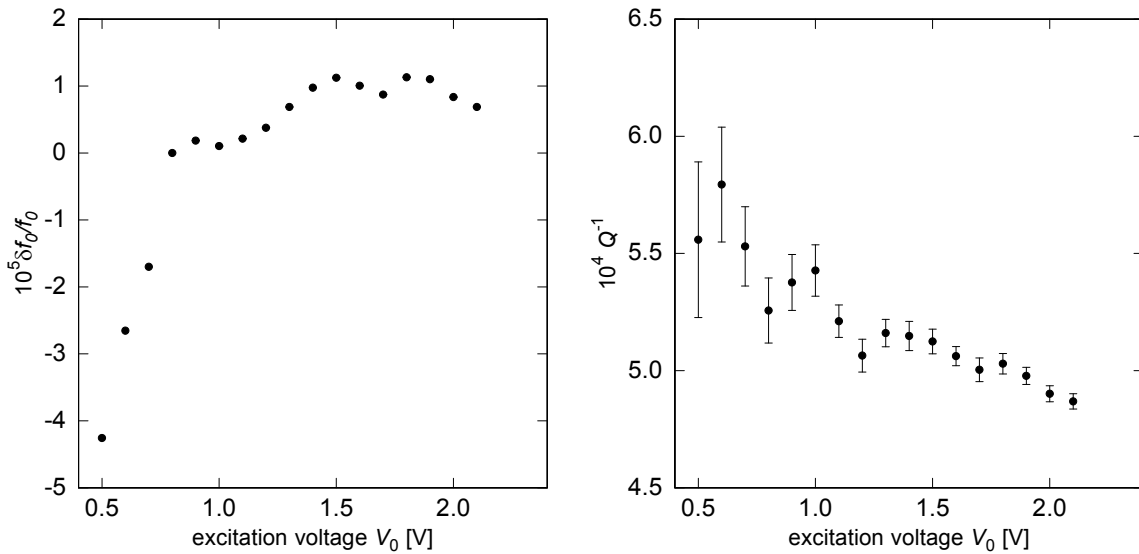


**Figure 4.4:** Excitation voltage dependence of the resonance frequency (left) and the internal friction (right) in case of the ST mode at 15 mK using a bias voltage of  $V_b = 300$  V. At each excitation voltage the resonance curve was fitted by a Lorentzian. The error bars of the resonance frequency are disguised by the data points.

for typical detection voltages  $V_d(V_0 = 2 \text{ V}) < 100 \mu\text{V}$ . As a compromise between a reasonably high SNR and avoiding non-linear driving  $V_0 = 2 \text{ V}$  was therefore chosen as the excitation voltage for the ST mode. The other modes required higher excitation voltages from 7 V (for B2) up to 25 V (for F) in order to separate the resonance peak from the background. At equal excitation voltage the amplitudes differed by a factor of about 500 as can be seen in Fig. B.7. Despite the rather high voltages and in contrast to the ST mode those modes did not show any sign of non-linearities; they rather became the more symmetric the larger their amplitude, cf. B.8. As only the detected voltage  $V_d$  depends on  $V_0$  but neither the equilibrium distance  $x$  nor the other parameters also a higher  $V_0$  does not cause problems as long as  $V_d$  is accordable with linear driving. Within this boundary condition the excitation voltages for the individual modes were chosen so that the SNR was of the same order as for the ST mode.

**Bias Voltage** According to Eq. (3.22) the measured voltage should scale linearly with the bias voltage  $V_b$  which is confirmed by Fig. 4.6. From the slope  $s = (12.5 \pm 0.4) \text{ mV V}^{-1}$  the displacement amplitude can be calculated to be

$$\xi = sx^2 \frac{C_1}{\epsilon_0 A_{el}} = 9 \times 10^{-11} \text{ m} \quad (4.8)$$

confirming the above estimations and argumentation. As for the impact of the bias voltage on the resonance frequency one would expect a decrease of  $f_0$  with rising  $V_b$ . That is because the effective spring constant  $k_{\text{eff}}$ , which takes into account the intrinsic spring constant of the DPO and the attractive electrostatic force between electrodes and the gold layer, decreases and  $f_0 \propto \sqrt{k_{\text{eff}}}$  [Hem15, p. 80]. This behaviour is qualitatively reproduced in the measurements, see Fig. B.10 in the appendix. The internal friction is not influenced for any finite value of  $V_b$ . For the sake of achieving a large SNR a high bias voltage  $V_b = 300$  V was therefore used for all further experiments.

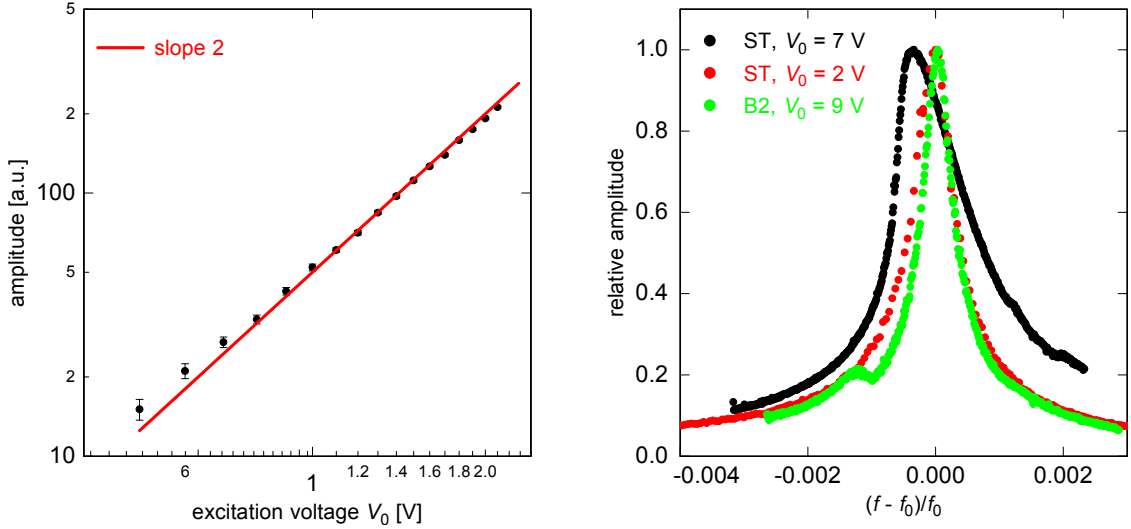


**Figure 4.5:** Excitation voltage dependence of the signal amplitude of the ST mode at 15 mK using a bias voltage of  $V_b = 300$  V (left). Non-linear driving sets in at different voltages for different eigenmodes (right).

#### 4.1.4 Thermalisation

With all the voltage parameters set the only remaining measuring parameter is the waiting time between subsequent temperature steps. In order to obtain reliable results the sample must be in thermal equilibrium with the cryostat. As glasses have a rather large and towards low temperatures only slowly decreasing specific heat, cf. Fig. 2.1, they release more heat for a given temperature decrease. The heat release is hindered by the poor thermal coupling through the leg of the DPO, though, which explains why one has to carefully consider thermalisation effects. In Fig. 4.7 the temporal signal evolution is plotted for two temperature steps between 13 mK and 52 mK. Even after 6 h there is still a drift in the signal observable. Restricting oneself to TLS only the heat release in a sample of volume  $V$  can be calculated from the STM [Esq98, p. 18] as

$$\dot{Q} = \frac{\pi^2 k_B^2}{24} p_0 V (T_f^2 - T_i^2) \frac{1}{t} \exp\left(-\frac{t}{\tau_{\max}}\right) \quad (4.9)$$

if the sample is to be heated up or cooled down from  $T_i$  to  $T_f$ . Integrating Eq. (4.9) for  $t \ll \tau_{\max}$  yields for the sample temperature

$$\Delta T(t) = \frac{Q}{c_V} = \frac{\pi^2 k_B^2}{24 c_V} p_0 V (T_f^2 - T_i^2) \log\left(\frac{t}{t_i}\right). \quad (4.10)$$

Using the parameter from the logarithmic fit from Fig. 4.7 and a specific heat for polystyrene of  $c_V(13 \text{ mK}) \sim 0.5 \mu\text{J K}^{-1}$  [War61] a TLS density of

$$p_0 \approx 7 \times 10^{21} \text{ cm}^{-3} \text{ eV}^{-1} \quad (4.11)$$

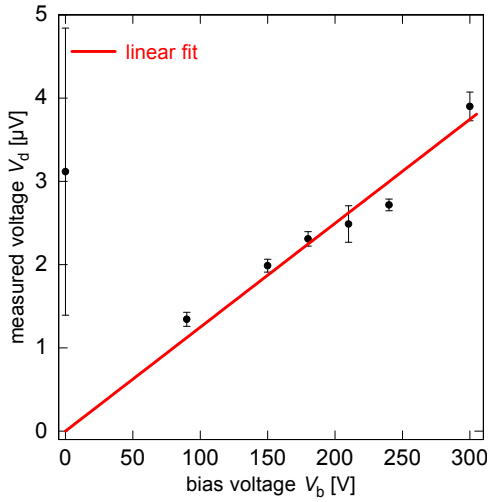


**Figure 4.6:** Bias voltage dependence of the ST mode signal amplitude at 81 K (data were taken in the nitrogen bath cryostat). The data follow the expected scaling of  $A \propto V_b$ .

can be inferred. This is smaller by about a factor of 1 000 than the value found in vitreous silica with specific heat measurements [Las75]. In contrast to polystyrene this sample has a nuclear spin bath due to the bromine atoms which also constitutes a thermal reservoir. The true value for the specific heat is thus larger and so is the TLS density.

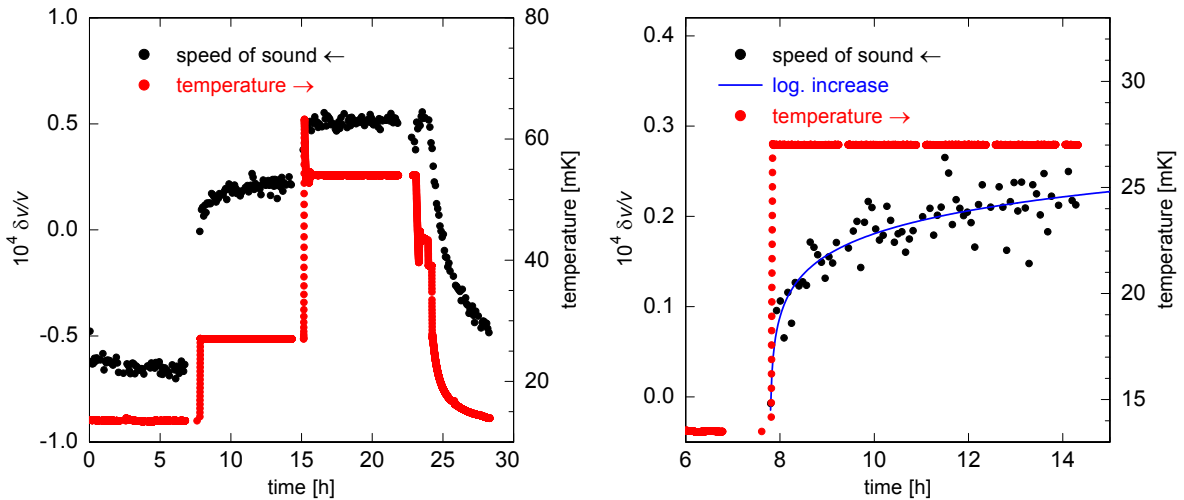


**Figure 4.7:** Thermalisation measurements of the sample from 13 mK to 26 mK, 26 mK to 52 mK and subsequent cooling (left). 50 readings were averaged to form one data point. Magnifying the first temperature step (right) one sees that the relative change of the speed of sound increases logarithmically.

After the second temperature step the signal follows almost instantaneously the temperature rise without any long-term drift. Thus, for temperatures above 50 mK already a short thermalisation time of 30 min is adequate whereas for lower temperatures longer times are required. No exponential suppression of the first signal rise in Fig. 4.7 is detectable. Therefore, the logarithmic increase of the relative change of the speed of sound will not saturate as long as  $t \ll \tau_{\max}$  with  $\tau_{\max} \gg 6$  h. For this reason the lowest-temperature thermalisation time was chosen such that within the hour following the end of the measurement the mean signal would

change by less than the (averaged) data scatter. This resulted in a thermalisation time of 2 h for the measurements at  $T < 50$  mK.

## 4.2 Complex Acoustic and Dielectric Susceptibilities

### 4.2.1 Temperature Overview

The temperature dependence of the relative change in speed of sound over more than four orders of magnitude in temperature can be viewed in Fig. 4.8, exemplary for 180 Hz. The other modes show a similar behaviour. It first rises until about 1 K and then flattens off on a semi-logarithmic scale. The increase at high temperatures is due to mechanical stiffening of the material, as discussed in Section 4.1.1. At low temperatures the TLS become the dominant degree of freedom but their influence can only be seen on a smaller scale of  $10^{-5}$  to  $10^{-4}$ . As for the internal friction besides the two maxima at higher temperatures, which are already known from Fig. 4.1, one observes a decline towards a plateau extending from 50 mK to 5000 mK. This plateau region is also found in conductivity measurements of a variety of other glasses, too, and was coined the nearly constant loss (NCL) regime [Lee91]. Towards even lower temperatures the internal friction decreases again which can be just about adumbrated in this semi-logarithmic plot.

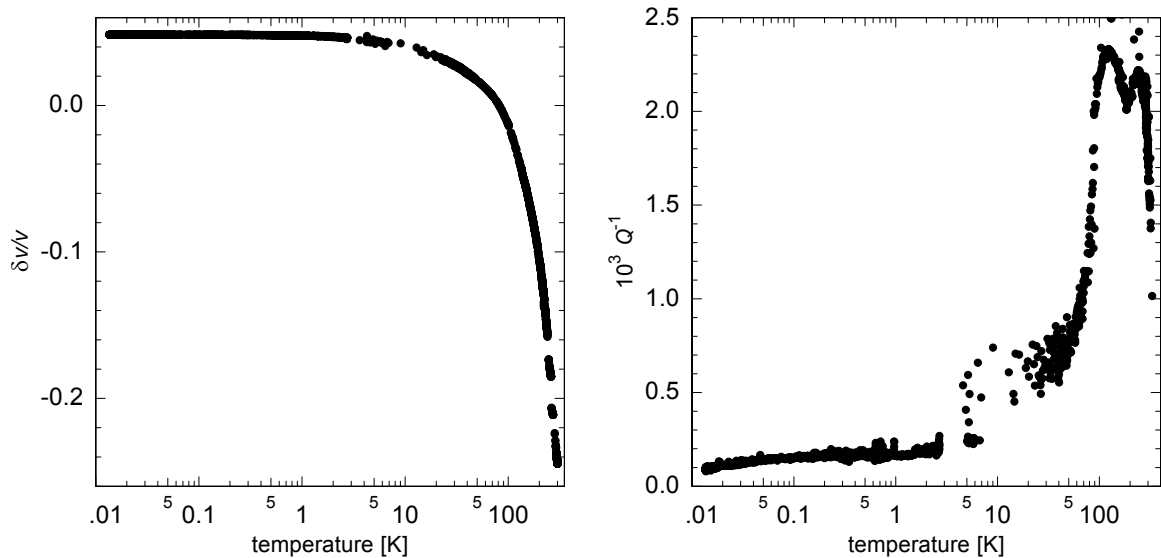


**Figure 4.8:** Overview over the relative change in the speed of sound (left) and the internal friction (right) at 182 Hz from 10 mK to 300 K.

### 4.2.2 Acoustic Measurements

**Speed of Sound Dispersion** The data shown in Fig. 4.9 were acquired using the resonance peak logging method with 100 samples to be averaged to one data point. The standard deviation of this set of samples is used to calculate the uncertainty on each measurement via Gaussian error propagation. The two lowest frequencies, 180 Hz (B1) and 260 Hz (ST), were measured using a different, slightly thinner DPO, than the other four frequencies. At low temperatures the B1-mode of the thicker DPO happened to lie exactly at a harmonic of the

power grid frequency of 50 Hz and was therefore not measurable. The speed of sound data were shifted along the vertical axis to allow for better comparison of the individual frequencies. Since  $\frac{\delta v}{v}$  is a relative quantity, which measures the change of the resonance frequency and thus of the speed of sound, adding a constant to the data does not change their physical meaning. Above 200 mK the curves of all six measured frequencies have a common slope. According to Table (2.1) the slope in the one-phonon-process dominated regime is governed by the parameter  $C = p_0 \gamma^2 / (\rho v^2)$ . From a semi-logarithmic linear fit it is determined as

$$-\frac{1}{2}C = (-5.21 \pm 0.08) \times 10^{-4} \Rightarrow C = (10.4 \pm 0.2) \times 10^{-4}. \quad (4.12)$$

Taking an absolute value of the speed of sound in polystyrene of  $v = 1.8 v(300 \text{ K}) = 4320 \text{ m s}^{-1}$  [War61] and a TLS density calculated from thermalisation measurements, cf. Eq. (4.11), the phonon-TLS coupling constant evaluates to

$$\gamma = \sqrt{\frac{C \rho v^2}{p_0}} = (0.18 \pm 0.01) \text{ eV} \quad (4.13)$$

which agrees well with coupling constants measured for other samples, e.g.  $\gamma = 0.24 \text{ eV}$  for transverse waves in BK-7 [Hun75]. For lower temperatures, however, several observations are striking. First, the slope of the resonant contribution is very small. According to the STM it should be of opposite sign and twice as large as the combined slope of relaxation and resonant branch at higher temperatures. Here, it is lower or at most equal (for 182 Hz) to the high-temperature slope for all frequencies. Second, there is no clear maximum in the data defined by the onset of the relaxation contribution. The speed of sound rather gradually flattens off before slowly starting to decrease again. Third, the data do not exhibit any clear frequency dependence despite the fact that the STM predicts a change of the maximum position with  $T_{\text{max}} \propto f^{1/3}$ , cf. Eq. (2.54). Here, the flattening-off occurs for different frequencies in almost the same temperature region. Only for 180 Hz and 260 Hz, that is for the two lowest frequencies, one can make out differences to the other modes towards lowest temperatures.

**Internal Friction** On the right hand side of Fig. 4.9 the internal friction of the DPO is shown as a function of temperature. One can clearly see the NCL plateau at temperatures above 100 mK. This occurs for all frequencies except for the F mode at 6.1 kHz, which shall therefore not be considered for further analysis. The two data sets obtained from a different DPO,  $f = 182 \text{ Hz}$  and  $260 \text{ Hz}$ , were shifted along the vertical axis by a constant amount so that the high-temperature plateau coincides with the one of the other frequencies. This is justified by a likely difference in the residual damping due to clamping losses. From fitting a constant to the plateau level and relating this value to the predictions of the STM one obtains

$$\frac{\pi}{2}C = (6.0 \pm 0.2) \times 10^{-4} \Rightarrow C = (3.8 \pm 0.1) \times 10^{-4}. \quad (4.14)$$

This deviates from the corresponding value as found in the speed of sound in Eq. (4.12) by a factor of 2.7.

Below 100 mK the internal friction decreases by an amount ranging from  $\Delta Q^{-1} = 1 \times 10^{-4}$  for 410 Hz to  $\Delta Q^{-1} = 3 \times 10^{-4}$  for 3.6 kHz. This is a strange feature, though, since according to the STM the throw should be frequency independent. Here, the throw first decreases, has a minimum at 410 Hz and then increases again. Also the onset of the decrease, which should shift to higher temperatures with increasing probing frequency, is not a monotonous function

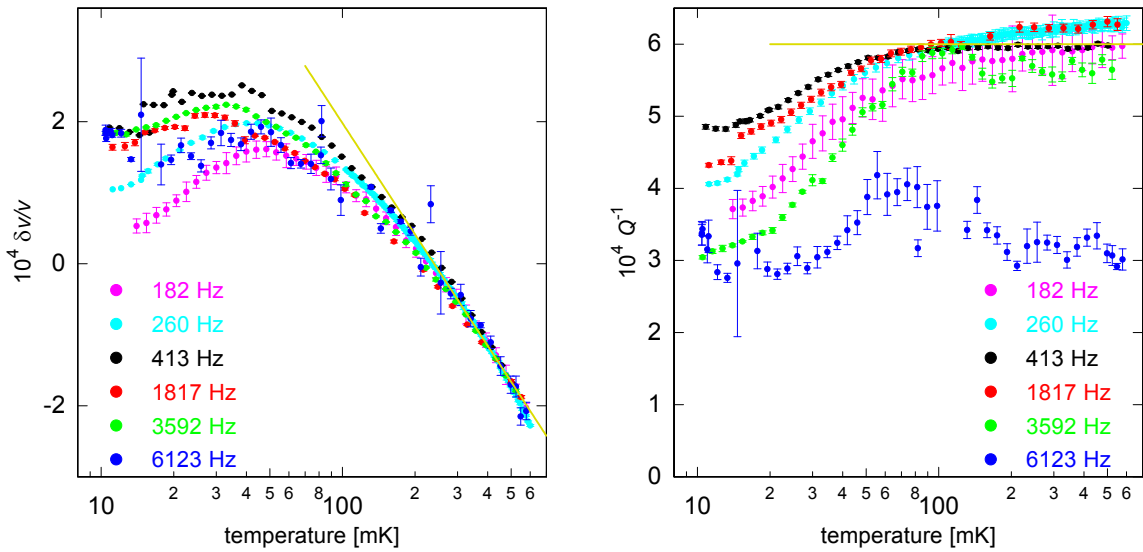


**Figure 4.9:** Relative change in the speed of sound (left) and the internal friction (right) from 10 mK to 600 mK for six different frequencies ranging from 180 Hz to 6.1 kHz. To the first four data points of the 260 Hz curve a constant of  $0.3 \times 10^{-4}$  was added both in the speed of sound and the internal friction in order to make the curves continuous. These points were measured at a large temporal distance to the rest. The linear curve in the speed of sound was fitted to the data between 200 mK and 600 mK and a constant was fitted to the internal friction between 100 mK and 600 mK under exemption of the 6.1 kHz data.

of frequency but rather exhibits the same peculiar frequency dependence as the throw. A last remarkable observation is the fact that even at 10 mK there is a residual internal friction of  $3 \times 10^{-4}$  to  $5 \times 10^{-4}$ . This value is approached for some frequencies approximately by a cubic temperature dependence as shown in Fig. 4.10 in accordance with the STM, cf. Table 2.1, but not for all frequencies. The residual internal friction might be explained by a temperature independent loss contribution due to the clamping. This could also make it plausible why different frequencies, which are differently affected by the clamping depending on the kind of oscillations, exhibit different residual losses. However, this discrepancy would also be visible in differences of the plateau levels. Since these differ by less than  $10^{-4}$ , though, there must be a contribution from another effect as well.

### 4.2.3 Dielectric Measurements

**Speed of Light Dispersion** The speed of light  $c = c_0/\sqrt{\varepsilon'}$  inside a medium depends on the real part of the medium's dielectric function  $\varepsilon$ . The change in the permittivity translates to a change of the speed of light as

$$\frac{\delta c}{c} = \frac{\partial c}{\partial \varepsilon'} \frac{\delta \varepsilon'}{c} = \frac{\partial c}{\partial \varepsilon'} \frac{\sqrt{\varepsilon'} \delta \varepsilon'}{c_0} = -\frac{c_0}{2\varepsilon'^{\frac{3}{2}}} \frac{\sqrt{\varepsilon'} \delta \varepsilon'}{c_0} = -\frac{1}{2} \frac{\delta \varepsilon'}{\varepsilon'}. \quad (4.15)$$

Hence, there is a relative minus sign between the changes of permittivity and speed of light turning the minimum of the permittivity into a maximum of the speed of light. For the sake of better comparing the elastic and dielectric susceptibilities with one another the latter is plotted in Fig. 4.11 in analogy to the relative change in speed of sound  $\delta v/v$  as the relative

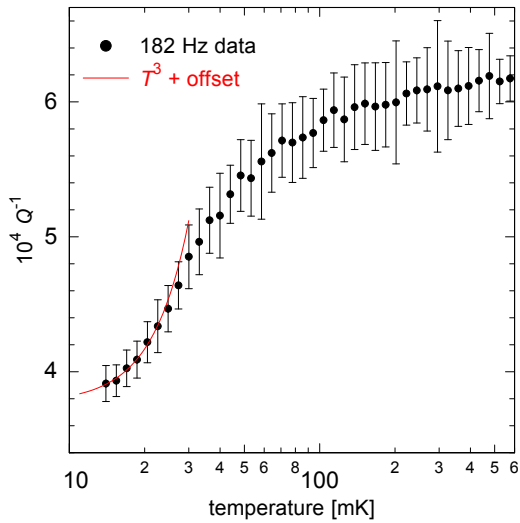


**Figure 4.10:** Internal friction at 182 Hz as a function of temperature. The data points at lowest temperatures can be described by a cubic dependence on temperature with an offset of  $3.8 \times 10^{-4}$  (solid line).

change in speed of light  $\delta c/c$ . The data of frequencies covering more than two orders of magnitude between 60 Hz and 16 kHz collapse on a single curve for  $T > 200$  mK if one allows for a vertical shift. This is justified by the fact that we are dealing with a relative quantity. For 60 Hz and 1 kHz below 100 mK the change of the speed of light flattens off completely without exhibiting a maximum. It appears that the resonant branch is either completely absent or compensated by another contribution. From fitting a linear curve to the high-temperature data in this semilogarithmic plot one obtains a value of  $C_d = (4.0 \pm 0.2) \times 10^{-4}$  for the dielectric macroscopic coupling constant, cf. Eq. 2.61. This agrees well with the corresponding value as obtained from the internal friction plateau of the acoustic measurements although the coupling between the TLS dipole moment and the probing field are different. In dielectric measurements the strain field coupling constant  $\gamma$  is replaced by the dipole moment  $|\mathbf{p}|$ . Another aspect is that mechanical probing is sensitive to all TLS while electrical probing only excites those TLS that carry a dipole moment, which experiments on the borosilicate glass BK-7 have shown to be around 60% [Lae77]. At 16 kHz a defined maximum appears at 60 mK. Below this temperature the change of the speed of light again flattens off until at 10 mK the slope vanishes. As a consequence the slope ratio of the resonant and resonant plus relaxation branch is not  $2 : -1$  as expected from the STM but it is rather reduced to  $\lesssim 1/2 : -1$ .

**Loss Tangent** On the right hand side of Fig. 4.11 the loss tangent at 16 Hz is plotted as a function of temperature. It qualitatively displays the shape expected from the STM, the NCL plateau at high temperatures and a decrease towards lower temperature. From the plateau level the macroscopic coupling constant  $C_d = (4.31 \pm 0.01) \times 10^{-4}$  can be calculated in analogy to Eq. (4.14). This is in good agreement with the value obtained from the high-temperature speed of light slope. Towards lowest temperatures, though, discrepancies to the STM arise. The loss tangent does not decrease to zero following a cubic temperature dependence. One rather finds a residual loss of about  $5 \times 10^{-4}$  at 7 mK. The loss data at 60 Hz and 1 kHz were so noisy that averaging disguised any temperature dependence which is why they are not shown here.

The results from the dielectric measurements qualitatively confirm the main findings of the acoustic experiments, namely that at sufficiently low probing frequencies first, for low

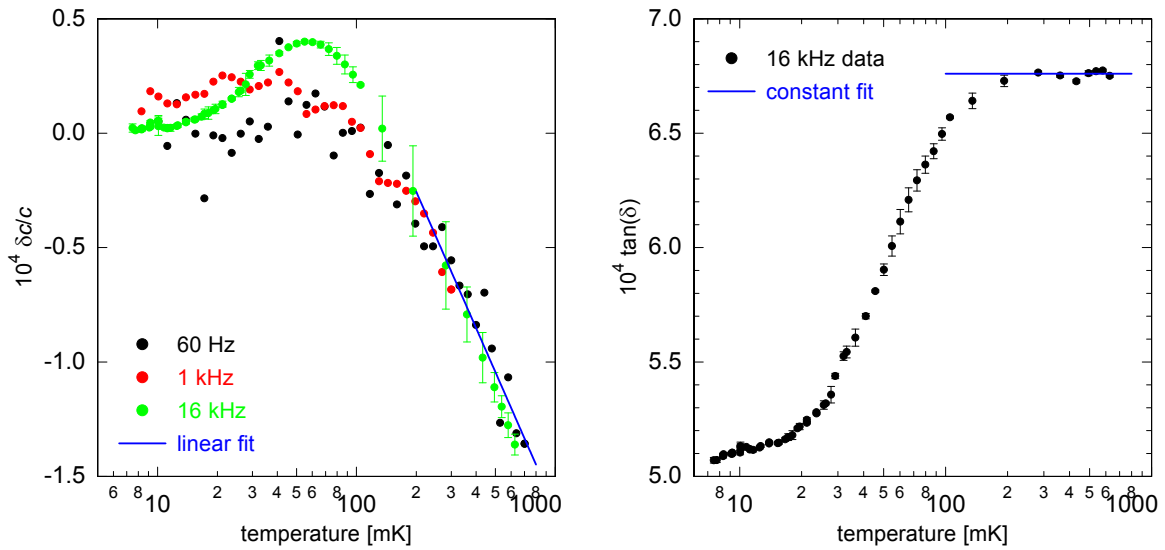


**Figure 4.11:** Relative change of the speed of light as measured by changes of the real part of the dielectric function for 60 Hz, 1 kHz and 16 kHz (left) and loss tangent at 16 kHz (right). The solid line in the speed of light is a linear fit of the high-temperature data with a slope of  $(-2.0 \pm 0.1) \times 10^{-4}$ . The plateau level of the loss data marked by the solid line lies at  $(6.76 \pm 0.02) \times 10^{-4}$ .

temperatures the data flatten off instead of exhibiting a distinct maximum and second, there is no clear frequency dependence.

### 4.3 Numerical Calculations

In order to quantify the disagreement between the measuring results from the acoustic measurements and theoretical predictions numerical simulations were performed using the software tool Mathematica<sup>1</sup>. The implementation was based on the algorithms by [Luc16] and modularly extended to account for different extensions of the STM, since not all the required equations can be solved analytically. For all simulations the lower (higher) integration boundary of the distribution function was chosen as  $E_{\min}$ ,  $\Delta_{0,\min} = 2 \times 10^{-8} \text{ K } k_{\text{B}}$  ( $E_{\max} = 5 \times 10^2 \text{ K } k_{\text{B}}$ ) satisfying that there is a sufficiently large margin between the boundaries and all corresponding temperatures relevant in the experiments,  $E_{\min}/k_{\text{B}} \ll T_{\text{exp}} \ll E_{\max}/k_{\text{B}}$ . It was observed that the exact choice of the integration limits scarcely affected the outcome of the simulations as long as the margin with respect to  $k_{\text{B}}T_{\text{exp}}$  is preserved. If the upper limit is chosen too high, though, e.g.  $E_{\max} > 1 \times 10^3 \text{ K } k_{\text{B}}$  numerical instabilities occurred resulting in artificial steps in the simulated data whose position and shape depended on the value of  $E_{\max}$ . The main purposes of the numerical calculations was to elucidate the deviations of the data from the expected frequency dependence and to attribute them to either the resonant or the relaxation contribution.

<sup>1</sup>Wolfram Mathematica 8.0, The Wolfram Centre, Lower Road, Long Hanborough, Oxfordshire, OX29 8FD, UK

### 4.3.1 Standard Tunnelling Model

If one limits oneself to considering only one-phonon relaxation processes which is adequate for the temperature range of concern,  $T < 1$  K, the STM is completely described by two free parameters: the macroscopic coupling constant  $C$  and the one-phonon relaxation strength, the prefactor of Eq. (2.44), which can be encoded in the real part maximum position  $T_{\max}(f)$  via Eq. (2.54). As the latter is a quantity on a more natural scale  $T_{\text{ref}} := T_{\max}(1 \text{ kHz})$  shall be used as a measure of the relaxation strength. These two parameters were tuned to fit the 410 Hz data yielding  $C = 3.8 \times 10^{-4}$  and  $T_{\text{ref}} = 45 \text{ mK}$ . The same values were used for modelling the other frequencies as well both in the speed of sound and the internal friction. The macroscopic coupling  $C$  agrees with the value found from the plateau level of the internal friction, cf. Eq. (4.14), as can also be seen in the plateau level of the simulated internal friction curves. It disagrees, though, with the corresponding value as obtained by the speed of sound slope. This may be due to the fact that the latter stems from a fit of the high-temperature end of the data while in the simulations the fit spans the entire temperature region. Although the high-temperature part of the data, i.e. the regime where both relaxation and resonant processes contribute, can be described quite well for all frequencies, large deviations occur on the low-temperature side. The maxima of the simulated curves shift to higher temperatures obeying  $T_{\max} \propto f^{1/3}$  whereas the data do not. Hence, the discrepancies between simulation and data increase for larger differences to the reference frequency 410 Hz, both in positive and in negative direction. As for the internal friction one finds that the plateau levels match the theoretical expectations if no constant residual damping is assumed but neither the onset of the decrease and its frequency dependence nor the throw agree between simulation and measurement.

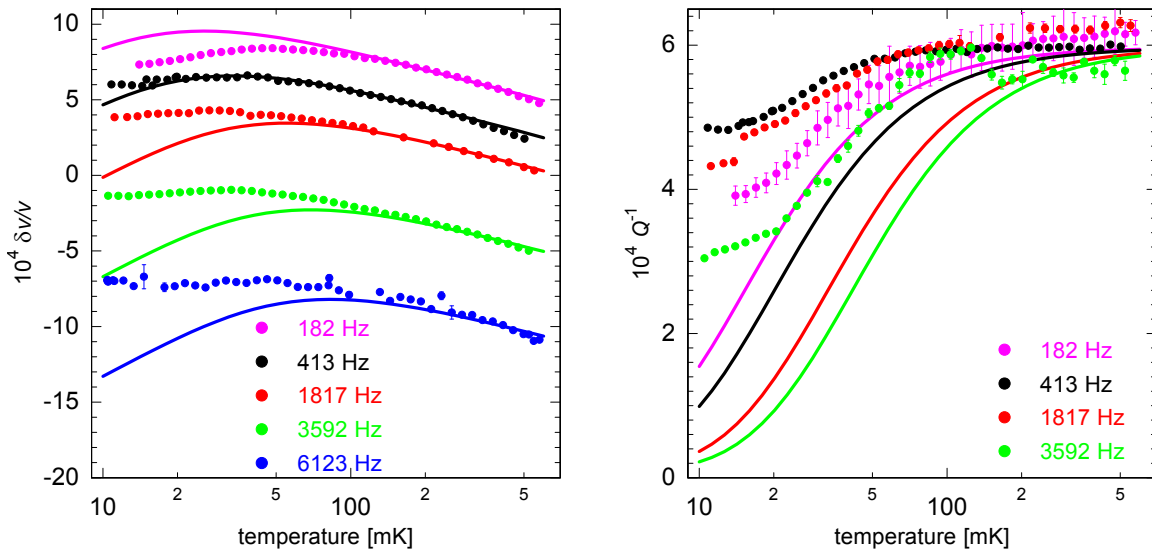


**Figure 4.12:** The solid lines are predictions of the STM for the speed of sound (left) and the internal friction (right) while the points show the data. For all simulated curves the same parameter set,  $C = 3.8 \times 10^{-4}$  and  $T_{\text{ref}} = 45 \text{ mK}$ , was used.

In conclusion, one may say that the high-temperature speed of sound and internal friction data can consistently be described by the macroscopic coupling parameter  $C$  of the STM. The frequency dependence as postulated by the STM cannot be reproduced, though, yielding different values of  $T_{\text{ref}}$  if every frequency is fitted separately as was done in Fig. B.11. This

suggests that direct relaxation of TLS induced by phonons might not be the only relaxation mechanism involved and one has to consider extensions to the STM.

### 4.3.2 Resonant Susceptibility

In Fig. 4.13 a model which claims changes of the resonant contribution due to a misalignment of the nuclear spin quantisation axes, as introduced in Section 2.2.2, is compared to the empirical data. Increasing the number  $n$  of nuclei per TLS which take part in a collective tunnelling motion shows that the slope of the resonant branch is reduced because of a wider pseudogap in the distribution function. For the case of a probing frequency of 3.6 kHz on average  $n = 3$  nuclei per TLS would be necessary to describe the data. The nuclear spin wavefunction overlap integral  $\eta$  on the other hand does not have a significant impact on the shape of the speed of sound curve as demonstrated in Fig. B.12. However, if the same parameter set is applied to the remaining frequencies the description breaks down. Furthermore, this theory does not alter the modelling of the internal friction since for low-frequency experiments the resonant contribution to the absorption is negligible.

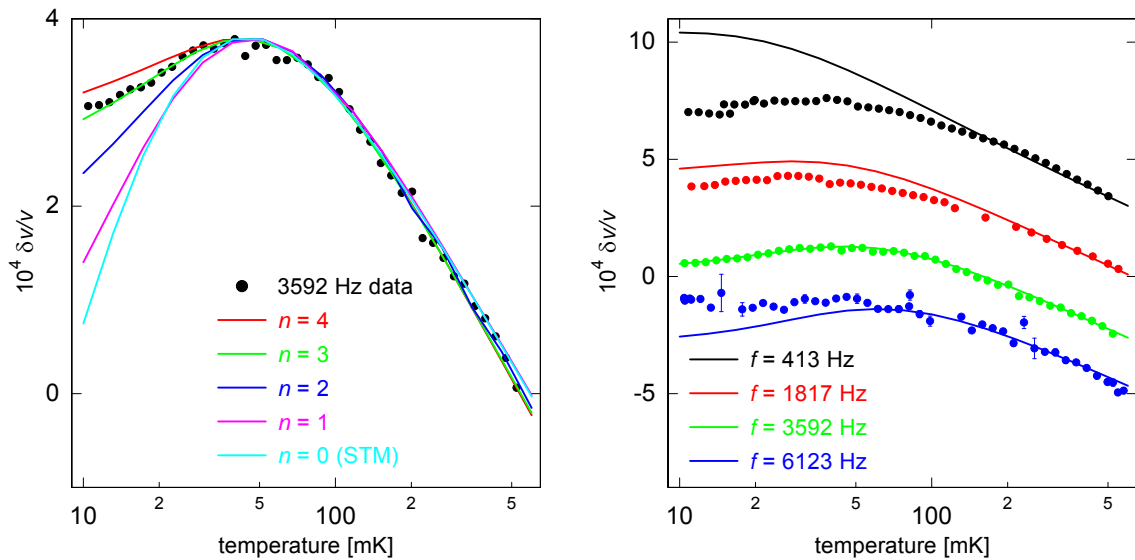


**Figure 4.13:** The predictions of the resonant susceptibility model assuming a quadrupole splitting of  $\nu_q = 250$  MHz and a spin overlap integral of  $\eta = 0.1$  for varying numbers  $n$  of nuclei forming a TLS compared to the measured data of 3592 Hz (left). Taking the same parameters, that had been tuned for 3.6 kHz, for all frequencies,  $n = 3$ ,  $\eta = 0.01$ ,  $C = 4.1 \times 10^{-4}$  and  $T_{\text{ref}} = 55$  mK, the model fails to describe the data of the other frequencies (right).

Hence, one is lead to the observation that the resonant susceptibility model is not by itself capable of explaining the data. The agreement with just a single frequency data set might be of purely coincidental nature but does not manifest a hint that this model would be suited for the sample and temperature range at hand. If one still wanted to adhere to it then additional extensions would have to be included as well.

### 4.3.3 Additional Relaxation Rate

Including another relaxation process, induced by nuclear quadrupole moments, into the STM, as presented in Section 2.2.3, allows to qualitatively reproduce the speed of sound data as shown on the left hand side of Fig. 4.14. With a single parameter set,  $T_{\text{ref}} = 7 \text{ mK}$ ,  $C = 3.85 \times 10^{-4}$  and  $\tau_0^{-1} = 250 \text{ kHz}$  for the constant phenomenological quadrupole relaxation rate of Eq. (2.80), the simulated curves qualitatively agree with the data. For all simulations a nuclear quadrupole splitting frequency of  $\nu_q = 250 \text{ MHz}$ , corresponding to the mean splitting of both bromine isotopes, was used. This model is able to correctly account for the fact that the maximum position does not shift with frequency as suggested by the STM. Yet, the 182 Hz curve, which has been measured with a second DPO, exhibits a maximum lying at a higher temperature than the one of the other frequencies which is not reflected in the model. For the internal friction using the same parameters did not yield a satisfactory agreement between model and data. Even by changing the parameters under consideration of the experience gained from the model characterisation no complete accordance could be achieved. At best merely the temperature dependence of the internal friction of a single frequency could be partially described. For this the reference temperature had to be increased to  $T_{\text{ref}} = 25 \text{ mK}$  and the constant rate reduced to  $\tau_0^{-1} = 1 \text{ kHz}$ . Only the macroscopic coupling constant  $C$  could be kept consistent between speed of sound and internal friction simulation which had already been the case for the pure STM, though. The NQM driven relaxation model does produce a local maximum around the temperature that corresponds to the quadrupole splitting and which could be attributed to the flattening off of the internal friction data below 20 mK, demonstrated in Fig. B.13. Although the main features of the data, that is a plateau at higher temperatures, a decrease below a certain temperature and a flattening off towards 10 mK, are qualitatively captured by the simulations, the decrease below 100 mK is systematically steeper in the data than in the simulated curves, though. Besides, different frequencies require different values for  $T_{\text{ref}}$ .

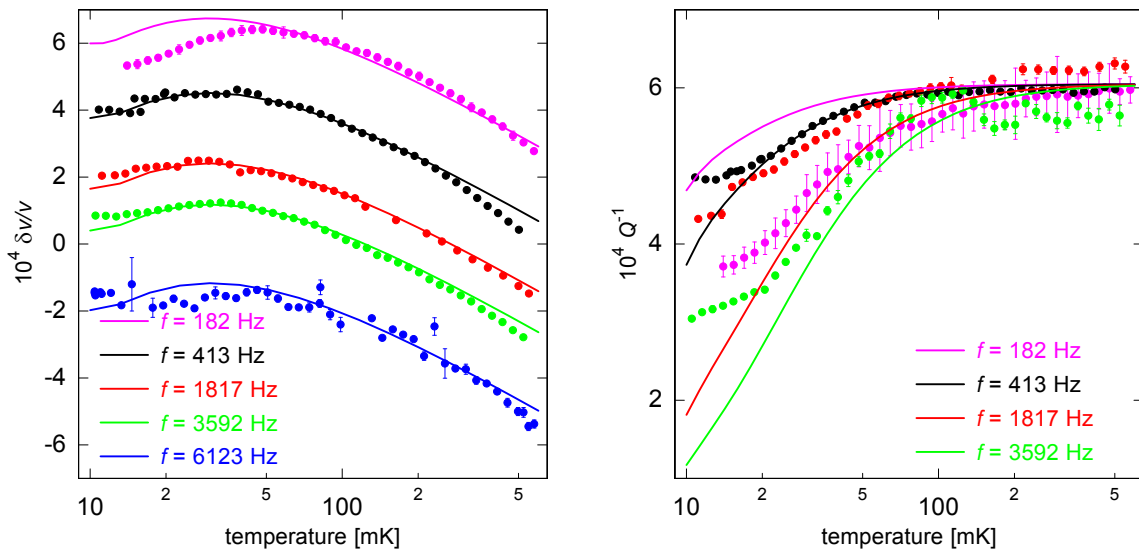


**Figure 4.14:** Comparison between model and data of speed of sound (left) and internal friction (right) under the assumption of an additional NQM driven relaxation process with  $\nu_q = 250 \text{ MHz}$  and  $C = 3.85 \times 10^{-4}$ . For the speed of sound simulations  $T_{\text{ref}} = 7 \text{ mK}$ ,  $\tau_0^{-1} = 250 \text{ kHz}$  were used and for the internal friction  $T_{\text{ref}} = 25 \text{ mK}$ ,  $\tau_0^{-1} = 1 \text{ kHz}$ .

As a result one may conclude that in qualitative terms a NQM driven relaxation process is able to account for some of the features of the experimental findings, mainly the frequency independence of the maximum in the speed of sound. However, the internal friction cannot be consistently described by this specific model.

#### 4.4 Impact of RF Bias

**Bias Frequency Sweep** The results of sweeping the RF bias frequency with the quadrupole transition drive module at constant input power  $P_b = -35$  dBm are shown in Fig. 4.15. At 39 MHz and 200 MHz there are broad peaks in the temperature of the experimental platform of the cryostat. Two thermometers, a resistance and a noise thermometer, independently confirmed the temperature rise ruling out that this was merely a cross talk between the bias and thermometer signal lines. The peaks in the temperature course can also be found in the internal friction where they manifest themselves as broad maxima. In addition, two other peaks are discernible, one at 270 MHz and another one at 550 MHz. In the speed of sound data at all of these frequencies there are features as well, both dips and peaks. Its overall profile is a lot flatter than the internal friction profile, though, which could be explained by the fact that there is a maximum in the temperature dependence of the speed of sound while the internal friction increases monotonically. The data were acquired with increasing bias frequency at a step size of 0.2 MHz. This is the reason for the sudden and discontinuous rise of the internal friction at very low bias frequencies. Starting from the initial situation with 0 MHz, that is no bias field at all, already relatively low bias frequencies have a large effect on the paddle oscillations.

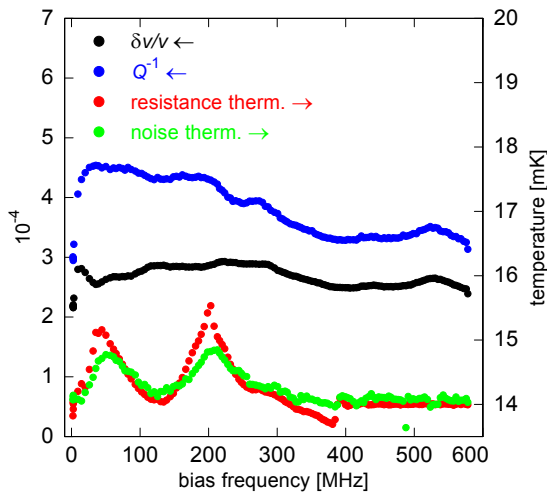


**Figure 4.15:** Response of the sample upon a sweep of the bias frequency at constant input power  $P_{\text{bias}} = -35$  dBm. Both a resistance and a noise thermometer recorded a temperature increase of the experimental platform at two specific bias frequencies. The speed of sound and the internal friction exhibit a broader frequency dependence and additional features which do not leave a trace in the temperature data. Since both quantities are dimensionless and of the same order of magnitude they are plotted on the same left axis.

Although the peak at 270 MHz seems to match the literature value of the quadrupole splitting frequency of one of the bromine isotopes,  $^{79}\text{Br}$ , it cannot be unambiguously attributed to it. First, with a linewidth of around 30 MHz it is broader than typical quadrupole resonance peaks of amorphous materials which are below 10 MHz [Rub74]. Second, a resonance peak for the second bromine isotope,  $^{81}\text{Br}$ , is expected from the ratio of their quadrupole moments of 1.2 at 225 MHz. Since the natural abundance of these two isotopes is roughly the same the peaks should be of similar height. This second peak cannot be identified, though. Either it is overridden by the large feature centred around 200 MHz or it does not exist. Hence, from this measurement alone no clear evidence can be gathered whether or not some of the features were caused by NQM.

**Bias Power Sweep** When the input bias power  $P_b$  is gradually increased from  $10^{-8}$  mW to  $10^{-3}$  mW the temperature of the experimental platform starts to rise for powers exceeding  $10^{-4}$  mW as can be seen in Fig. 4.16. The power was incremented in steps of 2.3% with a waiting time of 40 min in order to allow the system to reach steady state conditions. The internal friction of the sample already increases for  $P_b \geq 5 \times 10^{-6}$  mW. With the help of the internal friction data  $Q^{-1}(T)$  from Fig. 4.9 an interpolation table can be constructed that allows to convert  $Q^{-1}(P_b)$  to the temperature of the sample  $T_{\text{DPO}}(P_b)$ . This is possible because  $Q^{-1}(T)$  is a strictly monotonic function of temperature for  $T < 100$  mK. That procedure assumed that the observed change in the internal friction was solely of thermal origin and not caused by manipulating the interaction between NQM and TLS. After this conversion one finds that below  $5 \times 10^{-6}$  mW the temperature of the sample equals the temperature of the experimental platform, 10.9 mK while above it rises at an increasing rate up to 46 mK. Each of these black data points in Fig. 4.9 is the average of 100 readings. If the assumption of a mere thermal effect is correct then there is a large and growing temperature difference between the sample and the thermal bath of the cryostat. This could be explained by the leg of the DPO constituting a weak thermal link between the sample and the experimental platform. The bias power deposits a heat input

$$Q_{\text{bias}} = \frac{\Omega}{4\pi} \left(1 - 10^{\frac{2S_{11}}{10}}\right) P_b \quad (4.16)$$

onto the DPO where  $S_{11} \approx -0.001$  dB is the reflection parameter of the bias loop at 270 MHz as obtained from the module characterisation simulations, cf. Fig. 3.12, and  $\Omega \approx 2\pi$  the solid angle covered by the DPO from the perspective of the loop as an emitter. Considering the thermal conductance  $G(T) = G_0 T/T_0$  of the gold film with a temperature dependence given by the Wiedemann-Franz law the temperature difference between the sample and the cryostat can be estimated to be  $\Delta T_{\text{DPO}} = Q_{\text{bias}}/G(T)$ . It is given by the blue curve which quantitatively describes the temperatures rise of the sample. For the calculation a thermal conductance  $G_0 = G(10 \text{ mK}) = 3.5 \text{ nW K}^{-1}$  was used which is within a factor of two comparable to the estimation of Eq. (3.14). The skin depth of gold at a frequency of 200 MHz is given by

$$\delta_{\text{Au}} = \sqrt{\frac{\rho}{\pi f \mu}} \approx 4 \text{ } \mu\text{m} > d_{\text{Au}} \quad (4.17)$$

where  $\rho$  is the electric resistivity and  $\mu = \mu_0 \mu_r \approx \mu_0$  the magnetic permeability. Thus, the electromagnetic field extends throughout the entire gold film. This suggests that a likely cause for the temperature increase are dissipative eddy currents in the gold layer. That does not exclude that bromine nuclei are excited into the upper quadrupole levels as well and subsequently release the energy as heat into the phonon bath which would also increase the sample temperature. However, for bias power sweeps performed at a frequency that does not match the bromine quadrupole splitting the temperature rise is still the same. If the NQM did play a major role in the heating then one would expect to see a step in the DPO temperature corresponding to the saturation of all involved transitions. Any further increase of the bias power could then raise the sample temperature only by means of eddy currents. Since such a step is not observed one can consider this measurement only as an upper limit on the detectability of nuclear quadrupole transitions by this method. Furthermore, as the change in the internal friction can be well modelled by the temperature increase of the sample this is an indication that from these data it cannot be concluded whether or not the deviations from the STM of Fig. 4.9 are caused by the NQM.

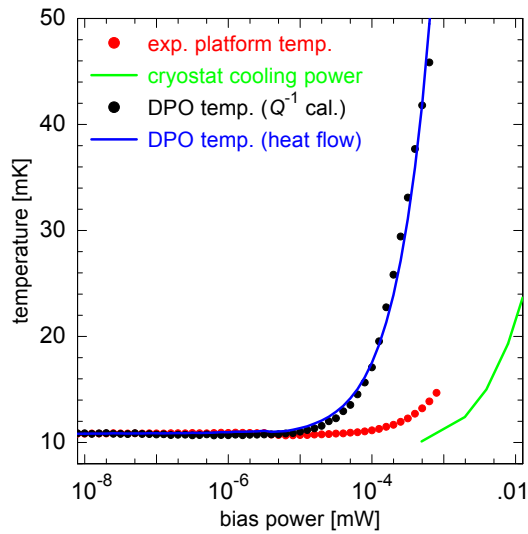


**Figure 4.16:** Temperature rise of the DPO (black) and the experimental platform (red) upon an increase of the bias power at constant bias frequency  $f_{\text{bias}} = 270$  MHz. The temperature of the DPO is calculated from the internal friction using linear interpolation of the previously acquired  $Q^{-1}(T)$  curves. Estimating the heat flow through the DPO leg due to a temperature gradient between sample and experimental platform the temperature rise of the sample can be modelled. The green curve shows the cooling power of the cryostat (on the  $x$ -axis) at different temperatures.

On the  $x$ -axis the cooling power of the dilution refrigerator for different temperatures, measured by [Rei13], is indicated by the green curve of Fig. 4.16. One can see that the temperature dependence of the cooling characteristics, given by Eq. (3.4), is similar to the cryostat temperature profile (red points). Yet, there is a deviation of a factor five between the two curves.

A possible explanation to consolidate the different findings of Fig. 4.16 is that the bias loop deposits most of the energy into the DPO, which is what it was designed for. This leads to a temperature rise of the sample shown by the increase of the internal friction. The heat cannot instantly flow into the experimental platform due to the small thermal conductance of the DPO leg which leads to the built-up of a continuously growing temperature gradient. Up to a certain input power, around  $10^{-4}$  mW, the mixing chamber of the cryostat can compensate for the additional heat. Above this threshold that is no longer possible and also the temperature of the experimental platform rises following the limit of the cooling power. A potential reason for the deviation between the cooling power curve and the experimental platform temperature might be the fact that the former was measured five years ago and since then the cooling power has worsened and consequently the lowest achievable temperature has also increased to 10 mK.

**Complex Plane Representation of the Elastic Susceptibility** The aim of the bias module was to investigate whether NQM were the reason for the deviations from the STM. In the previous paragraph it was shown that upon application of a bias input the change of the internal friction could be explained by an increase of the sample temperature. In order to rule out whether alternative or complementary explanations were possible, too, the data need to be presented in a temperature independent way as was done in Fig. 4.17. Changes of the speed of sound are linked to the real part of the elastic susceptibility and the internal friction to its imaginary part. So plotting  $Q^{-1}(\frac{\delta v}{v})$  yields a scatter plot in the complex plane that does not have an explicit dependence on temperature. The data set at 270 MHz, where the quadrupole resonance is expected to be found, is compared to two other bias frequencies and to a reference without bias. All four curves lie on top of each other exhibiting the same trajectory in the complex plane. Since the NQM driven relaxation would modify the temperature dependence of the speed of sound and the internal friction in a different way as illustrated with the help of simulations on the right hand side of Fig. 4.17 one can conclude that the bias signal did

not have the intended effect to selectively switch on and off the NQM driven relaxation. So the observed signal change is purely of thermal origin.

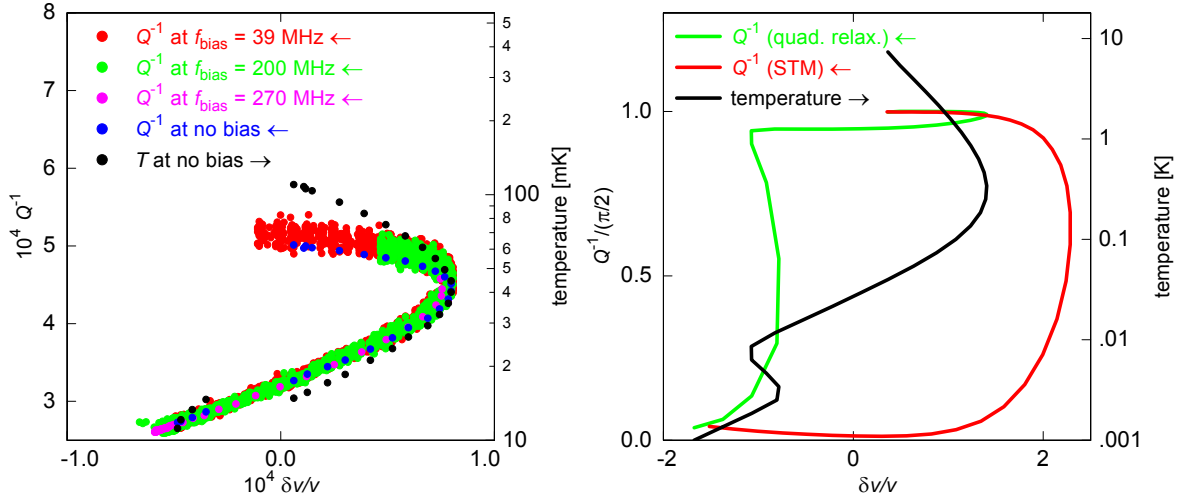


**Figure 4.17:** The response of the sample upon increasing the input power is plotted in the complex plane. On the left hand side data of different bias frequencies (red, green, purple), which had not been averaged, are compared to the unbiased case (blue). The sample temperature for a specific value of the speed of sound change can be retrieved from reading the corresponding reference value (black) from the right axis. On the right hand side the shapes of simulated trajectories for the STM with (green) and without (red) an additional quadrupole moments driven relaxation rate are compared to each other. The parameters used were  $T_{\text{ref}} = 100$  mK,  $C = 1$ ,  $\nu_q = 270$  MHz and  $\tau_0^{-1} = 100$  kHz.

The electromagnetic characterisation simulations in Section 3.3.3 yielded an estimate of the AC magnetic field amplitude inside the sample of  $\hat{B}_1 \sim 1 \mu\text{T}$  at the maximum bias input voltages used. The characteristic time scale  $\tau$  to change the population of the hyperfine levels is given by the inverse Rabi frequency  $\Omega_R = \gamma_{\text{Br}} \hat{B}_1$ . It follows  $\tau \sim 90$  ms. The applied bias field continuously drives hyperfine transitions. However, according to the results of the numerical simulations the relaxation rate induced by NQM in the framework of the analysed model would be in the kilohertz regime. This mismatch of time scales might explain why the current experiment does not succeed in discriminating between dominant NQM driven relaxation and relaxation governed by one-phonon processes. Increasing the RF bias voltage for the sake of faster Rabi oscillations results in too much heat input which drives the sample out of the low-temperature regime where the discrepancies would occur.



## 5. Discussion

### 5.1 Validity of Data

**Thermalisation** As was shown in Section 4.1.4 the sample took a rather large amount of time to reach thermal equilibrium with the mixing chamber. At around 20 mK even after 2 h there was still some signal change discernable. Thorough thermalisation measurements of multi-component glasses containing NQM showed that the thermalisation times of these specimens diverge as  $aT^{-3} + bT^{-1}$  [Luc16]. A different dielectric glass containing bromine, Br-DGEBA, also exhibits very long thermalisation times of greater than 5 h at such low temperatures [Aßm18]. It is therefore possible that the data below 20 mK are affected by insufficient thermalisation which could be one explanation for the flattening off of the internal friction. The reduced slope of the speed of sound change at the low-temperature side of the maximum is a separate phenomenon, though. It already occurs above 20 mK at temperatures for which there is still a decrease of the internal friction. Also, the rather large residual loss and internal friction cannot be explained by thermalisation arguments alone. Some temperature ramps were acquired with increasing and others with decreasing temperature but both sets of measurements exhibit large residual losses.

**Data Acquisition** For the acoustic experiments two different data acquisition approaches were possible, either recording entire resonance peaks and fitting Lorentzian functions to the data or logging the position of the resonance frequency. In this work the former was employed for the voltage scaling experiments because it yielded an absolute value for the internal friction. It allowed to directly assess the shape of the resonance curve in order to early identify asymmetries and non-linear drive. The resonance frequencies obtained from fitting the Lorentzian line shape of the resonance amplitude and fitting the phase course agreed with each other within the errors. For the speed of sound change and internal friction measurements at low temperatures the data presented here were acquired with the frequency logging method. A resonance curve at a single temperature was acquired in order to transform the relative internal friction data into absolute values. For some modes of the DPO entire resonance curves were recorded additionally in order to monitor the resonance shape throughout the temperature ramp and to compare the quality of the results with the logging technique. It turned out that the final result SNR of the frequency logging method is larger than for the fitting method. This may be due to the fact that if for some reason an unforeseen disturbance occurs the fit is very sensitive to the timing with respect to the peak position. Such sporadic signal bursts were indeed observed but not understood. A sudden burst right at the peak can alter the apparent parameters of the resonance while towards the edge this is less problematic. As for the logging case an arbitrary long array of data samples is averaged and so the timing of the burst is irrelevant. Another disadvantage of the fitting method is the way the statistical errors on the results can be calculated. They are obtained from the uncertainty of the fit parameters. Considering the scatter of the data, e.g. in the plateau level of the internal friction, these errors by far underestimate the true error. The internal friction data are systematically noisier than the speed of sound data and also the error bars of a given frequency are larger for the former. This could be made plausible by acknowledging the large steepness of the phase course at resonance, which is the guide for the logging procedure. That means that small changes of

the measured voltages at both channels result in small changes of the phase  $\pi/2 + \Delta\varphi$ . The relative error of the resonance frequency  $\Delta f_0/f_0 \sim \Delta\varphi/(2Q)$  is then suppressed by the quality factor, cf. Eq. (3.34). The relative internal friction error on the other hand is equal to the relative voltage changes at the peak of the resonance amplitude curve. A source of systematic internal friction error could be temperature independent clamping losses due to the way the DPO is attached to the sample holder. Depending on how large the displacement of a certain mode at the clamping position is different modes are affected differently with the torsional modes being affected least. The contribution to the internal friction stemming from the gold film,  $0.17 Q_{\text{Au}}^{-1}$ , see Eq. (3.18), cannot account for the residual internal friction since for  $T \rightarrow 0$  in such systems without TLS the thermoelastic loss is already several orders of magnitude smaller and vanishes along with the phonon density [Hou02].

**Self Heating** The internal friction is defined as the relative loss of energy per oscillation period, cf. Eq. (3.24). This energy is ultimately converted to heat which increases the sample temperature. The self heating power can be calculated from parameters of the DPO and the driving strength [Esq92]. For a quality factor of  $Q > 2000$ , an oscillation amplitude of  $\xi < 1$  nm, see Eq. (4.8), and a DPO mass of  $m < 1$  g the self heating power at a frequency  $\omega/(2\pi) < 10$  kHz is smaller than

$$P_{\text{sh}} = \frac{1}{8} Q^{-1} \xi^2 \omega^3 m < 200 \text{ fW}. \quad (5.1)$$

Considering a thermal conductance of  $G_{\text{DPO}} \sim 2 \text{ nW K}^{-1}$ , see Eq. (3.14), this conservative estimation would lead to a maximum temperature difference of 0.1 mK between the sample and the experimental platform. Such a small systematic temperature error is within the symbol size of the data points in all plots of this thesis.

**Thermometry** A potential systematic temperature error resulting from the calibration process is hard to estimate but smaller than 2% [Rei17]. The statistical temperature error varies between around 1.5% at 7 mK and around 0.01% at 600 mK. Hence, errors of the measured temperatures are much smaller than the voltage signal errors in relative terms. In all plots shown the temperature errors are within the symbol size of the data.

**Sample Preparation** Fabricating double paddle oscillators from a powder of the sample to be investigated was a crucial part of this work. Issues and questions that arised during that process shall be addressed in the following.

**Quadrupole Moment of Gold** The acoustic measurements using a DPO made it necessary to cover the sample with a thin metal layer for which gold was chosen. Gold also possesses a sizeable nuclear quadrupole moment of  $Q_{\text{Au}} = (510 \pm 15) \text{ mb}$  [Bel07] which is almost twice as large as the NQM of bromine. Due to the fact that gold atoms form metallic rather than covalent bonds to their neighbours and are consequently surrounded by a cloud of delocalised electrons the electric field gradient and with it the quadrupole level splitting are vanishingly small. Gold has an electronic configuration of  $[\text{Xe}]4f^{14}5d^{10}6s^1$  so the outermost electrons are in the spherically symmetric s-orbital and all lower-energy orbitals are fully occupied. Hence, the existence of a quadrupole moment in gold nuclei is not relevant for the present case.

**Constant Strain due to Bending** After deposition of the gold film and milling the DPO was bent along its leg towards the gold coated side. This effect may be due to mechanical strain that has built up in the course of the sputtering and subsequent cooling process because of different thermal expansion coefficients of the two materials. If this was the reason then further bending should occur when cooling down the DPO in the cryostat. Yet, this is not an issue as long as the DPO does not touch the electrodes of the sample holder hindering it from oscillating freely. This problem would reveal itself by strangely shaped resonance curves to which no Lorentzian curve could be fitted. The mere presence of this constant strain  $e_0$  does not influence the results since it only changes the asymmetry energy of individual TLS by  $|\delta\Delta| = 2\gamma e_0$ . The TLS distribution is very broad, though, and so the macroscopic response is not altered, similar to reordering the terms in a sum. Also, the DPO is slightly bent by the bias voltage  $V_b$  anyway which is beneficial as this increases the SNR.

**Amorphousness of Sample** In Section 3.2.2 four different pieces of evidence were presented supporting the fact that the investigated sample actually had an at least partially amorphous atomic structure. Besides, the low-temperature results for the speed of sound and internal friction give a clear indication that the sample is amorphous. However, no quantitative proof by direct measurements, e.g. using x-ray diffraction, exists. This leaves residual odds that the sample consists of some crystalline parts embedded in an amorphous surrounding. If this was true then the only consequence would be a reduced TLS density and thus a smaller macroscopic coupling parameter  $C$  compared to the case of complete amorphousness. It would however not explain the observed peculiarities and deviations to the STM.

**Dielectric Measurements** Unlike in acoustic experiments the sample did not move during the dielectric measurements so clamping losses did not occur here. The loss contribution due to the vacuum grease on both sides of the sample disc was negligible because of the relatively small amount used in comparison to the sample volume.

## 5.2 Conclusion

### 5.2.1 Interpretation of Results

The main findings of this work were that in a specific polymer glass, that contains large nuclear quadrupole moments at sites with an appreciable electric field gradient, at low temperatures the description of the elastic and dielectric susceptibilities by the STM breaks down. In glasses at such temperatures TLS are the dominant degree of freedom and govern the temperature dependence of the above quantities. It was shown that some assumptions of the STM, e.g. the claim of a set of non-interacting TLS with a homogeneous parameter distribution, are not valid in the sample at hand. The consequence is that the assumptions underlying the STM have to be modified. The empirical observations are summarised in the following:

1. The slope on the low-temperature side of the maximum, that should be a pure resonant contribution according to the STM, is strongly reduced or even vanishes completely in the measurement errors.
2. At higher probing frequencies the maximum narrows and shifts to higher temperatures.

3. At yet higher frequencies, that is 16 kHz in this study, a second feature seems to develop at 10 mK, characterised by a vanishing slope.
4. Among the STM parameters the macroscopic coupling constant  $C$  can be matched between the data of the real and imaginary part while this is not the case for the one-phonon relaxation strength encoded in  $T_{\text{ref}}$ .
5. There is a rather large residual internal friction and loss at 10 mK.

The position of the speed of sound or light change maximum as a function of probing frequency is plotted in Fig. 5.1 in support of observation 1 and 2. Together with a measurement at 36 MHz [Her17] there seems to be a threshold frequency around 10 kHz below which the STM scaling of  $T_{\text{max}} \propto f^{1/3}$  does not hold anymore. Observation 4 implies that foremost the way how relaxation is treated by the STM needs revising. In an attempt to consolidate the observations one could claim that there are interactions between TLS and their environment or amongst the TLS themselves not accounted for in the STM. These additional interactions would result in more relaxation pathways other than one-phonon relaxation. At probing frequencies that are smaller than the inverse life time of the interaction partner's excitation or smaller than the inverse coherence time of the TLS and its interaction partner this relaxation channel has a chance to have an effect. In a sketchy picture one could think of an increased inertia of the TLS if it is wrapped in a cloud of interaction partners. If the probing frequency is larger than these rates the interaction partner is too slow to follow the external field and the interaction is suppressed. The energy loss of the TLS via this additional interaction would make up what had above been called the residual internal friction.

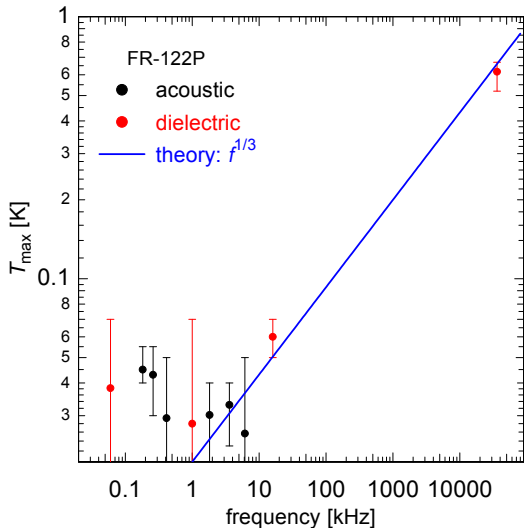


**Figure 5.1:** Frequency dependence of the speed of sound and speed of light change maximum temperature  $T_{\text{max}}$  from acoustic and dielectric measurements, respectively. The data point at 36 MHz was measured in [Her17]. In cases with vanishing resonant slope, i.e. when the data flatten off completely, the lower error bars extend to the bottom of the plot. The solid line indicates the expected frequency dependence  $T_{\text{ext}} \propto f^{1/3}$  from the STM. Below about 10 kHz the maxima become very broad or even disappear and their positions are independent of frequency.

Such interactions could be of different origins depending on the sample under investigation. Since FR-122P has a large bromine content it seems plausible that a suitable candidate for the interaction partner in question are nuclear quadrupole moments. There could be quadrupole or magnetic dipole coupling between the nuclear spins of bromine atoms belonging to different TLS. Another possibility is strain mediated coupling between a NQM carrying atom, that does not itself have to be part of a TLS, and a nearby TLS. This changes the EFG at the position of the atom by virtue of the tunnelling motion which alters the local electrochemical environment. That such an additional relaxation rate can qualitatively and to a minor extent also quantitatively explain the experimental findings was demonstrated with the help of

numerical simulations using a phenomenological model. In contrast, extensions to the STM because of a modified resonant contribution, such as a resonant process between matching quadrupole levels of both sides of the TLS double well, were shown to be less suitable to account for the deviations from the STM.

### 5.2.2 Comparison to Related Work

**Incoherent Tunnelling and Dipole Gap** The basic ideas leading to the interpretation of the results as discussed in the previous section are not new. Also, similar experimental observations have been made. For instance, below 10 mK the slope of the real part of the elastic susceptibility was measured to become temperature independent in vibrating wire experiments [Kön93]. In another study the temperature dependence of the loss of several glasses deviated from the expected  $T^3$ -scaling at low temperatures [Cla94]. These observations suggested that at low temperatures interactions of TLS had to be incorporated into the STM in order to account for the discrepancies. One possibility that was put forward were dipole-dipole interactions between TLS [Wür95, Ens97]. Depending on the ratio  $j = J/\Delta_0$  between the dipolar coupling constant  $J$  and the tunnelling splitting  $\Delta_0$  the TLS may enter from a phase of coherent into one of incoherent tunnelling. This would result on the one hand in a low-temperature suppression of the resonant contribution and on the other hand in an additional relaxation process with a rate  $\tau^{-1} \propto j^4 T$ . The dipolar interaction is known to be of long-range character with a distance dependence of  $r^{-3}$ . Such long-range interactions cause a decrease in the low-energy density of states, a dipole gap, which leaves its mark in the reduction of the low-temperature resonant contribution to the real part of the susceptibilities [Bur95]. Such an argument is very similar to the proposal of a quadrupole pseudo-gap [Bur06c], a model that has been investigated but excluded in the present work. Recent measurements of the dielectric function in poly(vinyl acetate) (PVAc) [Sch17, Fre16] showed that at low frequencies the real part becomes almost temperature independent below 50 mK and the loss tangent does not decrease to zero for  $T \rightarrow 0$ . At frequencies on the MHz scale the real part data exhibit a slightly reduced low-temperature slope as well. The residual low-temperature loss in the imaginary part disappears, though. These findings could in parts be explained by the dipole gap model. PVAc is a polymer with many highly polar bonds so that the dipolar interaction strength between TLS is large.

**High-Frequency Measurements of FR-122P** While this work was focused on low-frequency measurements of both acoustic and dielectric susceptibilities of FR-122P the dielectric function of the same material has been measured as well at 36 MHz using a resonating circuit [Her17]. In Fig. 5.2 changes of the speed of light on the kHz and MHz scale are compared to each other. The position of the maximum rises to higher temperatures when going to the MHz regime unlike below 10 kHz where it scarcely changes. The slope decreases in a similar way around 10 mK at both high and low frequencies. However, the resonant branch above that temperature is steeper at 16 kHz than at 36 MHz. For the latter above 4 K the onset of two-phonon relaxation reveals itself as a kink in the slope. This again justifies that for the low-frequency data below 1 K two-phonon processes could be neglected. A remarkable difference is the slope at intermediate temperatures. The 16 kHz data exhibit a steeper decrease than the 36 MHz data. Since also the high-temperature slope is larger for the 16 kHz data this hints to a larger  $C_d$  in this sample. Given that the slope at 10 mK is much more strongly suppressed at 16 kHz one could argue that a relaxation process, which is more effective at lower frequencies, was responsible for this observation.

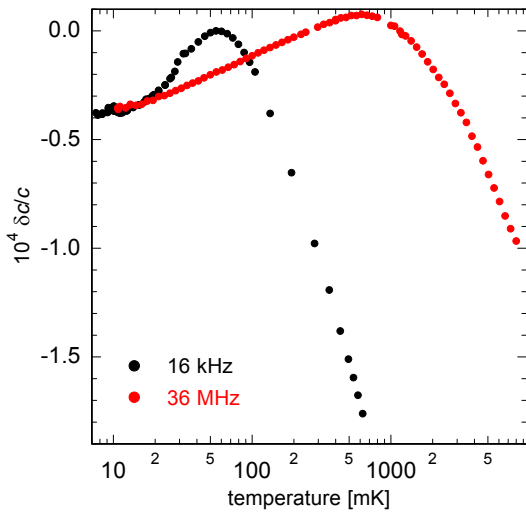


**Figure 5.2:** Comparison of the change of speed of light in FR-122P between 16 kHz and 36 MHz. Besides a change in the maximum position also the slopes, in particular of the resonant branch, are different. Both frequencies exhibit a flattening off towards 10 mK which is more pronounced for 16 kHz, though. The data at 36 MHz were measured in [Her17].

**Other Glasses Containing NQM** Important observations of this work, a flat low-temperature tail and a frequency independent extremum in the real part of the susceptibility, agree with what was measured in other glasses that contain nuclear quadrupole moments.

**BrDGEBA** On the left hand side of Fig. 5.3 the real part of the dielectric function of the brominated molecular glass bisphenol A diglycidyl ether (BrDGEBA) is shown [Aßm18]. Similar to FR-122P BrDGEBA also has a large concentration of bromine atoms which are covalently bound to carbon atoms. Thus, the quadrupole splitting is identical to the one in FR-122P to first order. For frequencies smaller than 10 kHz the permittivity becomes flat below a certain temperature. Unlike in FR-122P this temperature however does increase with rising frequencies approximately following  $f^{1/3}$ . At 16 kHz a minimum emerges but the flat tail at 10 mK remains.

**Multicomponent Glasses** The multicomponent glass HY-1 has a holmium concentration of 0.5 %, an element with a large quadrupole moment. Due to the multicomponent nature of HY-1 it is unclear what the electrical environments of the holmium atoms look like and thus how large the electric field gradients and the quadrupole splittings are. What is more holmium has a very large magnetic moment of  $10.6 \mu_B$  where  $\mu_B$  is Bohr's magneton, caused by the atomic shell. This complicates the situation for besides the quadrupole interaction between nuclei additional intraatomic hyperfine couplings may play a role as well. Still, in the low-frequency real part of the dielectric function, shown on the right hand side of Fig. 5.3, one observes a frequency independent minimum at around 300 mK [Luc16]. Dielectric measurements of NKZFS-11, another multicomponent glass containing NQM, at kHz and MHz frequencies confirmed these findings [Luc16, Sch16b]. Below 8 kHz the minimum is frequency independent and above its positions follows the usual  $f^{1/3}$  scaling.

So far, no model exists that could quantitatively describe the susceptibility data of different glasses that contain NQM. Yet, different groups of glasses with the common trait that interactions of TLS with themselves or with other entities are enabled, be it via direct dipole-dipole coupling or mediated by NQM, also share very similar features in their low-temperature susceptibility data. This leads to the conclusion that these interactions open up an additional relaxation channel for TLS which is responsible for the discrepancies to the STM. The ana-

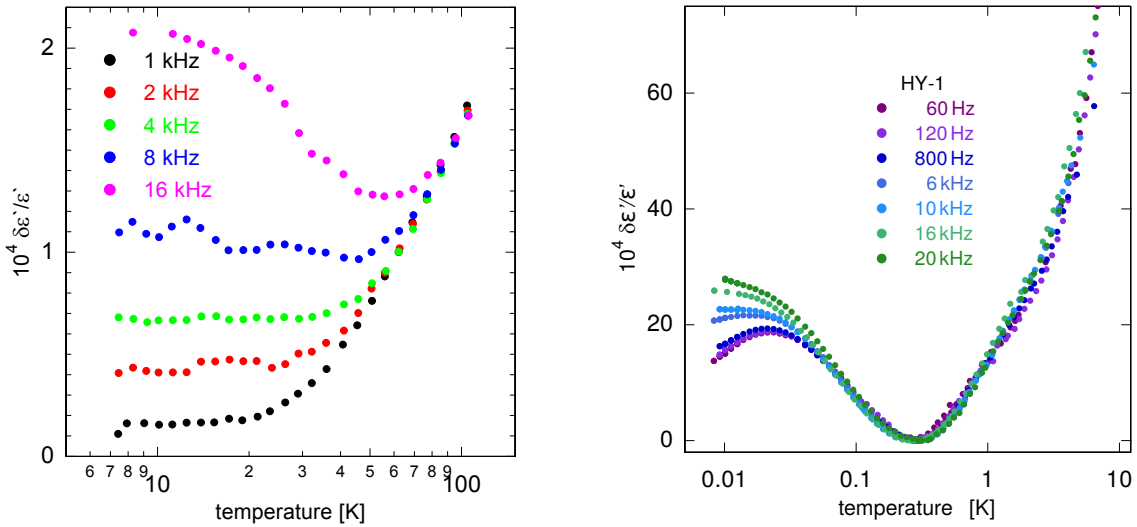


**Figure 5.3:** Relative change of the real part of the dielectric permittivity of the molecular glass Br-DGEBA (left, data from [Aßm18]) and of the multicomponent glass HY-1 (right, data from [Luc16]) at low probing frequencies. For Br-DGEBA the data flatten off below a temperature that does change with frequency. At 16 kHz a minimum starts to become visible. For the case of HY-1 the minimum lies at higher temperatures and is present for all frequencies but does not change its position with varying probing frequency.

lytical form of this relaxation may differ between different groups of glasses depending on the underlying TLS interaction process.

### 5.3 Outlook

**Tunable NQM Content** In order to directly see the influence of NQM a neat follow-up experiment could be measuring the acoustic and dielectric susceptibility for a series of organic samples that contain a variable concentration of NQM. Since both FR-122P and BrDGEBA are materials in which bromine atoms have replaced hydrogen atoms, varying the bromine gas exposition time should yield the desired result. Low-frequency dielectric measurements of DGEBA, which is bromine-free, are currently under way. This directly achieves what has been tried in this work on a single sample with the help of an AC magnetic field of the right frequency. A similar approach was pursued when in glycerol hydrogen, which does not carry a NQM, was replaced by deuteron, that does possess a NQM, for polarisation echo experiments [Bar13].

**Intermediate Frequencies** A missing piece of the whole story are broadband acoustic and dielectric measurements at intermediate frequencies between 20 kHz and 1 MHz. In this frequency region the extremum of the real part of the susceptibilities starts to shift to higher temperatures, at least in the samples investigated so far that exhibit a frequency independent extremum at low probing frequencies. Albeit being experimentally challenging this would provide valuable insights about the transition from the phonon dominated regime into one which is governed by different interactions, e.g. mediated by quadrupoles. It is very hard to design macroscopic mechanical resonators or resonant circuits with a resonance frequency in

this range. One solution could be the usage of micromechanical resonators, which are able to achieve higher resonance frequencies thanks to their smaller length scales. These are typically used for elastic and thermomechanic studies of thin films deposited on the resonator [Won12]. The principle can also be reversed in analogy to the current macroscopic DPO set-up in which the bulk DPO consists of the investigated sample and the layer enables excitation and detection.

**Nuclear Acoustic Resonance** Instead of using (micro)mechanical resonators one could also perform ultrasound (US) experiments with a piezoelectric transducer that is mechanically coupled to a resonance cavity filled with the material of interest. This not only offers the chance to set the probing frequency as desired by changing the length of the resonance cavity but also to apply pulse series. If the US frequency matches the hyperfine splitting frequency the quadrupole transition can also be driven mechanically. The advantage of this nuclear acoustic resonance (NAR) technique is that the speed of sound and the internal friction can be measured simultaneously and with the same field, as opposed to the bias-field module of this work for which two signal lines were needed. This could offer a chance to excite the quadrupole transition without parasitically heating the sample and thus to directly observe the influence of the nuclear quadrupole moments on the elastic susceptibility. Successful examples of this approach include NAR experiments on an insulating manganese spin glass [Dou89]. These revealed strong additional absorption and changes of the speed of sound temperature dependence when the probing frequency matched the hyperfine splitting of the manganese nuclei.

**Lower Temperatures** If the phenomenological quadrupole relaxation model was the only correct ansatz it would be expected that at temperatures significantly smaller than  $E_q/k_B$  the speed of sound should decrease again. The slope of this decrease would then exclusively be determined by the strength of the resonant branch for no relaxation processes would be present anymore. If however a (pseudo)gap in the distribution function does exist at lower temperatures then the resonant branch would flatten off as well. Hence, ultralow-temperature susceptibility measurements of glasses with NQM have the potential to shed more light on the nature of the interactions between NQM and TLS.

**Dielectric Measurements under RF Bias** Currently an experimental set-up is being developed and tested which allows to apply an RF bias field to the sample while the dielectric permittivity can be measured simultaneously with a capacitance bridge. This is in direct analogy to the NQM saturation module designed in this thesis. This approach however has the advantage that no moving parts and no dissipative metal layers are involved so that parasitic heating by the AC magnetic field can be excluded.

## 6. Summary

In this work low-frequency elastic and dielectric susceptibility measurements of a polymer glass were performed at low temperatures. The sample, a polymer with the trade name FR-122P, was chosen because of its high bromine concentration. Given the large nuclear quadrupole moment of the two bromine isotopes the electric field gradient caused by the carbon-bromine bond results in a discrete and known quadrupole splitting of the nuclear energy levels of around 230 MHz and 270 MHz for the two isotopes, respectively. Magnetic contributions such as Zeeman splitting or magnetic dipole interactions are negligible. This made FR-122P well suited for the research question at hand which was determining the role of nuclear quadrupole moments in the low-temperature dynamics of amorphous systems.

For the elastic susceptibility measurements a double paddle oscillator was fabricated from FR-122P. A thin gold layer was sputtered on one side of the double paddle using niobium as an adhesion layer. The gold film enabled capacitive excitation and detection of the double paddle oscillations and improved thermal coupling to the experimental platform. Five different eigenmodes of the double paddle with frequencies ranging from 180 Hz to 6.1 kHz could be found. The change of the resonance frequency as well as the resonance amplitude of each of these modes was measured between 10 mK and 600 mK. From that the speed of sound, or the real part, and the internal friction, or the imaginary part of the elastic susceptibility, could be calculated. As a function of temperature the speed of sound data exhibit a common slope for all frequencies at higher temperatures and a maximum at 30 mK to 40 mK that does not shift with frequency as would be expected from the standard tunnelling model. The slope of the resonant branch was heavily reduced compared to the predicted slope ratio of 2 : -1. In the internal friction data there is a common plateau at higher temperatures. Below about 60 mK the internal friction decreases to a finite value of  $3 \times 10^{-4}$  to  $5 \times 10^{-4}$  depending on the frequency.

The data were tried to be described by numerical simulations using the standard tunnelling, resonant susceptibility and quadrupole driven relaxation model. Neither of the models was able to quantitatively reproduce the data at all frequencies both in the real and imaginary part. However, with a coupling constant of  $C = 3.8 \times 10^{-4}$  the high-temperature slope in the real part and the plateau level in the imaginary part agreed with each other and with the simulation. The models failed to different degrees in explaining the data: The standard tunnelling model alone did not manage to account for the reduced resonant slope and the frequency independence of the maximum. In extension with the resonant susceptibility model the reduced slope could be retrieved but quantitative agreement was only reached for a single frequency. The quadrupole driven relaxation model did reproduce the flat resonant branch for all frequencies and moreover the frequency independent maximum. It failed when it came to describing the internal friction with the same parameters, though, as was the case for the other models, too.

In order to analyse the role of the nuclear quadrupole moments more closely a novel experimental module was developed. It consisted of a clamped loop that could be mounted at the back of the double paddle oscillator. The loop was made from a Nb/Ti-alloy which was superconducting at the temperatures of the experiment. The susceptibility measurements could now be accompanied by an AC electromagnetic bias field which was supposed to drive the quadrupole transition. Sweeping the bias frequency from 0 MHz to 600 MHz several peaks

in the internal friction were detected. One of them coincided with the quadrupole splitting of one of the two bromine isotopes at 270 MHz. A second peak matching the quadrupole moment of the other isotope was not found, though. A sweep of the bias power from  $10^{-8}$  mW to  $10^{-3}$  mW at 270 MHz demonstrated that a likely explanation for the temperature rise could be eddy currents in the dissipative gold layer leading to a rise of the sample temperature and as a consequence a rise in the internal friction, too. The cause of the frequency selective heating may be electromagnetic resonances matching the double paddle geometry or the dimensions of the circuitry. Plotting the internal friction as a function of the speed of sound change in a complex plane representation, which eliminated the explicit temperature dependence, did not unveil any deviations from the unbiased case. Therefore, all observed signal changes had to be attributed to thermal effects. This experiment sets an upper limit on the detectability of the nuclear quadrupole resonance of this sample by this method.

Measurements of the dielectric function at 60 Hz, 1 kHz and 16 kHz complemented the acoustic experiments. These were conducted in a capacitance bridge set-up. At the lowest two frequencies no resonant branch in the speed of light change could be observed. The data flatten off already below about 50 mK which is in agreement with the observations from the elastic measurements. At 16 kHz, though, a maximum forms at 60 mK. The resonant slope is still smaller than expected from the standard tunnelling model and even vanishes below 10 mK. At this temperature there remains a residual loss similar to the elastic case. The macroscopic coupling constant  $C_d = (4.0 \pm 0.2) \times 10^{-4}$  as obtained from the slope of the high-temperature change of speed of light agrees with the value from the loss tangent plateau,  $C_d = (4.31 \pm 0.01) \times 10^{-4}$ , within the errors. This value also lies very close to the macroscopic coupling constant in the elastic case,  $C = (3.8 \pm 0.1) \times 10^{-4}$ .

In conclusion, this work revealed discrepancies between the measured low-temperature susceptibility and predictions by the standard tunnelling model at low frequencies in yet another amorphous system, a brominated polymer glass. The discrepancies could qualitatively be explained by interactions between the nuclear quadrupole moments of bromine atoms in and around atomic tunnelling systems. These interactions cause additional relaxation and are dominant at low temperatures when one-phonon processes have already ceased to contribute.

## References

- [Abr61] A. Abragam: The Principles of Nuclear Magnetism, Clarendon Press (Oxford), ISBN 978-0-19-852014-6, 1961.
- [AH04] Andeen-Hagerling: AH 2700A 50 Hz – 20 kHz ultra-precision capacitance bridge – operation and maintenance manual, 2004.
- [Akl81] J. J. Aklonis: Mechanical properties of polymers, *J. Chem. Educ.*, **58**(11), 892–897, 1981.
- [And70] A. Anderson, and R. Peterson: Selection of a thermal bonding agent for temperatures below 1 K, *Cryogenics*, **10**(5), 430–433, 1970.
- [And72] P. W. Anderson, B. I. Halperin, and C. M. Varma: Anomalous low-temperature thermal properties of glasses and spin glasses, *Philos. Mag.*, **25**(1), 1–9, 1972.
- [Arn75] W. Arnold, and S. Hunklinger: Experimental evidence for the direct interaction between two-level systems in glasses at very low temperatures, *Solid State Commun.*, **17**, 883–886, 1975.
- [Aßm17] N. Aßmann: Unpublished data, 2017.
- [Aßm18] N. Aßmann: Dielektrische Eigenschaften eines bromierten molekularen Glases bei niedrigen Frequenzen und tiefen Temperaturen, Bachelor’s thesis, Heidelberg University, 2018.
- [Bai03] W. C. Bailey, and F. M. Gonzalez: Calculation of bromine nuclear quadrupole coupling constants in gaseous state molecules, *J. Mol. Struct.*, **651–653**, 689–695, 2003.
- [Bar74] M. Barmatz, and B. Golding: Thermoelastic relaxation near the Curie point of EuO, *Phys. Rev. B*, **9**(7), 3064–3073, 1974.
- [Bar13] M. Bartkowiak, M. Bazrafshan, C. Fischer, A. Fleischmann, and C. Enss: Nuclear quadrupole moments as a microscopic probe to study the motion of atomic tunneling systems in amorphous solids, *Phys. Rev. Lett.*, **110**(20), 205 502, 2013.
- [Bel07] L. Belpassi, F. Tarantelli, and A. Sgamellotti: Nuclear electric quadrupole moment of gold, *J. Chem. Phys.*, **126**(6), 064 314, 2007.
- [Ber75] B. S. Berry, and W. C. Pritchett: Vibrating reed internal friction apparatus for films and foils, *IBM J. Res. Dev.*, **19**(4), 334–343, 1975.
- [Ber17] D. Berndtson: Glass spheres forged by volcanic lightning offer clues about eruptions, *Sci. Am.*, 2017.
- [Blo46] F. Bloch, W. W. Hansen, and M. Packard: Nuclear induction, *Phys. Rev.*, **70**(7), 460–474, 1946.

- [Blo48] N. Bloembergen, E. M. Purcell, and R. V. Pound: Relaxation effects in nuclear magnetic resonance absorption, *Phys. Rev.*, **73**(7), 679–712, 1948.
- [Bol93] D. I. Bolef, and R. K. Sundfors (Eds.): Nuclear Acoustic Resonance, Academic Press (London Oxford Boston New York San Diego), ISBN 978-0-12-111250-9, 1993.
- [Bro47] S. B. Brody, W. A. Nierenberg, and N. F. Ramsey: Nuclear moments of the bromine isotopes, *Phys. Rev.*, **72**(3), 258–259, 1947.
- [Bur95] A. L. Burin: Dipole gap effects in low energy excitation spectrum of amorphous solids – theory for dielectric relaxation, *J. Low Temp. Phys.*, **100**, 309–337, 1995.
- [Bur06a] A. L. Burin, S. Hunklinger, C. Enss, and A. Fleischmann: Magnetic field dependence of the low-temperature dielectric constant in glasses, in AIP Conference Proceedings, Vol. 850, 1127–1128, ISBN 978-0-7354-0347-5, 2006.
- [Bur06b] A. L. Burin, I. Y. Polishchuk, P. Fulde, and Y. Sereda: Effect of nuclear quadrupole interactions on the dynamics of two-level systems in glasses, *Phys. Rev. Lett.*, **96**, 025 505, 2006.
- [Bur06c] A. L. Burin, I. Y. Polishchuk, P. Fulde, and Y. Sereda: Low-temperature breakdown of coherent tunneling in amorphous solids induced by the nuclear quadrupole interaction, *Phys. Rev. B*, **73**(1), 014 205, 2006.
- [Cah88] D. G. Cahill, and R. O. Pohl: Lattice vibrations and heat transport in crystals and glasses, *Annu. Rev. Phys. Chem.*, **39**(1), 93–121, 1988.
- [Cla94] J. Classen, C. Enss, C. Bechinger, G. Weiss, and S. Hunklinger: Low-frequency acoustic and dielectric measurements on glasses, *Ann. Phys.*, **3**(5), 315–335, 1994.
- [Cla00] J. Classen, T. Burkert, C. Enss, and S. Hunklinger: Anomalous frequency dependence of the internal friction of vitreous silica, *Phys. Rev. Lett.*, **84**(10), 2176–2180, 2000.
- [Däh10] D. Dähn: Messung der dielektrischen Funktion des Tantal-Oxid-Glases N-KZFS11 bei sehr tiefen Temperaturen, Diploma thesis, Heidelberg University, 2010.
- [Dem06] W. Demtröder: Experimentalphysik 1, Mechanik und Wärme, Springer-Verlag (Berlin Heidelberg), ISBN 978-3-662-54846-2, 2006.
- [Dou80] P. Doussineau, C. Frénois, R. G. Leisure, A. Levelut, and J.-Y. Prieur: Amorphous-like acoustical properties of Na-doped  $\beta$ -Al<sub>2</sub>O<sub>3</sub>, *J. de Phys.*, **41**(10), 1193–1211, 1980.
- [Dou89] P. Doussineau, A. Levelut, W. Schön, and W. D. Wallace: Nuclear acoustic resonance in an insulating manganese spin-glass, *Europhys. Lett.*, **8**(8), 803–808, 1989.
- [Ens97] C. Enss, and S. Hunklinger: Incoherent tunneling in glasses at very low temperatures, *Phys. Rev. Lett.*, **79**(15), 2831–2834, 1997.
- [Ens05] C. Enss, and S. Hunklinger: Low-Temperature Physics, 1st Ed., Springer-Verlag (Berlin Heidelberg), ISBN 978-3-540-23164-6, 2005.
- [Esq92] P. Esquinazi, R. König, and F. Pobell: Acoustic properties of amorphous SiO<sub>2</sub> and PdSiCu, and of crystalline Ag, NbTi and Ta at very low temperatures, *Z. Phys. B*, **87**, 305–321, 1992.

- 
- [Esq98] P. Esquinazi (Ed.): Tunneling Systems in Amorphous and Crystalline Solids, 1st Ed., Springer-Verlag (Berlin Heidelberg), ISBN 978-3-540-63960-2, 1998.
- [Est91] S. Estalji, O. Kanert, J. Steinert, H. Jain, and K. L. Ngai: Uncommon nuclear-spin relaxation in fluorozirconate glasses at low temperatures, *Phys. Rev. B*, **43**(10), 7481–7486, 1991.
- [Fre16] B. Frey: Entwicklung mikrostrukturierter supraleitender Resonatoren zur breitbandigen Untersuchung dielektrischer Eigenschaften zwischen 37 MHz und 1 GHz bei tiefen Temperaturen, Master’s thesis, Heidelberg University, 2016.
- [Haa00] H. Haas, and H. Petrilli: Quadrupole moments of the halogen nuclei, *Phys. Rev. B*, **61**(20), 13 588–13 592, 2000.
- [Hei02] M. Heitz, A. Fleischmann, and C. Enss: Study of elastic properties of solids using a novel SQUID detection technique, *Phys. B*, **316**, 380–382, 2002.
- [Hem08] M. Hempel: Niederfrequente akustische Messungen an metallischen Gläsern bei sehr tiefen Temperaturen, Diploma thesis, Heidelberg University, 2008.
- [Hem14] M. Hempel: Unpublished data, 2014.
- [Hem15] M. Hempel: Elastische Eigenschaften von supraleitenden massiven metallischen Gläsern, PhD thesis, Heidelberg University, 2015.
- [Her17] T. Herbst: Dielectric permittivity of the glass FR-122P between 10 mK and 10 K at 36 MHz, Bachelor’s thesis, Heidelberg University, 2017.
- [Hou02] B. H. Houston, D. M. Photiadis, M. H. Marcus, J. A. Bucaro, X. Liu, and J. F. Vignola: Thermoelastic loss in microscale oscillators, *Appl. Phys. Lett.*, **80**(7), 1300–1302, 2002.
- [Hun72] S. Hunklinger, W. Arnold, S. Stein, R. Nava, and K. Dransfeld: Saturation of the ultrasonic absorption in vitreous silica at low temperatures, *Phys. Lett. A*, **42**(3), 253–255, 1972.
- [Hun75] S. Hunklinger, and L. Piché: Propagation of transverse sound waves in glasses at very low temperatures, *Solid State Commun.*, **17**(9), 1189–1192, 1975.
- [Hun76] S. Hunklinger, and W. Arnold: Physical Acoustics, Vol. 12, 1st Ed., Academic Press (London Oxford Boston New York San Diego), ISBN 978-0-12-477912-9, 1976.
- [Jäc72] J. Jäckle: On the ultrasonic attenuation in glasses at low temperatures, *Z. Phys.*, **257**(3), 212–223, 1972.
- [Jen80] J. E. Jensen, R. B. Stewart, W. A. Tuttle, H. Brechna, and A. G. Prodell (Eds.): Selected Cryogenic Data Notebook, Vol. 2, Brookhaven National Laboratory, 1980.
- [Joh28] J. B. Johnson: Thermal agitation of electricity in conductors, *Phys. Rev.*, **32**(1), 97–109, 1928.
- [Kan80] O. Kanert, R. Kuchler, and M. Mali: NMR-investigation of the dynamic properties of off-center Ag<sup>+</sup> defects in RbCl, *J. de Phys.*, **41**(7), 404–407, 1980.
- [Kar04] J. T. Karvonen, L. J. Taskinen, and I. J. Maasilta: Electron-phonon interaction in thin copper and gold films, *Phys. Status Solidi C*, **1**(11), 2799–2802, 2004.

- 
- [Kay11] G. W. C. Kaye, and T. H. Laby: Tables of Physical and Chemical Constants and Some Mathematical Functions, 1st Ed., Longmans, Green, and Co. (London), 1911.
- [Kle85] R. N. Kleiman, G. K. Kaminsky, J. D. Reppy, R. Pindak, and D. J. Bishop: Single-crystal silicon high- $Q$  torsional oscillators, *Rev. Sci. Instrum.*, **56**(11), 2088–2091, 1985.
- [Klo08] F. Klotz: Untersuchung von Kernquadrupolwechselwirkungen in lithiumdotiertem Kaliumchlorid, Diploma thesis, Heidelberg University, 2008.
- [Kön93] R. König, P. Esquinazi, and F. Pobell: Nonlinear acoustic properties of vibrating wires at very low temperatures, *J. Low Temp. Phys.*, **90**(1), 55–76, 1993.
- [Kre03] F. Kremer, and A. Schönhalz (Eds.): Broadband Dielectric Spectroscopy, 1st Ed., Springer-Verlag (Berlin Heidelberg), ISBN 978-3-540-43407-8, 2003.
- [Kus17] A. Kushino, and S. Kasai: Development of semi-rigid superconducting coaxial cables as low-pass filters, *IEEE Trans. on Appl. Supercond.*, **27**(4), 1200 204, 2017.
- [Lae77] C. Laermans, W. Arnold, and S. Hunklinger: Influence of an electromagnetic wave on the acoustic absorption of borosilicate glass at low temperatures, *J. Phys. C*, **10**, 161–165, 1977.
- [Las75] J. C. Lasjaunias, A. Ravex, M. Vandorpe, and S. Hunklinger: The density of low energy states in vitreous silica: Specific heat and thermal conductivity down to 25 mK, *Solid State Commun.*, **17**(9), 1045–1049, 1975.
- [Lay01] M. Layer, M. Heitz, J. Classen, C. Enss, and S. Hunklinger: Low-temperature elastic properties of glasses in magnetic fields, *J. Low Temp. Phys.*, **124**(3-4), 419–429, 2001.
- [Lee91] W. K. Lee, J. F. Liu, and A. S. Nowick: Limiting behavior of AC conductivity in ionically conducting crystals and glasses: A new universality, *Phys. Rev. Lett.*, **67**(12), 1559–1561, 1991.
- [Lin76] B. Lindman, and S. Forsen (Eds.): Chlorine, Bromine and Iodine NMR – Physico-Chemical and Biological Applications, Vol. 12, 1st Ed., Springer-Verlag Berlin Heidelberg, ISBN 978-3-642-66365-9, 1976.
- [Luc14] A. Luck, A. Fleischmann, A. Reiser, and C. Enss: Effects of large nuclear quadrupoles on dielectric properties of glasses at very low temperatures, *J. Physics: Conf. Ser.*, **568**(3), 032013, 2014.
- [Luc16] A. Luck: Nuclear spin dominated relaxation of atomic tunneling systems in glasses, PhD thesis, Heidelberg University, 2016.
- [Lud56] G. W. Ludwig: Some bromine, iodine, and indium nuclear quadrupole interaction frequencies, *J. Chem. Phys.*, **25**(159), 159–171, 1956.
- [Lud02] S. Ludwig, C. Enss, P. Strehlow, and S. Hunklinger: Direct coupling of magnetic fields to tunneling systems in glasses, *Phys. Rev. Lett.*, **88**(7), 075 501, 2002.
- [Mat79] R. A. Matula: Electrical resistivity of copper, gold, palladium, and silver, *J. Phys. Chem. Ref. Data*, **8**(4), 1147–1300, 1979.

- 
- [Max14] Max Planck Society: From thin silicate films to the atomic structure of glass, [phys.org/news/2014-06-thin-silicate-atomic-glass.html](https://phys.org/news/2014-06-thin-silicate-atomic-glass.html), last visited: 10/02/2018, 2014.
- [McI06] M. J. McIntire, and E. L. Chronister: Characterization of tunneling systems in molecular versus polymer glasses by high-pressure photon echo spectroscopy, *J. Chem. Phys.*, **124**(1), 14 904, 2006.
- [Mes05] D. Meschede: Gerthsen Physik, 23rd Ed., Springer-Verlag (Berlin Heidelberg), ISBN 978-3-540-25421-8, 2005.
- [Nar70] V. Narayanamurti, and R. O. Pohl: Tunneling states of defects in solids, *Rev. Mod. Phys.*, **42**(2), 201–237, 1970.
- [Nyq28] H. Nyquist: Thermal agitation of electric charge in conductors, *Phys. Rev.*, **32**(1), 110–113, 1928.
- [Phi72] W. A. Phillips: Tunneling states in amorphous solids, *J. Low Temp. Phys.*, **7**(3-4), 351–360, 1972.
- [Phi81] W. A. Phillips (Ed.): Amorphous Solids, 1st Ed., Springer-Verlag (Berlin Heidelberg), ISBN 978-3-642-81536-2, 1981.
- [Phi87] W. A. Phillips: Two-level states in glasses, *Reports on Prog. Phys.*, **50**, 1657–1708, 1987.
- [Pob07] F. Pobell: Matter and Methods at Low Temperatures, 3rd Ed., Springer-Verlag (Berlin Heidelberg), ISBN 978-3-540-46356-6, 2007.
- [Pro16] I. C. L. Products: ICL Industrial Products. FR-122P application data sheet for expanded polystyrene foam (EPS), 2016.
- [Ray84] A. K. Raychaudhuri, and S. Hunklinger: Low-frequency elastic properties of glasses at low temperatures – Implications on the tunneling model, *Z. Phys. B*, **125**, 113–125, 1984.
- [Ree66] W. Reese: Low-temperature thermal conductivity of amorphous polymers: Polystyrene and polymethylmethacrylate, *J. Appl. Phys.*, **37**(2), 864–868, 1966.
- [Rei05] A. Reiser: Glasübergang niedermolekularer organischer Flüssigkeiten unter Druck – Dielektrische und dilatometrische Studien, PhD thesis, Heidelberg University, 2005.
- [Rei13] A. Reifenberger, and M. Hempel: Unpublished data, 2013.
- [Rei17] A. Reifenberger: Spezifische Wärme von supraleitenden metallischen Gläsern bei tiefen Temperaturen, PhD thesis, Heidelberg University, 2017.
- [Rub74] M. Rubinstein, and P. C. Taylor: Nuclear quadrupole resonance in amorphous and crystalline As<sub>2</sub>S<sub>3</sub>, *Phys. Rev. B*, **9**(10), 4258–4276, 1974.
- [Rub75] M. Rubinstein, H. A. Resing, T. L. Reinecke, and K. L. Ngai: Nuclear spin lattice relaxation in amorphous materials B<sub>2</sub>O<sub>3</sub>, *Phys. Rev. Lett.*, **34**(23), 1444–1447, 1975.
- [Sal94] D. J. Salvino, S. Rogge, B. Tigner, and D. D. Osheroff: Low temperature AC dielectric response of glasses to high DC electric fields, *Phys. Rev. Lett.*, **73**(2), 268–271, 1994.

- [Sam68] G. V. Samsonov (Ed.): Handbook of the Physiochemical Properties of the Elements, 2nd Ed., Instituto de Formento Industrial, ISBN 978-1-4684-6068-1, 1968.
- [Sch67] E. Schmidt (Ed.): Landolt-Börnstein. Wärmetechnische Messverfahren. Thermodynamische Eigenschaften homogener Stoffe, 6th Ed., Springer-Verlag (Berlin Heidelberg), ISBN 978-3-540-03899-3, 1967.
- [Sch76] M. von Schickfus, and S. Hunklinger: The dielectric coupling of low-energy excitations in vitreous silica to electromagnetic waves, *J. Phys. C*, **9**, 439–442, 1976.
- [Sch16a] A. Schaller: Novel readout system and online analysis for dielectric polarisation echoes, Master’s thesis, Heidelberg University, 2016.
- [Sch16b] C. W. Scholz: Untersuchung der dielektrischen Eigenschaften von N-KZFS11 zwischen 300 K und 10 mK bei 25 MHz, Bachelor’s thesis, Heidelberg University, 2016.
- [Sch17] M. Schrodin: Low temperature dielectric properties of amorphous poly(vinyl acetate) and poly(vinyl chloride), Master’s thesis, Heidelberg University, 2017.
- [Shi16] Y. Shin, H. Lee, W. Lee, and D. Y. Ryu: Glass transition and thermal expansion behaviour of polystyrene films supported on polystyrene-grafted substrates, *Macromolecules*, **49**, 5291–5296, 2016.
- [Sie93] H. Sieranski, O. Kanert, and M. Backens: Low-frequency excitations in sodium beta-alumina: An NMR study, *Phys. Rev. B*, **47**(2), 681–685, 1993.
- [Sie98] W. M. Siebert: Circuits, Signals, and Systems, 11th Ed., MIT Press (Cambridge), ISBN 978-0-262-19229-3, 1998.
- [Smi07] G. D. Smith, and D. Bedrov: Relationship between the  $\alpha$  and  $\beta$ -relaxation processes in amorphous polymers: Insight from atomistic molecular dynamics simulations of 1,4-polybutadiene melts and blends, *J. Polym. Sci. B*, **45**(6), 627–644, 2007.
- [Ste16] M. P. Steven: Chemistry of industrial polymers, [britannica.com/topic/industrial-polymer-chemistry-468716](http://britannica.com/topic/industrial-polymer-chemistry-468716), last visited: 27/02/2018, 2016.
- [Sto95] J. T. Stockburger, M. Grifoni, and M. Sassetti: Nonlinear acoustic response of glasses in the tunneling model, *Phys. Rev. B*, **51**(5), 2835–2843, 1995.
- [Sto05] N. J. Stone: Table of nuclear magnetic dipole and electric quadrupole moments, *At. Data Nucl. Data Tables*, **90**(1), 75–176, 2005.
- [Str98] P. Strehlow, C. Enss, and S. Hunklinger: Evidence for a phase transition in glasses at very low temperature: A macroscopic quantum state of tunneling systems?, *Phys. Rev. Lett.*, **80**(24), 5361–5364, 1998.
- [Str00] P. Strehlow, M. Wohlfahrt, A. G. M. Jansen, R. Haueisen, G. Weiss, C. Enss, and S. Hunklinger: Magnetic field dependent atomic tunneling in non-magnetic glasses, *Phys. Rev. Lett.*, **84**(9), 1938–1941, 2000.
- [Swa89] E. T. Swartz, and R. O. Pohl: Thermal boundary resistance, *Rev. Mod. Phys.*, **61**(3), 605–669, 1989.
- [Sys14] D. Systems: Solidworks material database. mechanical material properties of polystyrene and gold, 2014.

- 
- [Sze75] J. Szeftel, and H. Alloul: Nuclear spin-lattice relaxation associated with low-energy excitations in glasses, *Phys. Rev. Lett.*, **34**(11), 657–660, 1975.
- [Tie92] D. Tielburger, R. Merz, R. Ehrenfels, and S. Hunklinger: Thermally activated relaxation processes in vitreous silica: An investigation by Brillouin scattering at high temperatures, *Phys. Rev. B*, **45**(6), 2750–2760, 1992.
- [War61] R. W. Warfield, and M. C. Petree: Thermodynamic properties of polystyrene and styrene, *J. Polym. Sci.*, **55**, 497–505, 1961.
- [Was80] Y. Waseda: Structure of Non-Crystalline Materials, 1st Ed., McGraw-Hill (New York), ISBN 978-0-070-68426-3, 1980.
- [Wei98] J. G. Weisend (Ed.): Handbook of Cryogenic Engineering, 1st Ed., Taylor & Francis (Abingdon), ISBN 978-1-560-32332-7, 1998.
- [Whi95] B. E. White, and R. O. Pohl: Internal friction of subnanometer  $\alpha$ -SiO<sub>2</sub> films, *Phys. Rev. Lett.*, **75**(24), 4437–4440, 1995.
- [Woe63] D. E. Woessner, and H. S. Gutowsky: Nuclear pure quadrupole relaxation and its temperature dependence in solids, *J. Chem. Phys.*, **39**(2), 440–456, 1963.
- [Won12] Y. Won, J. Lee, M. Asheghi, T. W. Kenny, and K. E. Goodson: Phase and thickness dependent modulus of Ge<sub>2</sub>Sb<sub>2</sub>Te<sub>5</sub> films down to 25 nm thickness, *Appl. Phys. Lett.*, **100**, 161 905, 2012.
- [Wur95] A. Wurger: Collective low-energy excitations of two-level tunnelling defects in mixed crystals, *Z.Phys. B*, **98**, 561–573, 1995.
- [Wur97] A. Wurger: From Coherent Tunneling to Relaxation, 1st Ed., Springer-Verlag (Berlin Heidelberg), ISBN 978-3-540-61424-1, 1997.
- [Wur02] A. Wurger, A. Fleischmann, and C. Enss: Dephasing of atomic tunneling by nuclear quadrupoles, *Phys. Rev. Lett.*, **89**(23), 237 601, 2002.
- [Zac32] W. H. Zachariasen: The atomic arrangement in glass, *J. Am. Chem. Soc.*, **54**(10), 3841–3851, 1932.
- [Zel71] R. C. Zeller, and R. O. Pohl: Thermal conductivity and specific heat of non-crystalline solids, *Phys. Lett. B*, **4**(6), 2029–2041, 1971.

# Appendices

## A Mathematical Derivations

### Occupation Probability of the Energy Levels of a TLS

The probabilities  $w_+$  and  $w_-$  to occupy the upper or lower energy state, respectively, are linked by the Boltzmann factor

$$\frac{w_+}{w_-} = \exp\left(-\frac{E}{k_B T}\right) \quad (1)$$

and normalised

$$w_+ + w_- = 1. \quad (2)$$

Let  $N$  be the total number of identical TLS and  $\Delta N$  the occupation difference then it follows

$$\begin{aligned} \Delta N &= N_- - N_+ \\ &= N(w_- - w_+) \\ &= N(w_- - w_+) \underbrace{\frac{1}{w_- + w_+}}_{=1} \\ &= N \frac{1 - \frac{w_+}{w_-}}{1 + \frac{w_+}{w_-}} \\ &\stackrel{(1)}{=} N \frac{1 - \exp\left(-\frac{E}{k_B T}\right)}{1 + \exp\left(-\frac{E}{k_B T}\right)} \\ &= N \frac{\exp\left(-\frac{E}{2k_B T}\right) - \exp\left(-\frac{E}{2k_B T}\right)}{\exp\left(-\frac{E}{2k_B T}\right) + \exp\left(-\frac{E}{2k_B T}\right)} \\ &= N \frac{2 \sinh\left(-\frac{E}{2k_B T}\right)}{2 \cosh\left(-\frac{E}{2k_B T}\right)} \\ &= N \tanh\left(-\frac{E}{2k_B T}\right). \end{aligned} \quad (3)$$

## B Complementary Figures

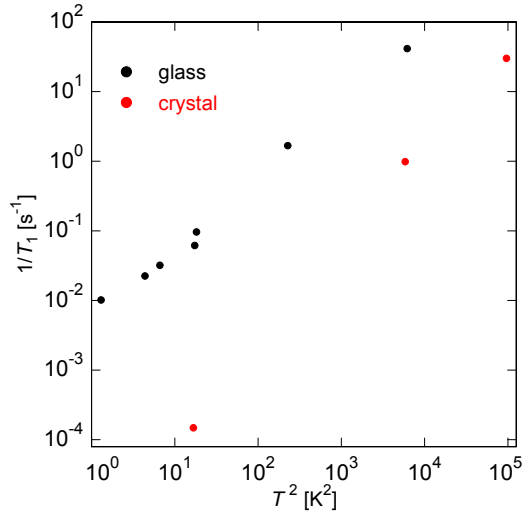


**Figure B.1:** In nuclear quadrupole resonance experiments the longitudinal relaxation rates  $1/T_1$  in vitreous  $\text{As}_2\text{S}_3$  are by two orders of magnitude larger than the corresponding rates in crystalline  $\text{As}_2\text{S}_3$  (data from [Rub74]).

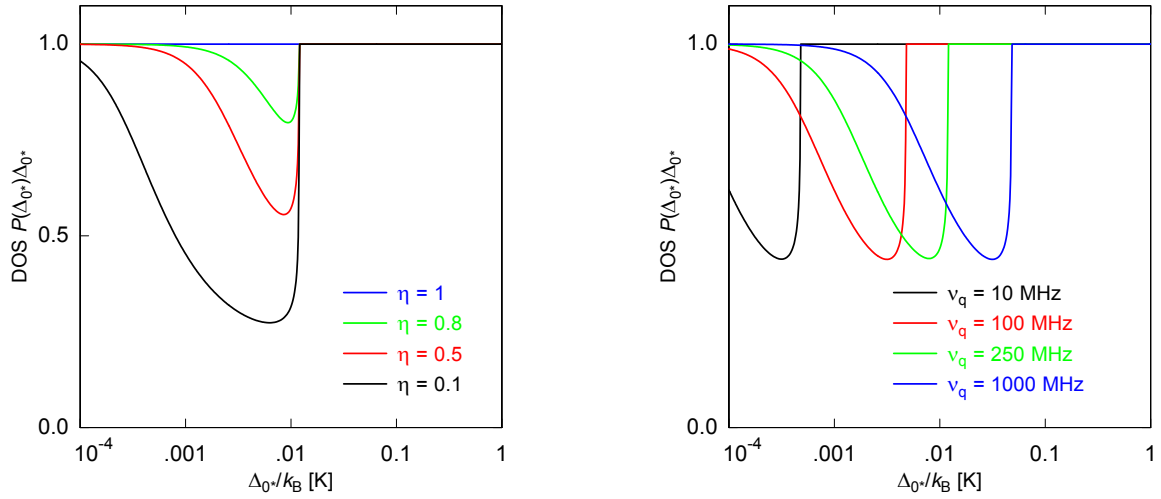


**Figure B.2:** Logarithmic density of states of TLS with varying spin wave function overlap  $\eta$  at constant  $\nu_q = 0.01 \text{ K } k_B/h$  (left) and varying quadrupole resonance frequency  $\nu_q$  at constant  $\eta = 0.1$  (right) as a function of the renormalised tunnelling amplitude  $\Delta_{0*}$ . For both plots one nucleus per TLS is assumed.

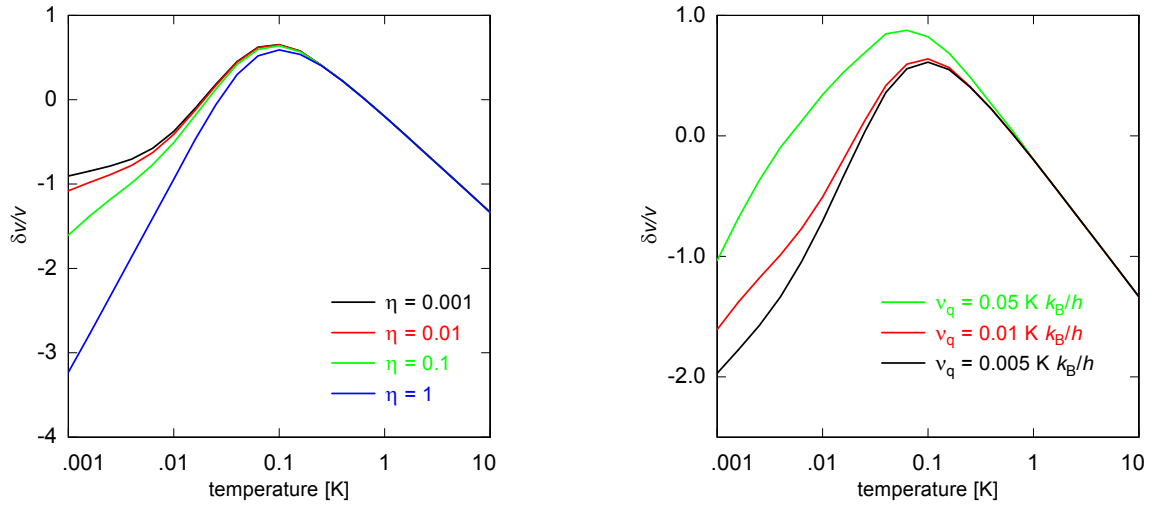


**Figure B.3:** Real part of the dynamic elastic constant for varying spin wave function overlap  $\eta$  at constant  $\nu_q = 0.01 \text{ K } k_B/\hbar$  (left) and varying quadrupole resonance frequency  $\nu_q$  at constant  $\eta = 0.1$  (right) as a function of temperature. For both plots one nucleus per TLS is assumed.

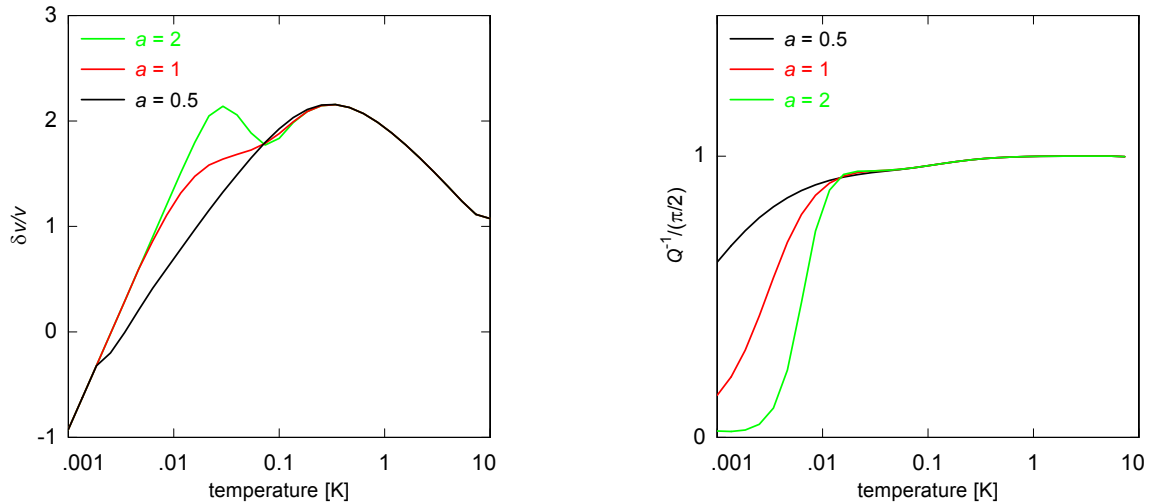


**Figure B.4:** The impact of the exponent  $a$  on the quadrupole relaxation mechanism is shown for the real part (left) and for the imaginary part (right). The larger  $a$  the more pronounced is the additional maximum in the real part and the steeper is the decrease at temperatures below the end of the quadrupole plateau in the imaginary part.

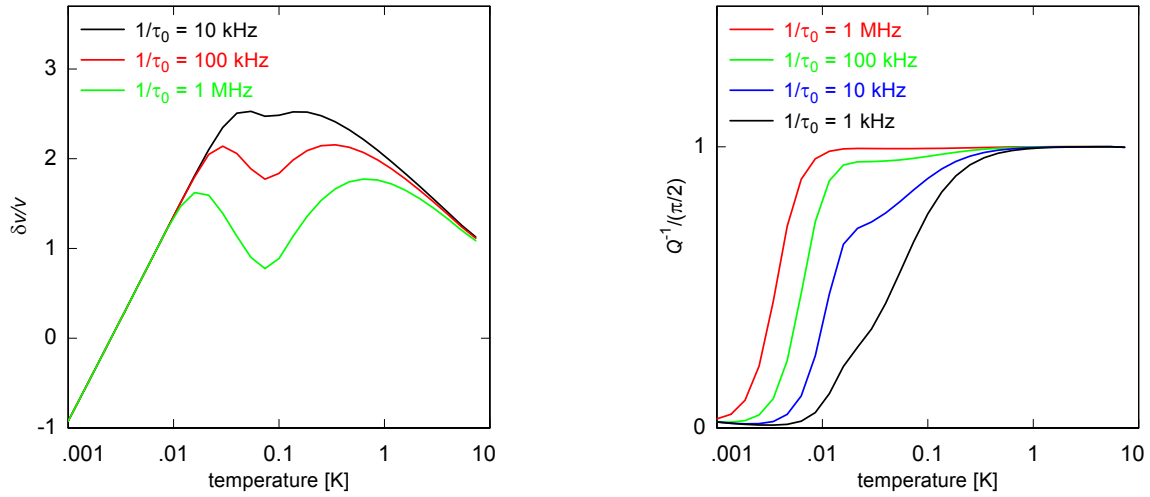


**Figure B.5:** The impact of the constant rate  $\tau_0^{-1}$  on the quadrupole relaxation mechanism is shown for the real part (left) and for the imaginary part (right). With increasing  $\tau_0^{-1}$  the valley between the additional real part maximum and the one-phonon maximum deepens and the level of the quadrupole plateau in the imaginary part increases.

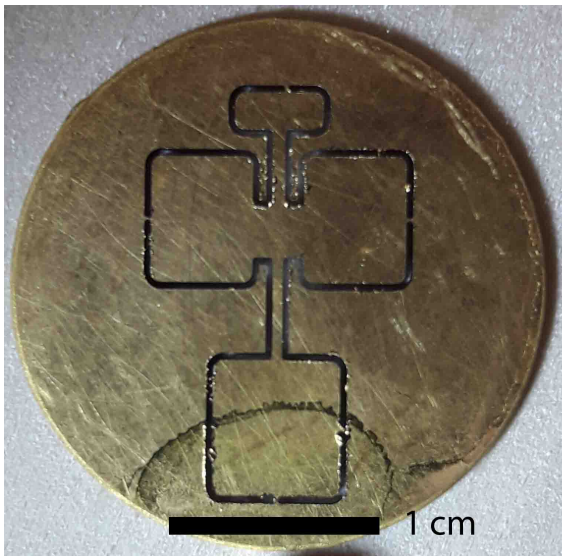


**Figure B.6:** The DPO inside the sample disc after deposition of the gold layer and after milling. At four places the DPO is still attached to the rest of the disc by tiny bridges.

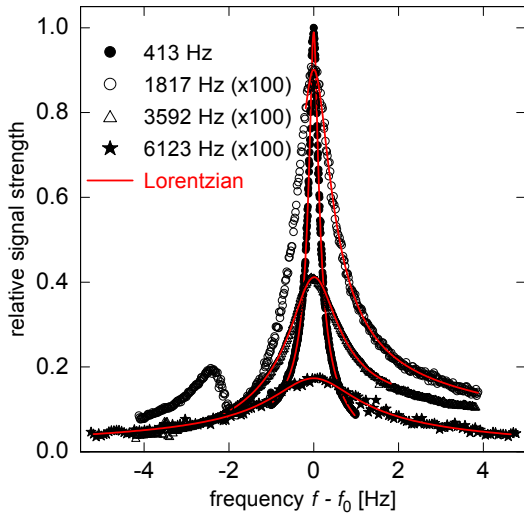


**Figure B.7:** Relative signal strength of different eigenmodes. Note that the three highest frequencies, i.e. the modes B2, B3 and F, were amplified by a factor of 100 in order to fit on the same scale as the ST mode.

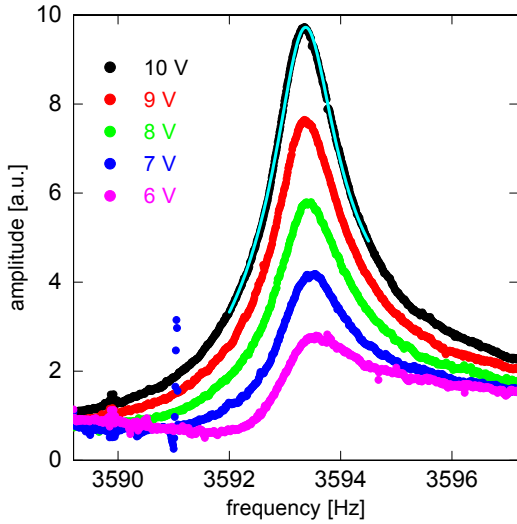


**Figure B.8:** Peak shape of the B3 mode at different excitation voltages  $V_0$  at 15 mK. If  $V_0$  is too small then the background is comparable to the peak size. The larger  $V_0$  the more symmetric does the resonance curve get and the less important becomes the background. Only at very high voltages  $V_0 = 10$  V does the curve start to show a slight tendency to tilt to the left when compared to a Lorentzian line fit (solid line).

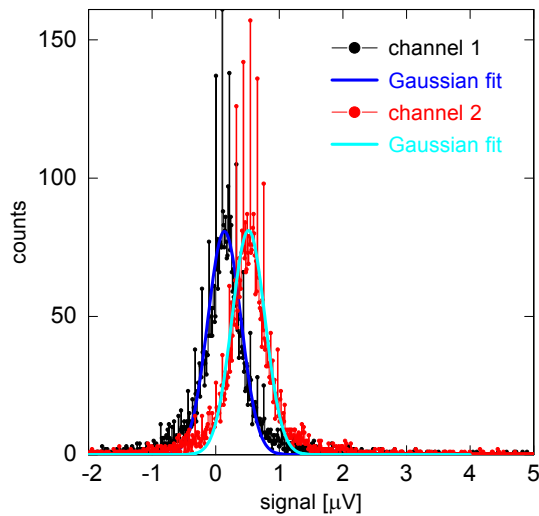


**Figure B.9:** Histogram of the background noise on channel 1,  $A \cos(\varphi)$ , and channel 2,  $A \sin(\varphi)$ , without any excitation voltage applied. The noise level on each channel follows approximately a Gaussian distribution centred around  $0.2 \mu\text{V}$  or  $0.5 \mu\text{V}$ , respectively, with a standard deviation of  $\sigma = 0.3 \mu\text{V}$  each.

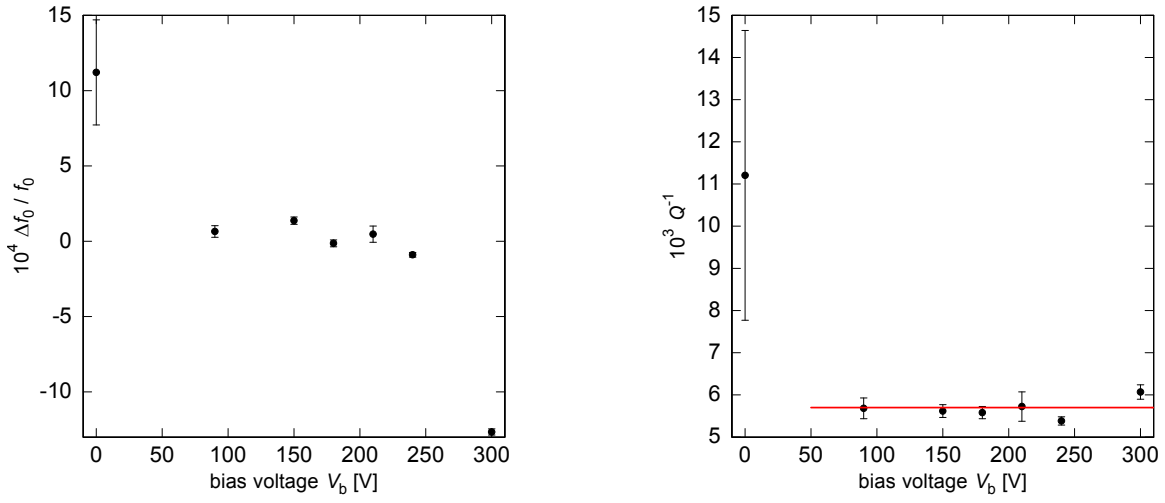


**Figure B.10:** The resonance frequency decreases with increasing bias voltage (left) while the internal friction remains constant for finite bias voltages (right). The solid red line is the mean value of the internal friction for finite bias voltages. The data were acquired at 81 K in the nitrogen bath cryostat.

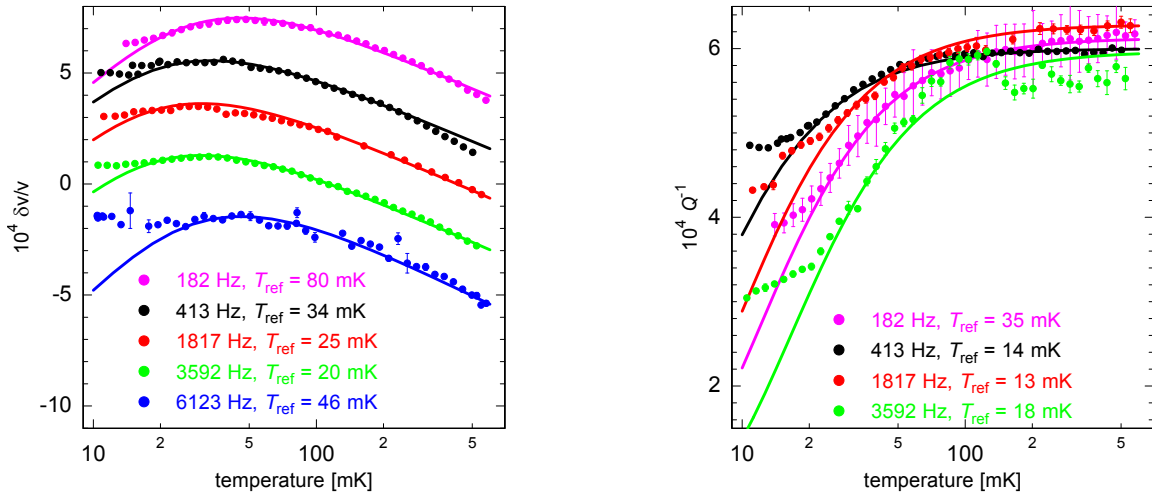


**Figure B.11:** Standard tunnelling model predictions for the speed of sound (left) and the internal friction (right). The fit parameters  $T_{\text{ref}}$  and  $C$  vary for each frequency. While the macroscopic coupling constant only differs by around 5% between different frequencies the one-phonon relaxation strength changes by a factor of six and is consistently smaller for the internal friction than for the speed of sound.

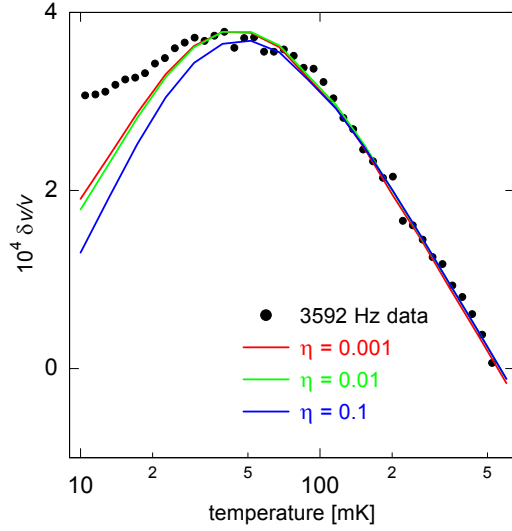


**Figure B.12:** Varying the nuclear spin wavefunction overlap integral  $\eta$  over three orders of magnitude does not significantly change the shape of the speed of sound curve. The parameters used for the simulation were  $n = 1$ ,  $\nu_q = 250$  MHz,  $C = 4.1 \times 10^{-4}$  and  $T_{\text{ref}} = 37$  mK.

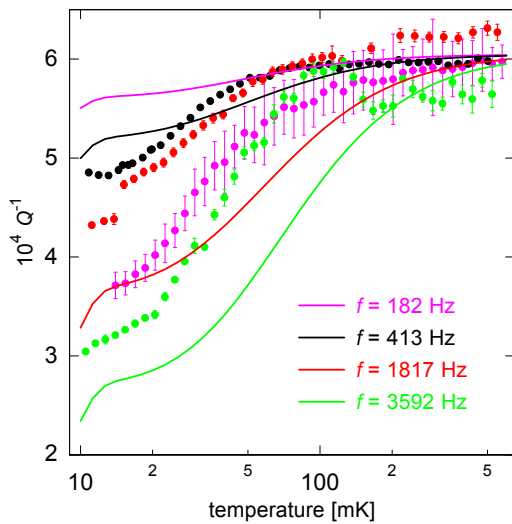


**Figure B.13:** The nuclear quadrupole driven relaxation model is able to produce a side hill at lowest temperatures in the internal friction which qualitatively agrees with the temperature dependence of the data. For the simulations the parameters  $\nu_q = 250$  MHz,  $T_{\text{ref}} = 80$  mK,  $C = 3.85 \times 10^{-4}$ ,  $\tau_0^{-1} = 12$  kHz were used.

## Danksagung

*Keine Schuld ist dringender als die, Dank zu sagen.*

— Marcus Tullius Cicero

Ich möchte mich an dieser Stelle bei all denjenigen bedanken, die mich während der Masterarbeit, aber auch im Laufe des gesamten Studiums unterstützt haben. Ohne vielfältige soziale Beziehungen zu kompetenten und lieben Menschen wären die Erstellung dieser Arbeit und die ganzen zurückliegenden fünfeinhalb Jahre nicht nur um eine Größenordnung anstrengender, sondern auch um zwei Größenordnungen weniger schön gewesen.

Mein besonderer Dank gilt

PROF. CHRISTIAN ENSS für die Aufnahme in seine Arbeitsgruppe, den Vorschlag dieses interessanten Themas, welches tiefste Quantenphysik mit makroskopischen Vorgängen verknüpft, die anregenden Impulse bei den Gruppensitzungen, sowie die erinnerungswerten Erlebnisse auch außerhalb der Forschung, sei es bei der physikalischen Weihnachtsshow oder auf der Neckarfähre während der ULT-Tagung,

PROF. RÜDIGER KLINGELER für das Interesse an dieser Arbeit und die Übernahme des Zweitgutachtens,

DR. ANDREAS REISER für die kompetente und tatkräftige Unterstützung in allen Belangen von der Fertigung des DPO bis zu Diskussionen über die Messergebnisse, die Korrekturlektüre des Manuskripts, sowie das Teilen seines unglaublich großen Sachverstands und Allgemeinwissens zum und über das Projekt hinaus,

DR. ANDREAS FLEISCHMANN für die stets erhellenden, von einem tiefen Verständnis geprägten Gespräche über allerlei Physikthemen und die Verbesserungsvorschläge bei der Gestaltung des DPG-Frühjahrstagungsposters,

DR. MARIUS HEMPEL für das sorgfältige und ausführliche Korrekturlesen der Arbeit, die Überlassung des entwickelten Versuchsaufbaus für neue Experimente und Erweiterungen, sowie die nachhaltigkeitsorientierten Diskussionen und Veranstaltungsvorschläge,

DR. ANNINA LUCK für die Initiation in die kernquadrupolmomentdominierte Relaxation und die Einführung in die niederfrequenten dielektrischen Messungen,

DR. ANDREAS REIFENBERGER für die Hilfestellungen und Motivationsappelle zu Genplot, die Ratschläge zu wissenschaftlichem Arbeiten an sich, sowie für manchen zynischen, aber immer nett gemeinten Kommentar,

BENEDIKT FREY für die Begleitung bei den ersten Gehversuchen mit dem Verdünnungskryostaten und den immerzu tollen Stunden im Labor,

MATTHÄUS KRANTZ UND DEM GANZEN REINRAUM-TEAM für die Bedienung der Sputteranlage bei der Prozessierung der Proben,

RUDI EITEL für die zuverlässige Bereitstellung von flüssigem Helium,

WERNER LAMADE, SIEGRIED SPIEGEL UND DEM KOMPLETTEN WERKSTATT-TEAM für die Fertigung des neuen experimentellen Aufbaus zur Anregung des Kernquadrupolübergangs und die Hilfe bei diversen Kleinprojekten,

DR. JEYAKUMAR ALBERT, the Technical Manager of ICL Europe, for kindly supplying us with the FR-122P sample material,

NICOLE ASSMANN UND TIMOTHY HERBST für das gemeinsame Interesse an unserer Probe FR-122P und für die ausgetauschten Daten,

MATTHEW HERBST, SVEN LUTTER, DR. MARIUS HEMPEL, DR. ANDREAS REIFENBERGER, DR. ANNINA LUCK UND ERIK WEERDA für die grandiose Zeit im Büro 0.310, die zwar auch aber nicht nur von bierernster Physik geprägt war, kaj mi ankaŭ volas diri dankon al ĉiuj karaj kollegoj kun malfermitaj koroj por la esperantaj amuzaĵoj kaj belegaj musikemaj interaktoj,

DER GANZEN ARBEITSGRUPPE F345-N3RDT3MPE1 für die eine oder andere schnelle Beantwortung von Fragen auf dem Gang, die schönen Erlebnisse auf den beiden Frühjahrskonferenzen in Dresden und Berlin, die fantastischen Weihnachts- und Sommerfestfeiern, sowie die vielen netten Mensa- und Kaffeerunden über Mittag,

DEN PHYSIKOZYTEN für die ganzen Schlemmerdilemmata, Mitternachtsvolleyballturniere, Wanderungen, Radtouren und die übrigen kaum aufzählbaren Aktionen, die das Studium erst lebenswert und das Leben studienwert gemacht haben und

MEINEN LIEBEN ELTERN STEFANIE UND MANFRED SCHYGULLA für die finanzielle, ideelle und vor Allem liebevolle Förderung durch das ganze Studium hindurch.

## Statement of Authorship

I hereby declare that I am the sole author of this Master's thesis. I confirm that I have not used any other sources than those listed in the bibliography and identified as references. I further declare that I have not submitted this thesis at any other institution in order to obtain a degree.

Hiermit versichere ich, dass ich diese Masterarbeit eigenständig verfasst habe. Ich bestätige, dass ich keine anderen als die im Quellenverzeichnis angegebenen und als solche gekennzeichneten Quellen und Hilfsmittel verwendet habe. Des weiteren versichere ich, dass ich diese Arbeit bei keiner anderen Universität zur Erlangung eines Abschlusses eingereicht habe.

Heidelberg, April 20, 2018

---

Patrick Schygulla